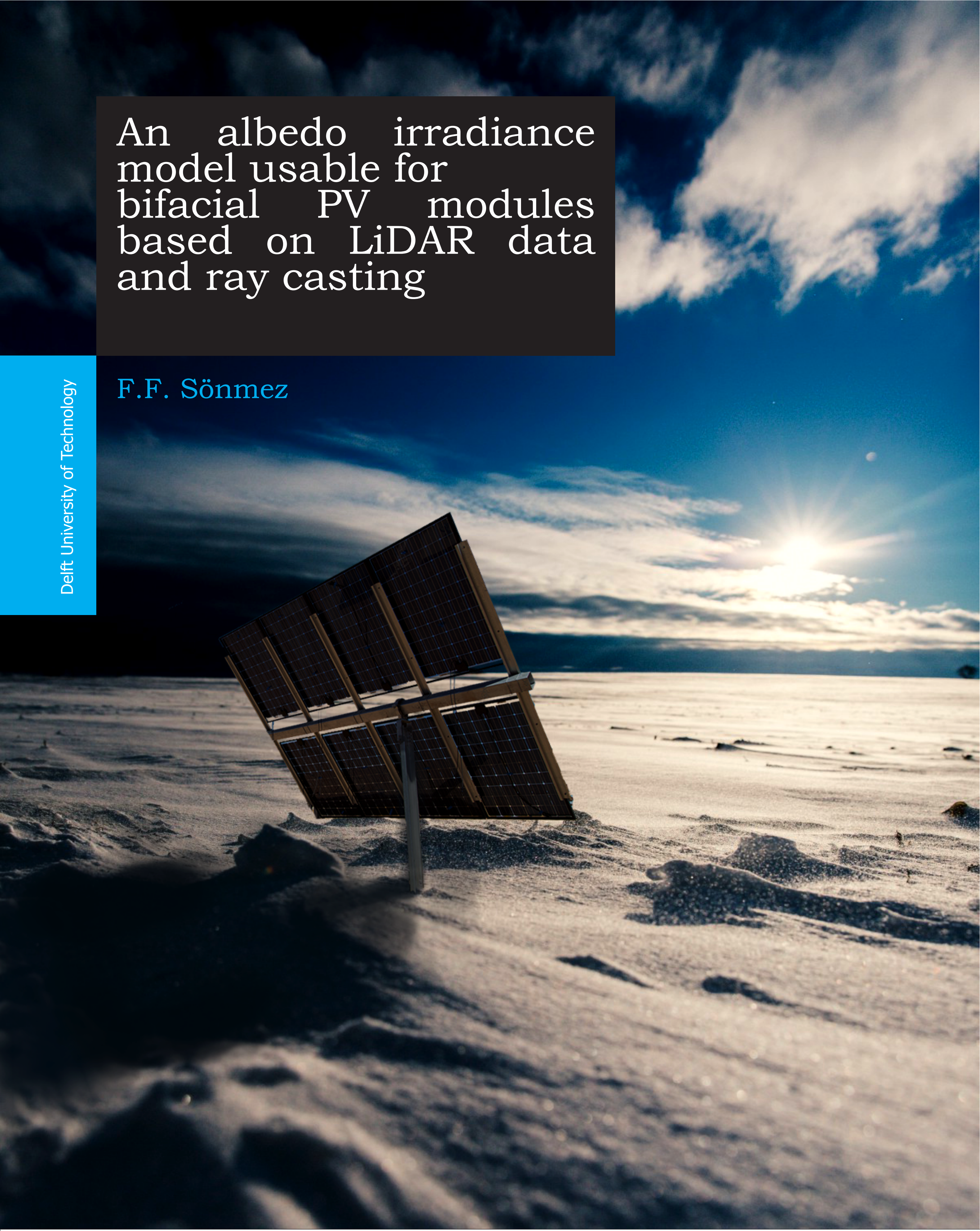

An albedo irradiance model usable for bifacial PV modules based on LiDAR data and ray casting

F.F. Sönmez

Delft University of Technology

TU Delft Delft University of Technology

Challenge the future

An albedo irradiance model usable for bifacial PV modules based on LiDAR data and ray casting

by

F.F. Sönmez

in partial fulfillment of the requirements for the degree of

Master of Science
in Sustainable Energy Technology

at the Delft University of Technology,
to be defended publicly on Friday December 8, 2017 at 14:30 AM.

Supervisor:	Dr. ir. O. Isabella,	TU Delft
Daily supervisor:	Dr. ir. H. Ziar,	TU Delft
Thesis committee:	Dr. ir. O. Isabella,	TU Delft
	Prof. Dr. Ir. M. Zeman,	TU Delft
	Dr. ir. H. Ziar,	TU Delft
	Dr. ir. M. Cvetkovic,	TU Delft
	Ir. M. van Hoolwerff,	SolarMonkey

An electronic version of this thesis is available at `http://repository.tudelft.nl/`.

TU Delft
Delft
University of
Technology

Acknowledgements

First of all, I want to express my sincere gratitude to everyone that has supported me in the largest project of my life until now. Specifically, I want to thank Olindo Isabella in guiding me through my thesis as my supervisor, despite having a very busy agenda. In my first few months, you have not only been my supervisor, but also my daily supervisor. Next I want to thank Hesan Ziar for taking over the role as daily supervisor for the rest of my thesis. Thank you for always holding your door open for me, for your incredible eye for detail and for all the feedback that you have given me. Also I would like to acknowledge that the mathematical model of albedo and formulas provided in chapter 3 of this thesis have been developed by Hesan Ziar. I want to thank the TU Delft Gamelab for allowing me to work or study at the office whenever I wanted. I also want to thank my friends who have always asked me how things are going with my thesis. I want to thank my family and especially my mother for her mental support, motherly love and prayers. Lastly, I want to thank my wife Liza for supporting me with everything that she has. Thank you for being so patient…

F.F. Sönmez
Delft, December 2017

Abstract

Despite the fact that the price per watt-peak for photovoltaic modules are decreasing rapidly, there is a large population of people which have still not implemented photovoltaic technology in their everyday lives. An important reason why PV is still not the main source of electrical energy for these people is the uncertainty that comes with installing a PV system on the roof of a house. Consumers are afraid that an investment in a PV system will cost them too much money, while it will take a long time before their investment is paid back for. Therefore, it is important to accurately estimate the energy yield of PV systems before installation. By doing so, consumers will be more likely to see the benefits of a PV system, thus implementing the technology on their houses.

This thesis aims to improve the accuracy of the annual energy yield estimation using LiDAR data and a new model for the albedo component of irradiance. LiDAR has been used to determine the irradiance on a surface previously, however, this thesis uses LiDAR data in the Unity 3D game engine, which enables the user to apply changes and build on the environment rapidly. This eliminates the disadvantage of LiDAR data, which is often outdated, thus missing crucial objects surrounding the location of the potential PV system.

Ray-casting is used extensively to determine the sky view factor, view factor, shading factor and to determine the surfaces visible to the PV module. Being able to determine the sky view factor without doing any field work greatly reduces the time required to design a PV system.

The albedo component is often neglected entirely when estimating the irradiation on a surface, while it may significantly contribute to the energy yield, reaching up to 10% of the total. The albedo component is mainly important for highly tilted PV modules or BIPV. The albedo component is also crucial for bifacial PV modules. Measurements have shown that the albedo of a material is not determined easily using a sample of the material along with two inversely installed pyranometers making up an albedometer. It has been found that the albedometer is only able to determine the specific albedo of a location for the weather condition and the time in which the measurement has been done. Extensive research has been done in order to determine the factors which have an influence on the albedo of a location. The spectral reflectivity of materials is expected to play an important role in finding a final model which describes the albedo factor accurately.

In order to estimate the irradiance due to reflectance, first the irradiance on the surfaces that are visible to the PV module are estimated one by one along with the view factor of each of the visible surfaces to the PV module in question. Finally using the reflectivity of the material of each surface, the contribution of each surface to the irradiance on the PV module as a result of reflectance is summed up resulting in the albedo component of the irradiance. The same method is used for the back side of the PV module to determine the irradiance on the back side of a bifacial PV module.

This research aims to play an important part in the automation of PV system design, striving to completely eliminate necessary field work, while improving the accuracy of the predicted annual energy yield.

Contents

List of Figures ix

List of Tables xiii

1 Introduction 1
- 1.1 Motivation 1
- 1.2 PVISION 2
- 1.3 Objectives and research questions 2
- 1.4 Thesis outline 3

2 Different components of irradiance 5
- 2.1 Irradiance 5
- 2.2 Clear sky models 6
  - 2.2.1 Direct normal irradiance 6
  - 2.2.2 Diffuse horizontal irradiance 7
- 2.3 Meteorological data 8
- 2.4 Global irradiance on a PV module 9
  - 2.4.1 Direct irradiance on a PV module 9
  - 2.4.2 Diffuse irradiance on a PV module 10
- 2.5 Conclusions 11

3 Albedo 13
- 3.1 Albedo 13
- 3.2 Different sources of albedo 13
  - 3.2.1 Albedo as a constant 13
  - 3.2.2 Range of albedo 13
- 3.3 Significance of albedo component 15
- 3.4 Measurements on albedo 15
  - 3.4.1 Experiment setup 16
  - 3.4.2 Measurement results and discussion 18
  - 3.4.3 Measurements conclusions 22
- 3.5 Spectral albedo 23
- 3.6 Importance of spectral albedo 26
- 3.7 Conclusions 29

4 LiDAR data and simulation framework 31
- 4.1 LiDAR 31
- 4.2 How does LiDAR work 31
- 4.3 What format does LiDAR use 31
- 4.4 Compatibility with Unity3D 32
- 4.5 LiDAR terrain in Unity3D 32
  - 4.5.1 Modification of terrain in Unity3D 33
- 4.6 Conclusions 34

5 Sky view factor 35
- 5.1 Geometric definition of the sky view factor 35
- 5.2 Sky view factor using the Meteonorm software 36
- 5.3 Sky view factor using Chronolux 36
- 5.4 Sky view factor using Unity3D with LiDAR data 37
- 5.5 Accuracy and simulation time of SVF with respect to amount of rays 39
- 5.6 Conclusions 40

6 View factor **43**
6.1 View factor . . . 43
6.2 Mathematical problem . . . 43
6.3 Reciprocity rule for view factors . . . 44
6.4 Numerical method for determining the view factor using the Riemann method . . 44
6.5 Determining the view factor using the Monte Carlo method . . . 44
6.6 Determining the view factor using ray casting . . . 44
6.7 Comparing the results of ray casting with exact solutions . . . 45
6.8 Using the reciprocity rule to determine the view factor from the surface to the PV module . . . 48
6.9 Conclusions . . . 48

7 Sun path **49**
7.1 Sun path . . . 49
7.2 Position of the Sun . . . 50
7.3 Shading factor . . . 52
  7.3.1 Shading analysis example . . . 53
7.4 Angle of incidence . . . 56
7.5 Simulation time steps . . . 58
7.6 Conclusions . . . 60

8 Irradiance prediction **61**
8.1 Irradiance prediction . . . 61
8.2 Irradiance prediction using existing models . . . 61
  8.2.1 The models used . . . 62
  8.2.2 Irradiance prediction using existing models results . . . 62
8.3 Irradiance prediction using the ray casting model . . . 63
  8.3.1 Albedo component using the ray casting model . . . 65
  8.3.2 Irradiance prediction using the ray casting model results . . . 67
  8.3.3 Comparison between the ray casting model and the existing model . . . 68
  8.3.4 Effect of albedo component on the irradiance . . . 68
8.4 Bifacial PV modules . . . 71
  8.4.1 Different configurations . . . 71
  8.4.2 Comparison between bifacial module and a monofacial PV module . . . 73
8.5 Conclusions . . . 74

9 Conclusions **77**
9.1 Recommendations . . . 78

Bibliography **81**

Appendices **85**

A Meteonorm data **87**

B Albedometer **93**

C Measurement results **97**

D Paper draft **103**

List of Figures

1.1 A study showing the increasing popularity of bifacial PV technology [1] 2

2.1 The spectral irradiance of the sun for different air masses and 6000K black body solar spectrum [2]. 6
2.2 An illustration of the air mass, where θ is the angle between the normal of the ground surface and the direction of the sun. 7
2.3 Locations of Meteonorm weather stations in west-Europe [3] 8
2.4 An illustration showing the three components of irradiance on a PV module G_M, their directions and their sources [4] 9
2.5 An illustration showing the three components of diffuse irradiance on a PV module G_M^{dif}, and their sources. 10
2.6 The extraterrestrial irradiance varying with respect to the day of the year [5]. 11

3.1 Albedo measurement of asphalt material for the entire day [6]. 14
3.2 A vertically mounted PV system in Edinburgh Napier University [7]. 15
3.3 Pueblos blancos, a village in Andalusia Spain. 16
3.4 Working principle of the albedometer. 16
3.5 The albedometer that was used for the measurements. 17
3.6 The albedo as a function of GHI for different reflecting surface sample orientations for set 1. 18
3.7 The albedo as a function of GHI for different reflecting surface sample orientations for set 2. 19
3.8 The albedo as a function of GHI for different azimuth angles of albedometer. 19
3.9 The albedo as a function of GHI for different albedometer heights. 20
3.10 The albedo as a function of GHI for different surface areas. 21
3.11 The albedo as a function of GHI for different materials for set 1. 21
3.12 The albedo as a function of GHI for different materials for set 2. 22
3.13 The albedo as a function of GHI for diffuse irradiation only. 23
3.14 The spectral reflectivity of green grass for the visible spectrum [8]. 24
3.15 The spectral irradiance of the AM1.5 spectrum [9]. 24
3.16 The spectral reflectivity of green grass for the spectrum of the albedometer (285nm to 2800nm) [8]. 25
3.17 The spectral irradiance curve of the direct normal, diffuse horizontal and the global horizontal component of the solar irradiance calculated by Solar Gate [10] from the data of Gueymard [11]. 25
3.18 The spectral irradiance curve of the direct normal irradiance for different air mass values calculated by Solar Gate [10] from the data of Gueymard [11]. 26
3.19 The spectral reflectivity of common solar PV farm materials [12]. 27
3.20 The spectral reflectivity of common rooftop materials [12]. 27
3.21 The spectral reflectivity of various commonly found materials [12]. 28
3.22 The EQE of different PV technologies [12]. 28
3.23 The effective albedo of common solar PV farm materials for different PV technologies [12]. 29
3.24 The effective albedo of commonly found materials for different PV technologies [12]. . 29
3.25 The effective albedo of common rooftop materials for different PV technologies [12]. . 30

4.1 Heightmap of the TU Delft campus in a PNG file format for a 780 meter by 482 meter area. 32
4.2 Unity3D game engine terrain of the EWI faculty building in the TU Delft campus 33
4.3 Google Maps terrain of the EWI faculty building in the TU Delft campus [13] 33

4.4 The unaltered simulation environment. 34
4.5 The altered simulation environment, where a block has been added, which represents a building. 34

5.1 Illustrating the definition of the sky view factor , which is the fraction of the celestial hemisphere enclosed by the thick red line [4]. 35
5.2 The plot of equation 5.1 for all angles of θ 36
5.3 The horicatcher tool of meteonorm with a digital camera and a horizon mirror [14]. . . 37
5.4 Sky view factor grid made by the horicatcher tool, which gives an SVF of 0.8896. . . . 37
5.5 An illustration showing how the distance between the end points of the rays become larger when the distance of the end points to the center of the sphere increases. . . . 38
5.6 SVF prediction by ray casting in the simulation using 50000 rays. 39
5.7 The SVF plot according to the simulation for a different number of total rays used. . . . 40
5.8 The difference of the SVF in % for a different number of total rays used. 41
5.9 The simulation time for the amount of rays used. 41

6.1 The view factor for a differential sphere dA_1 to sphere A_2 where h is the distance between differential sphere 1 and the center of sphere 2 which has a radius r. 45
6.2 Lambert's law showing how the reflected intensity decreases as the angle of the reflected beams increase with respect to the normal of the reflecting surface. 46
6.3 The view factor for a differential planar surface 1 to finite parallel rectangle surface 2 where normal of surface 1 passes through a corner of surface 2. 48

7.1 An illustration of the solar azimuth (A_s) and the solar altitude (a_s) [4]. 49
7.2 An illustration of the latitude (ϕ_0) and the longitude (λ_0) [15]. 50
7.3 An illustration of the apparent movement of the Sun around the Earth, where the vernal equinox is depicted with Υ and the axial tilt $\epsilon \approx 23.4$ degrees [4]. 51
7.4 An illustration of the hour angle h, GMST, LMST θ_L, right ascension α and longitude λ_0 [4]. 51
7.5 An illustration for the concept of shading factor. 52
7.6 The solar bike station with the EWI building to its southward direction. 53
7.7 An illustration showing the PV modules placed on the roof of the power station. 54
7.8 An illustration showing the PV modules placed on the roof of the power station for both spots, where the PV modules at the left hand side are the PV modules at the second spot and the PV modules at the right hand side are again the PV modules on the first or original spot. 55
7.9 An illustration showing the concept of the angle of incidence. 57
7.10 An illustration showing the angles regarding the PV module [4]. 58
7.11 The Sun path with a time step of 1 hour, where the Sun for each time step is illustrated as a yellow circle and the actual sun path is illustrated as a dotted arc. 59
7.12 The Sun path with a time step of 2 hours, where the Sun for each time step is illustrated as a yellow circle and the actual sun path is illustrated as a dotted arc. 59
7.13 The Sun hours for different latitudes per day, where the blue line indicates the latitude of New York [16]. 60

8.1 The power station used for the irradiance predictions, with the PV module depicted as a blue square [13]. 62
8.2 The direct component of irradiance per hour of a year for the existing model simulation. 63
8.3 The diffuse component of irradiance per hour of a year for the existing model simulation. 64
8.4 The albedo component of irradiance per hour of a year for the existing model simulation. 64
8.5 The total irradiance per hour of a year for the existing model simulation. 65
8.6 The surfaces visible to the PV module depicted by the red color with the PV module pointed by the arrow with latitude 51.999633 and longitude 4.368913 for the location. 66
8.7 Top view of the surfaces visible to the PV module depicted by the red color with the PV module pointed by the arrow with latitude 51.999633 and longitude 4.368913 for the location. 66
8.8 The direct irradiance per hour of a year for the ray casting model simulation. 67
8.9 The diffuse irradiance per hour of a year for the ray casting model simulation. 68

8.10 The reflected irradiance per hour of a year for the ray casting model simulation. 69
8.11 The total irradiance per hour of a year for the ray casting model simulation. 69
8.12 Albedo component share of total energy yield for different surface tilts. 70
8.13 Albedo component share of total energy yield for different albedo factors. 70
8.14 Bifacial PV modules mounted on a certain height above the ground [17]. 71
8.15 Vertically mounted bifacial PV modules [18]. 72
8.16 The visible surfaces to the backside of the bifacial PV module depicted in a red color. . 72
8.17 Albedo component share of total energy yield for the backside of a PV module for different tilt angles. 73
8.18 Reflected energy yield and the total energy yield on the backside of a PV module for different tilt angles. 73
8.19 Bifacial gain for different albedo factors and different tilt angles. 74
8.20 Energy yield of the front side, back side and both sides of a bifacial module for different tilt angles. 75
8.21 Energy yield of the bifacial PV module for different albedo factors and different tilt angles. 75

C.1 The albedo as a function of GHI for different reflecting surface sample orientations for set 1. 97
C.2 The albedo as a function of GHI for different reflecting surface sample orientations for set 2. 98
C.3 The albedo as a function of GHI for different azimuth angles of albedometer. 98
C.4 The albedo as a function of GHI for different albedometer heights. 99
C.5 The albedo as a function of GHI for different albedometer heights for grass only. 99
C.6 The albedo as a function of GHI for different albedometer heights for bitumen only. . . 100
C.7 The albedo as a function of GHI for different surface areas. 100
C.8 The albedo as a function of GHI for different materials for set 1. 101
C.9 The albedo as a function of GHI for different materials for set 2. 101
C.10 The albedo as a function of GHI for diffuse irradiation only. 102

List of Tables

3.1 Constant albedo factors of different materials [19]. 13
3.2 Range of albedo values of different materials according to Geem [20]. 14
3.3 Albedo factors of different materials according to PVPMC [5]. 14
3.4 The different materials for which the albedo measurements were done. 17

7.1 Shading factor of solar bike station in front of the EWI building. 54
7.2 Shading factor of the dual axis solar tracker in percentages. 55
7.3 Shading factor of the single axis solar tracker in percentages. 56
7.4 Shading factor of the dual axis solar tracker in percentages for the location at the back side of the roof behind the chimney. 57
7.5 Shading factor of the single axis solar tracker in percentages for the location at the back side of the roof behind the chimney. 58

8.1 The variables used to determine the irradiance on a surface. 63

1

Introduction

A photovoltaic (PV) module is irradiated by three different sources of irradiance. The most obvious source of irradiance comes directly from the sun, this is called the direct component of irradiance. The second source of irradiance is the diffuse component. This irradiance consists of light that has been scattered by particles in the air and by the clouds. The third source of irradiance is due to light that has been reflected from the environment.

Many researches have been done in order to determine the direct and the diffuse components. Several models have been proposed which accurately describe the direct and the diffuse components while the albedo component of the irradiance has been neglected by many. While the direct and diffuse components are known very well and can be estimated without the need of any fieldwork, the albedo component still requires much field work to accurately describe its behaviour. Even then, however, the slightest change in weather conditions or in the geometry of a location will disturb the estimations. This thesis proposes a model which describes the actual albedo component of the irradiance, by using LiDAR data along with ray casting. This model is also usable for bifacial PV modules for which it is hard to estimate the irradiance on the back side of the PV module, since it is heavily dependant on the albedo component of irradiance.

1.1. Motivation

Even though solar energy has been growing exponentially in the last decades, the vast majority of consumers still do not have a PV system providing electricity to their houses and businesses. However, this does not mean that people do not want solar panels. To the contrary, a study made by Motivaction [21] has shown that 9 out of 10 people in the Netherlands want more solar panels in the Netherlands, while half of the people want solar panels on their roofs. There is still too much uncertainty regarding solar energy. The reason behind this uncertainty is the speculation that solar panels will not pay back the investment fast enough. Also, consumers do not know the potential of solar panels well enough. Some companies have created software that is able to predict the annually produced electricity in order to assure consumers that their PV system will be functional and cost-effective. These predictions still are not made easy enough and/or accurate enough to fully convince all people to buy a PV system for their households. The albedo component of the irradiance is still too unpredictable to be trusted, while it may be well significant.

The significance is even more important for bifacial PV modules, which are currently on the rise in popularity according to ITRPV [1] as can be seen in figure 1.1.

It is therefore important to be able to accurately predict the irradiance received by a bifacial PV module. This research aims to create a model which describes the albedo component of the irradiance. This model has to allow the annual irradiance prediction without the need of fieldwork, which is very time consuming and expensive. Also it allows the irradiance prediction for the front side as well as the back side of a bifacial PV module.

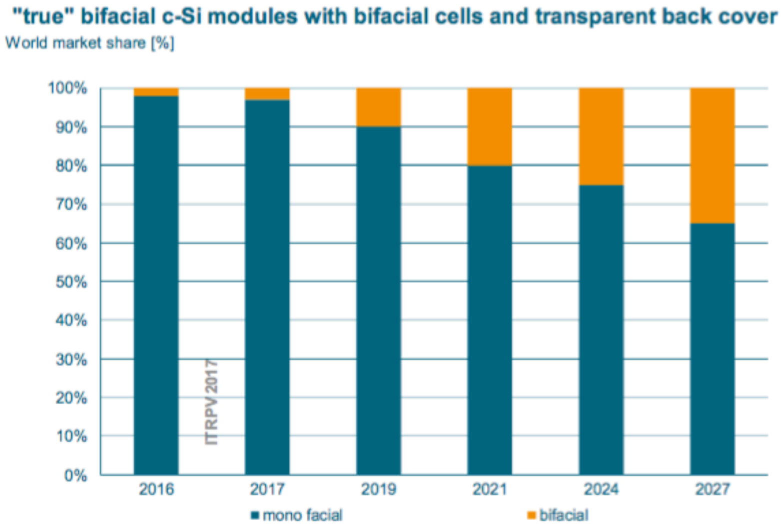

Figure 1.1: A study showing the increasing popularity of bifacial PV technology [1]

1.2. PVISION

This project is part of a larger project called Photovoltaic system installation optimization or PVISION. The aim of the project is to develop an innovative software solution that can efficiently (fully automated) design optimal PV systems for any location. This will lead to PV systems with a better performance (more kWh/kWp), lower acquisition costs for installation companies and more reliable data to boost the adoption of solar energy in the Netherlands [22]. The partners of this project are:
- Solar Monkey - A company focused on the development of software as a service to automatically calculate and design the best performing PV systems on any given location.
- Readaar - A company focused on the development of software that can analyze aerial photographs and 3D LiDAR-maps. These analyses contribute to the precision of the output calculations (predictions) for Solar Monkey.
- Delft University of Technology - A knowledge institution, for this project, focused on the energy yield modelling of custom PV systems, outdoor monitoring of PV systems and experimental validation of albedo recognition from aerial images. This research will validate and enhance the predictive power of the software of Solar Monkey and Readaar.
- University of Utrecht - A knowledge institution, for this project, focused on outdoor monitoring of PV systems on Utrecht university campus, analyses of performance data of residential systems, assistance with energy yield modeling.

As part of the Delft University of Technology this thesis has focused on parts of the PVISION project which include the energy yield modelling of PV systems Also, measurements have been performed in order to gain more insight into the albedo, which is an important aspect of the validation of albedo.

1.3. Objectives and research questions

The objective of this research is to allow for an automated PV system by eliminating several problems which are in the way of a software capable of estimating the annual energy yield of any location with great accuracy. This thesis focuses on the optical modeling. In order to achieve this objective, first a research goal has been defined, which includes all the essential parts of this thesis. The main research goal has been defined as:
- **Improve the automated design of custom PV systems by predicting the annual energy yield incident on a PV module including the albedo component of the irradiance which is also usable for bifacial PV modules.**

This research goal has been divided into sub-goals, which are all the necessary goals that are required for the main research goal. The subsequent sub-goals for the main research goal are:
- **Create a simulation which predicts the annual energy yield of a PV module by using me-**

teorological data.
- **Perform measurements and research literature to determine the albedo values of various materials which may be part of the field of view of a residential PV module.**
- **Improve the simulation by adding the albedo component.**
- **Improve the simulation by allowing the irradiance prediction for a bifacial PV module.**

These research goals have been written in terms of research questions. The resulting research questions are subsequently defined as:
- **How can the albedo component of the irradiance be estimated using the environmental factors without the need of field work?**
- **What are the parameters which have an effect on the albedo factor?**
- **How can the irradiance on the back side of a bifacial PV module be estimated?**

1.4. Thesis outline

In order to achieve a well organized structure, this thesis has been divided into multiple chapters. Chapter 2 is focused on providing the reader understanding in the basics of irradiance. Also, it shows several existing models which describe the direct and diffuse component of the irradiance.
The albedo is explained in detail in chapter 3, where different views on albedo are given. Measurements have been made which show that the albedo is a very complex concept. Then, an introduction to the spectral albedo is given which has the potential of describing the actual albedo using the reflectivity of the material.
In chapter 4, LiDAR data is explained along with the way that it is used in the simulation framework.
Chapter 5 explains the sky view factor, which is an important factor in the estimation of the diffuse component of the irradiance and it describes how the ray casting model is used to accurately determine the sky view factor.
Then, chapter 6 describes the view factor, which is important in the estimation of the reflected irradiance from a surface, that reaches the PV module, later used to estimate the albedo component of the irradiance. Again, the ray casting model is used to accurately determine the view factor.
Chapter 7 explains which model is used to determine the sun path and how it works. Next it shows how the sun path is used in determining the shading factor and the angle of incidence, which are both important in the estimation of the direct component of the irradiance.
Finally in chapter 8, the model is used for the estimation of the three components of the irradiance. The annual energy yield is determined using an existing model and the ray casting model, where after these are compared. Also, the ray casting model is used in order to determine the irradiance on the back side of a bifacial PV module, thus enabling the annual energy yield estimation for a bifacial PV module.

2

Different components of irradiance

This chapter aims to provide an understanding of the basics and principles of irradiance and the different components of irradiance. This chapter explains several models that are used currently and what their implications are. This chapter handles the subjects of clear sky models, meteorological data and the different components of irradiance excluding the albedo component, whereas the albedo will be handled in chapter 3. A final model used for the albedo component of the irradiance will be given in chapter 8.

2.1. Irradiance

The sun radiates as a black body at approximately 6000K. When reaching the atmosphere of the earth, the average irradiation of the sun is $1353 Wm^{-2}$ [2]. Finally, when passing through the atmosphere, light of different wavelengths are absorbed by various particles. This reduces the irradiation at surface level depending on the amount of atmosphere the light passes through. This is called air mass (AM). At the outside of the earth's atmosphere, the solar spectrum has AM0 and when the light passes through the atmosphere perpendicular to the surface of the earth, the solar spectrum has AM1. Depending on the angle in which the solar light passes through the atmosphere, the solar spectrum will be at least AM1 or larger [4]. The spectrum of the sun for two different air masses as well as the 6000K black body solar spectrum can be found in figure 2.1.

A part of the irradiance is directly reflected by the atmosphere of the earth, while another part of the light particles passes through the atmosphere without any interference. These light particles are considered to be moving parallel with respect to each other, because the distance between the sun and the earth is so great compared to the thickness of the atmosphere. Since these light particles are moving parallel to each other, some of the light is intercepted by an object (for example a tree), while some of the light are not intercepted and they are therefore radiated on a specific surface. This part of the solar irradiance is called the direct component.

Finally another portion of the light is scattered by the particles in the atmosphere. These particles can for example be air, dust or clouds. This part of the solar irradiance is radiated on a specific surface of the earth from the skies that are visible to the surface. Therefore this part of the solar irradiance is called the diffuse component.

Finally, the rest of the light particles that radiate on a specific surface are reflected from other surfaces. This is called the albedo component and it is generally the smallest part of the solar irradiance and the most complex to model. The albedo component will be handled in more detail in chapter 3.

There are several models to predict the annual irradiance on a surface, each having their own accuracies and focuses. Since there are three components for the irradiance, there are also different models for each of the components. Different models have different strengths and weaknesses for their own applications. In order to predict the annual irradiance on a surface, the instantaneous global horizontal irradiance (GHI) must be known. It is also possible to have the GHI in terms of time steps instead of having it instantaneous. The advantage of having the GHI in time steps is to be able to use different means to determine the GHI. The GHI is the sum of the direct, diffuse and albedo components. Having smaller time steps will increase the accuracy of a simulation, but it will increase the simulation

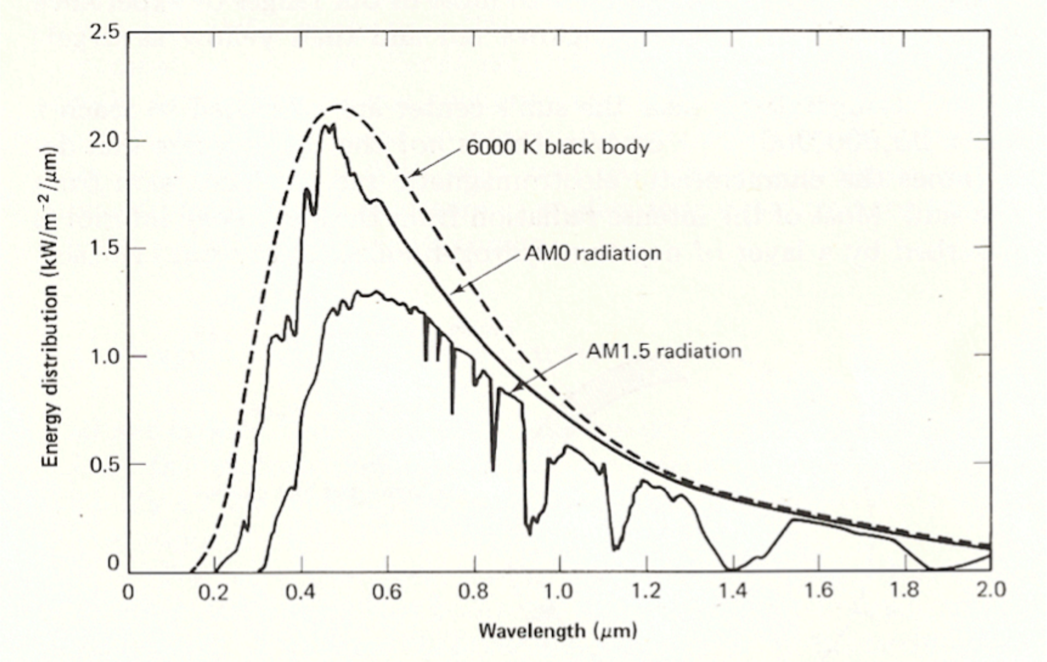

Figure 2.1: The spectral irradiance of the sun for different air masses and 6000K black body solar spectrum [2].

time. Often, the time step is limited by the data which is available. Meteonorm uses a time step of 1 hour as an example [14].

2.2. Clear sky models

There are several clear sky models to predict the direct normal irradiance and the diffuse horizontal irradiance. These models assume that the skies are clear from any clouds or other distortions. When the skies are considered to be clear, there is no need to account for situations that are complex to predict. Therefore, it becomes easier to create models for these situations. These models should be used with caution, because the skies are very often not clear and therefore these models would not work on those situations.

2.2.1. Direct normal irradiance

The direct normal irradiance (DNI) has often the most influence on the total irradiance on a surface. It is also the easiest to model since the incident power depends only on the angle between the normal of the surface and the sun. However, there are several factors which might block the incident power. One of these factors is the air mass which will block the irradiance of the sun. The AM depends on the amount of atmosphere (air) that the sun light has to pass through. The irradiance drops for an increasing path in which the sun light has to pass through the atmosphere. The AM is given by equation 2.1 [4].

$$AM = \frac{1}{cos\ \theta} = \frac{1}{sin\ \alpha_s} \tag{2.1}$$

Where θ is the angle between the normal of the ground surface and the direction of the sun. α_s is the altitude of the sun, which can also be used to express the AM. The altitude of the sun is related to angle θ as can be seen from equation 2.2.

$$\theta = 90 - \alpha_s \tag{2.2}$$

The concept of air mass is illustrated in more detail in figure 2.2.

From figure 2.2 it becomes clear how the sunlight path length changes depending on θ. Equation 2.1 does not take into account, the fact that the earth is round. When the curvature of the earth is

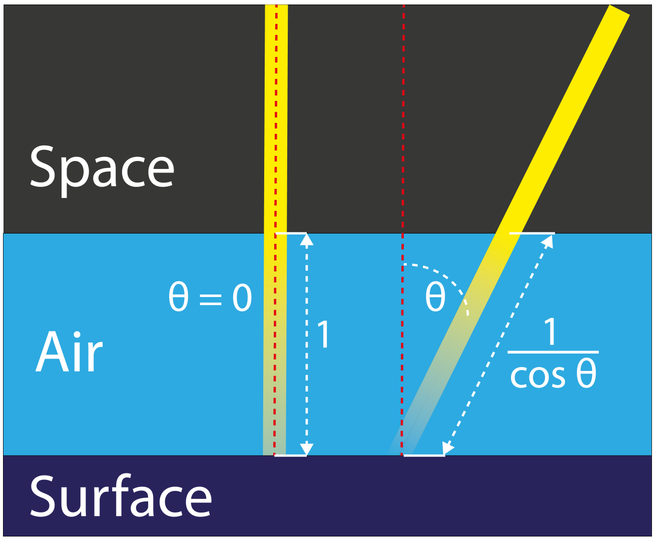

Figure 2.2: An illustration of the air mass, where θ is the angle between the normal of the ground surface and the direction of the sun.

also taken into account, the AM is defined in equation 2.3 [23].

$$AM = \frac{1}{sin\ \alpha_s + 0.50572(6.07995 + \alpha_s)^{-}1.6364} \tag{2.3}$$

According to Laue [24], the DNI is then influenced by the air mass in accordance with empirical equation 2.4.

$$I^{dir} = I^0[(1 - ch)0.7^{(AM^{0.678})} + ch] \tag{2.4}$$

Where I^0 is the solar constant 1353 Wm^{-2}, c is a constant of 0.14 and h is the height of the observer above sea level in km. This is however only applicable in the case when there are no clouds in the skies and if the diffusion percentage is low [4].

Another model is the so called ESRA model by Rigollier et al. [25]. This model as is given by equation 2.5 is accurate for high diffusion percentages as well.

$$I^{dir} = I^0\ \eta\ sin\ AOI\ exp[-0.8662\ T_L(AM2)\ m\ \delta_R(m)] \tag{2.5}$$

where η is the correction for the variations of the annual earth-sun distance, $T_L(AM2)$ is the Linke turbidity factor(a convenient factor to model the scattering of light for AM2), m is the relative optical air mass and $\delta_R(m)$ is the integral Rayleigh optical thickness.

2.2.2. Diffuse horizontal irradiance

The second largest component of the irradiance is the diffuse horizontal irradiance (DHI). The DHI consists of all incident light which is scattered by particles in the atmosphere. The European solar radiation atlas (ESRA) model proposed by Rigollier et al. [25] has a diffuse component as well.

$$I^{dif} = I^0\ \eta\ \frac{Dl}{2\pi}\ T_{rd}(T_L(AM2))[D_0\ \omega + D_1\ sin\ \omega\ + D_2\ sin\ 2\omega]_{\omega_1}^{\omega_2} \tag{2.6}$$

A more elaborated overview on the ESRA models can be found from Rigollier et al. [25].

An approximation of the diffuse component for a PV module perpendicular to the sun is given by PVEducation [9].

$$I^{dif}\ \approx\ 0.1 \cdot I^{dir} \tag{2.7}$$

which shows that during clear sky conditions, the diffuse component is approximately 10% of the DNI. Equations 2.6 and 2.7 only give the DHI for a case in which the surface has no obstructions from the surroundings. The DHI is provided by all parts of the skies that are visible to a surface. This means that the diffuse irradiance will be lower for an area in which there are more trees, buildings etc. In order to correct for this factor, the sky view factor (SVF) is used. A more elaborate explanation on the SVF will be given in chapter 5.

2.3. Meteorological data

Another method of obtaining the DNI and the DHI is by using meteorological data. Meteorological data can be obtained from different sources. Koninklijk Nederlands meteorologisch instituut (KNMI) is an institution in the Netherlands which can provide hourly data for the wind speed, wind direction, temperature, solar irradiation, the amount or rain, the amount of mist and several other weather parameters [26].
Another source of meteorological data is ESRA, but it is only available in book form and CD-ROM [27].
There are many more sources for different locations on the world each with their priorities. Meteonorm is available on most populated areas on the world and also it can deliver the relevant hourly data for PV applications. By interpolating between 3 or more Meteonorm weather stations, the data for a specific location is found. Figure 2.3 shows the locations of Meteonorm weather stations in western Europe.

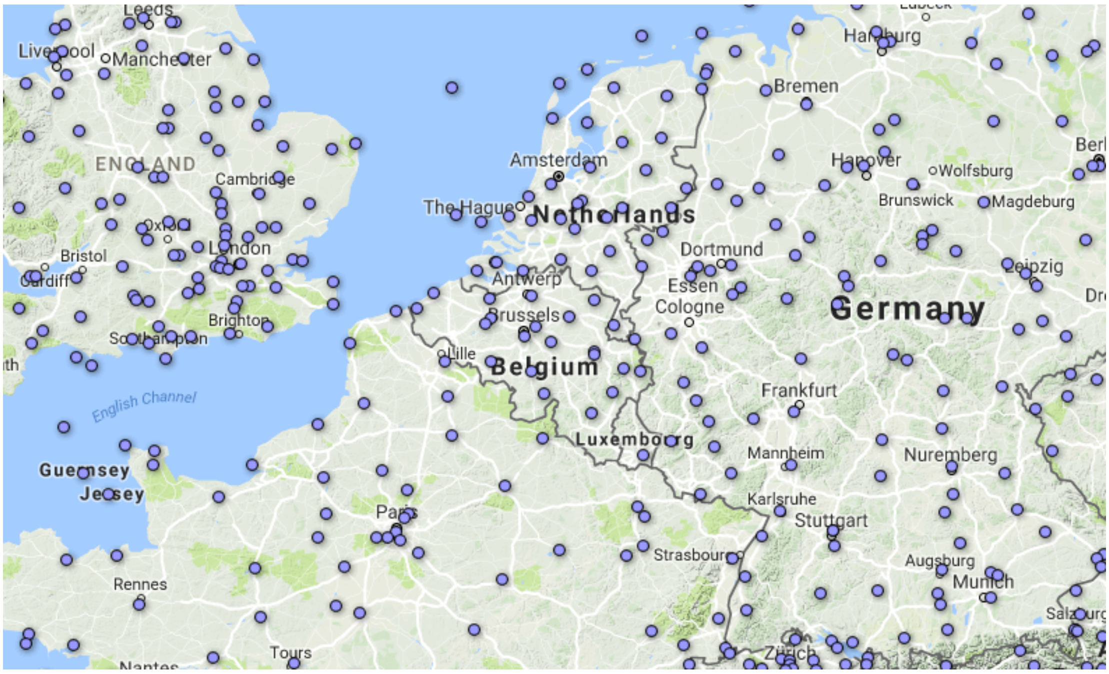
Leeds
Liverpool
Manchester
ENGLAND
Cambridge
Oxford
London
Bristol
Cardiff
Brighton
Southampton
English Channel
Guernsey
Jersey
Rennes
Nantes
Tours
Paris
Lille
Belgium
Brussels
Antwerp
The Hague
Amsterdam
Netherlands
Luxembourg
Dortmund
Essen
Cologne
Bremen
Hamburg
Hanover
Wolfsburg
Brunswick
Magdeburg
Leipzig
Germany
Frankfurt
Mannheim
Karlsruhe
Stuttgart
Nuremberg
Strasbourg
Augsburg
Munich
Zürich
Salzburg

Figure 2.3: Locations of Meteonorm weather stations in west-Europe [3]

Meteonorm is also available as an application programming interface (API) to connect to an external software, making it a good option to use for automated PV system design applications [3].
The DNI and DHI are obtained from meteorological data on approximately the surface level and therefore it is not necessary to account for the atmospheric effects. This makes it a very convenient source of irradiance.
There are different ways of obtaining the meteorological data. Meteonorm uses ground stations, aerosols and satellites to obtain their data. The three methods are combined to fill in the gaps for locations where there is no data of and also to validate other sources of data. For each of the data that Meteonorm provides, also a certain accuracy is provided. This inaccuracy can be up to 6% for locations in the Arctic circle, which are harder to measure. An example of the meteorological data of a city in the Arctic circle can be seen in appendix A. For the most northern city in the world ,Longyearbyen, the inaccuracy of the Meteonorm data for the GHI is 6%. In locations for which there is a greater density of measurement stations, the inaccuracy will decrease. Also, the accuracy will increase for locations which are closer to a measurement station. Nonetheless, the weather can still not be predicted with great accuracy one year into the future. Therefore, the meteorological data is based upon average data of the past. For example, the average of the years 1995-2005 is taken. The irradiance might change from one year to another, but when looking at an average of 10 years, the differences are small since the climate does not change in such a short amount of time.

2.4. Global irradiance on a PV module

Once the DNI and the DHI are known, the next step is to determine the effect of these components on a specific surface, since each surface has different parameters which influence the irradiance. These parameters are the angle of incidence (AOI), SVF, shading factor (SF), albedo component and AM. More parameters are possible for more complex models. To find the final irradiance G_M on the PV module, the three components of irradiance must be determined and summed [4].

$$G_M = G_M^{dir} + G_M^{dif} + G_M^{albedo} \tag{2.8}$$

The direct component as well as the diffuse component will be handled in this section, but the albedo component will be explained in more detail in chapter 3. An illustration of the three components of irradiance on a PV module can be seen in figure 2.4 [4].

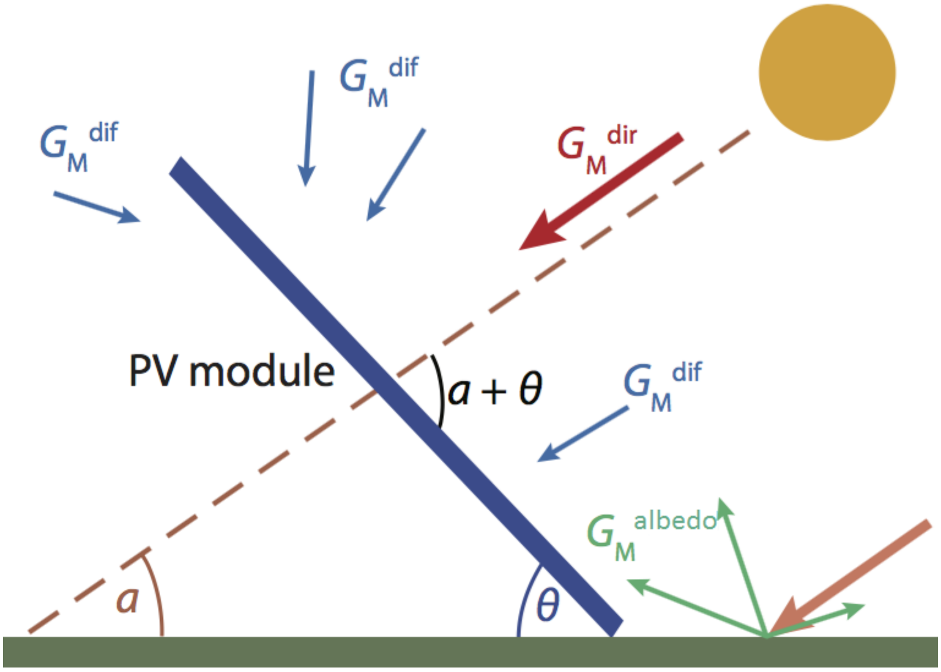

Figure 2.4: An illustration showing the three components of irradiance on a PV module G_M, their directions and their sources [4]

2.4.1. Direct irradiance on a PV module

Since a PV modules is often set up on an angle θ from the ground, the DNI must be corrected for it as the effective irradiance of the direct component of the irradiance decreases with respect to the angle. This angle is the AOI. The AOI will be handled in more detail in chapter 7. The direct irradiance on a module G_M^{dir} is consequently given by equation 2.9 [4].

$$G_M^{dir} = DNI \cos AOI \tag{2.9}$$

This equation assumes that the PV module is flat. In a case for which the PV module is not flat, other approaches are necessary. Since most of the PV modules are flat, this approach is sufficient to use.
The DNI is not always able to reach the PV module from the sun, because there are often obstructions which block the sun. These obstructions may cast a shade on the PV module, thereby eliminating the DNI. These obstructions will block the sun depending on the altitude and azimuth of the sun on a certain time. Therefore, the shading factor (SF) is introduced. Since the altitude and azimuth of the sun depend on the time of the day, so does the SF. Equation 2.9 is now altered in such a way that it includes the SF and it is given by equation 2.10.

$$G_M^{dir} = DNI\ (1 - SF) \cos AOI \tag{2.10}$$

When the shading factor is 1, the PV module will be completely blocked from the DNI, thus a structure will cast a shade over the entire PV module. This will happen for example, when there is a large building

between the PV module and the sun. The three parameters which determine the G_M^{dir} all change with respect to the time.
In chapter 7 the AOI and SF will be handled in more detail.

2.4.2. Diffuse irradiance on a PV module

The diffuse component is more complex than the direct component and thus there are more models which try to describe it accurately. The complexity of the model often describes the accuracy which is achieved, because it is often closer to reality. There are three components which describe the behaviour of the diffuse component. According to Reindl the three components are the isotropic radiation, circumsolar and horizontal brightening [28]. The three components of the diffuse irradiance are illustrated in figure 2.5.

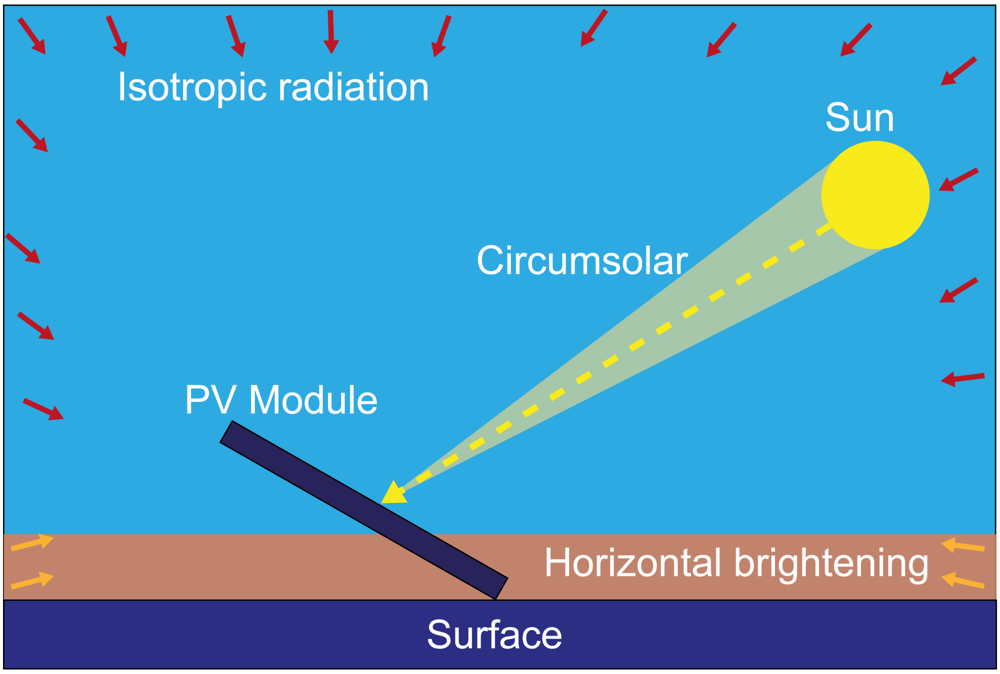

Figure 2.5: An illustration showing the three components of diffuse irradiance on a PV module G_M^{dif}, and their sources.

The isotropic component assumes that all parts of the sky emits the light in an isotropic way, or uniformly distributed in all directions. The circumsolar component is the light that is scattered due to aerosols in the atmosphere which mainly emits light in the area around the sun. The horizontal brightening is the increase in light emission in the air right above the horizon [28]. The correction coefficient which all of the diffuse irradiation models have is the SVF.
Noorian et al has performed a study on 12 different diffuse models to determine which delivers the best accuracy. From their study, the Reindl model is one of the models which shows the closest results to the measured diffuse component [29].

Isotropic sky model

The simplest diffuse model is the isotropic sky model, which only requires the SVF. As its name states, it considers the diffuse light across the sky to be isotropic and therefore uniform from all directions. The only factor that has influence on the diffuse component is the SVF [5]. The isotropic sky model is defined by equation 2.11.

$$G_M^{dif} = DHI\ SVF \tag{2.11}$$

Reindl diffuse model

The Reindl model is a so called anisotropic model, which means that it does not consider the light to come from all directions uniformly. According to Loutzenhiser et al. the Reindl model is especially useful for tilted PV modules [30]. This makes the model especially useful for northern locations. As an example the Reindl model is suitable to use for a location in the Netherlands. According to the Reindl model, the diffuse irradiation on a PV module is given by equation 2.12 [5].

$$G_M^{dif} = DHI\left[A_i \cos AOI + (1 - A_i)SVF\left(1 + \sqrt{\frac{DNI \cos \theta_Z}{GHI}} \sin^3 \frac{\theta_M}{2}\right)\right] \tag{2.12}$$

Where DHI and DNI can be obtained from meteorological data, the AOI is obtained from the sun path and the tilt of the module, while the tilt of the module is either a constant if the PV module has no solar tracker or it also changes with respect to the solar position, θ_Z is the solar zenith angle and θ_M is the tilt of the PV module. Finally, the index A_i is defined in equation 2.13

$$A_i = \frac{DNI}{E_a}, \tag{2.13}$$

where E_a is the extraterrestrial irradiance. The extraterrestrial irradiance is the irradiance of the sun at the top of earths atmosphere varying with respect to the distance between the earth and the sun. The variance of this irradiance is due to the elliptical orbit of the earth around the sun. The extraterrestrial irradiance is given by equation 2.14

$$E_a = I^0 \frac{R_{av}}{R}, \tag{2.14}$$

where R_{av} and R are the mean sun-earth distance and the real sun-earth distance respectively. The quadratic coefficient is given by equation 2.15

$$\frac{R_{av}}{R} = 1.00011 + 0.034221 \, cos \, b + 0.00128 \, sin \, b + 0.000719 \, cos \, 2b + 0.000077 \, sin \, 2b \tag{2.15}$$

and finally b is given by equation 2.16

$$b = \frac{DOY}{365} 360 \tag{2.16}$$

where DOY is the day of the year. The extraterrestrial irradiance is plotted in figure 2.6 [5].

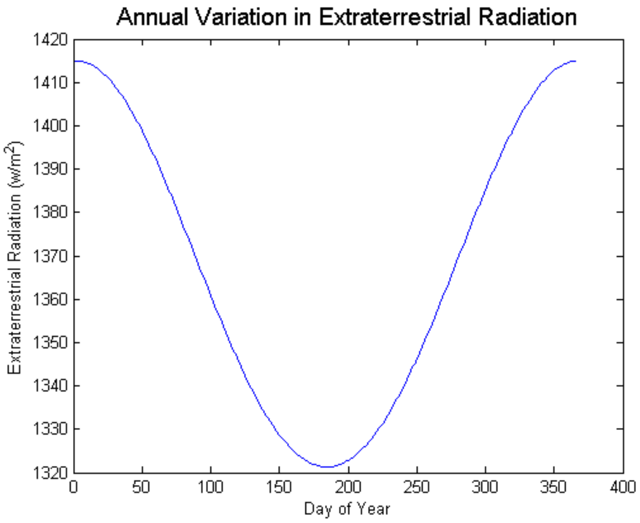

Figure 2.6: The extraterrestrial irradiance varying with respect to the day of the year [5].

2.5. Conclusions

Since the meteorological data for most locations is widely available and since the accuracy of meteorological data from Meteonorm is relatively high, this is the data that will be used to determine the irradiance on a surface. The DNI and the DHI will be used as an input for each time step. It is important that for the simulation the environmental impacts are shown. Factors such as the shading factor and sky view factor are important location dependant factors. In order to determine the direct component of the irradiance, equation 2.10 will be used. For the diffuse component of the irradiance, the aim is to show the difference in the effects of the sky view factor, therefore the isotropic sky model will be used even though the Reindl diffuse model is more suitable for tilted surfaces. The goal of this thesis is not to prove which diffuse model works best, but to show that a PV system should be designed location specifically.

3
Albedo

This chapter aims to give a clear understanding of the complex concept which is the albedo. First the definition of albedo is given, where after the different sources of albedo are shown along with the albedo factors that they claim for different materials. The measurements that have been done for this thesis are explained in detail and finally results and conclusions of those results are shown. As a conclusion, a new concept is introduced which is the spectral albedo. The spectral albedo is a concept which has the potential to describe the albedo factor in a more usable way.

3.1. Albedo

Albedo is a Latin term which is translated as whiteness. A more elaborate definition is given by Coakley [31]: "The albedo of a surface is the fraction of the incident sunlight that the surface reflects". The part of the incident sunlight which is not reflected is absorbed, since no energy is lost. The definition results in equation 3.1 for albedo:

$$\alpha = \frac{\phi_{reflected}}{\phi_{incident}}, \tag{3.1}$$

where $\phi_{reflected}$ and $\phi_{incident}$ are the reflected radiation from a surface and the incident irradiation on a surface respectively. The incident irradiation consists of the direct and the diffuse component. However, the incident irradiation may also consist of light reflected from other surfaces.

3.2. Different sources of albedo

3.2.1. Albedo as a constant

The albedo factor is often regarded as a constant value in literature. This means that if the incident irradiation halves, the reflected radiation is halved as well as a consequence. An example of constant albedo values for different materials can be found in table 3.1.

Table 3.1: Constant albedo factors of different materials [19].

Material	**Albedo (%)**
Grass	14
Dry Soil	16
Dry Sand	35
Wet Sand	20
Tall Grass	17
Water	5

3.2.2. Range of albedo

More often, a range is assigned to the value of albedo. As an example, Geem [20] claims that the albedo of aged concrete is in the range of 20% to 30%. A list of ranges of albedo can be found in table 3.2 [20] and a list of constant and ranges of albedo values can be found in table 3.3 [5].

Table 3.2: Range of albedo values of different materials according to Geem [20].

Material	Albedo (%)
Aged concrete	20-30
New concrete	40-50

Table 3.3: Albedo factors of different materials according to PVPMC [5].

Material	Albedo (%)
Urban environment	14 – 22
Grass	15 – 25
Fresh grass	26
Fresh snow	82
Wet snow	55-75
Dry asphalt	9-15
Wet Asphalt	18
Concrete	25-35
Red tiles	33
Aluminum	85
Copper	74
New galvanized steel	35
Very dirty galvanized steel	8

Coakley [31] claims that the albedo changes with respect to time of the year and according to Gueymard [32] the albedo changes with respect to time of the year as well as the time of the day. Also according to Wang [6], the albedo changes with respect to time of the day as his measurements show in figure 3.1.

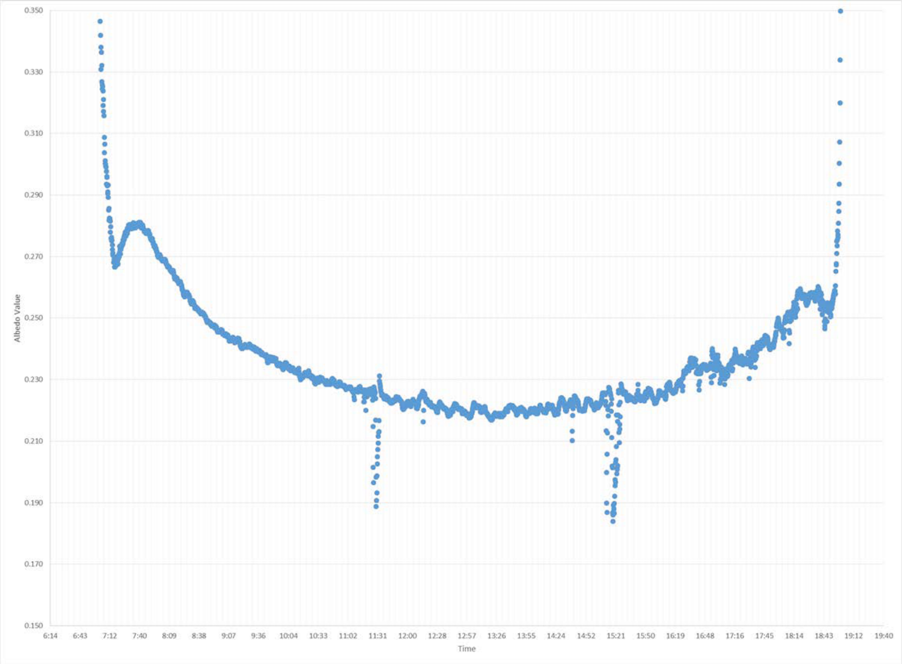

Figure 3.1: Albedo measurement of asphalt material for the entire day [6].

From all this discrepancy between the different findings of different literature, it can be concluded that albedo is a very complicated concept.

3.3. Significance of albedo component

According to Ineichen et al. [33], the irradiance as a result of albedo can be up to $100W\ m^{-2}$ for certain scenarios. Kotak et al. [7] has found values in the range of $45.2Wm^{-2}$ to $92Wm^{-2}$ depending on the albedo of the materials of the surroundings. When considering an AM1.5 solar spectrum with a $1000Wm^{-2}$ irradiance, the albedo component would in those scenarios result in 10%, 4.5% or 9.2% of the total irradiance, respectively. When ignoring the albedo effects in the estimation of the yearly energy yield, this might thus result in a significant estimation error for such scenarios. This displays the importance of including the albedo component in the energy yield estimation in certain scenarios. One of the scenarios in which the albedo might play a significant role in the energy yield of a PV system is for vertically mounted PV modules as was used in the example of Kotak [7]. An example of a facade PV system can be seen in figure 3.2.

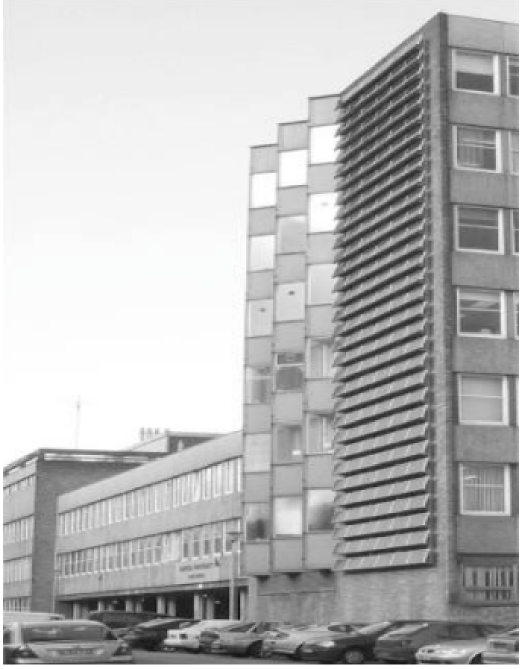

Figure 3.2: A vertically mounted PV system in Edinburgh Napier University [7].

Another case for which the albedo component will be significant is for a location in which the area is very white i.e. an area in which there are many white buildings, high albedo roads, pavements etc. An extreme example of such an area would be the so called ”pueblos blancos” in Andalusia Spain as can be seen in figure 3.3.

While snow may block light entering the PV module, it is a very highly reflective material and therefore if the PV module is clean, fresh snow will boost up the irradiance on a PV module as a result of albedo. Albedo is important to consider when estimating the irradiance on a monofacial PV module, however, it is even more important for bifacial PV modules. Bifacial PV modules are able to allow light to enter from both sides of the PV module. Light entering the PV module from the back side is often reflected from the ground behind the PV module. The higher the albedo of the ground, the higher the total irradiance on the PV module. This could be achieved by painting the surface on which the bifacial PV module is mounted in a high albedo paint.

3.4. Measurements on albedo

Measurements were done in order to determine the albedo factor of various materials which can be found in urban areas. The albedo factor of many of these materials are given in literature, however, from section 3.2 it can be concluded that there is too much uncertainty about reliable results.

Figure 3.3: Pueblos blancos, a village in Andalusia Spain.

3.4.1. Experiment setup

The measurement was done using an albedometer from Kipp en Zonen [34]. An albedometer is in fact made up from two pyranometers, one facing upward and one facing downward, where the upward facing pyranometer measures the direct and diffuse irradiation of the sun and the downward facing pyranometer measures the reflected irradiation. This has been illustrated in figure 3.4.

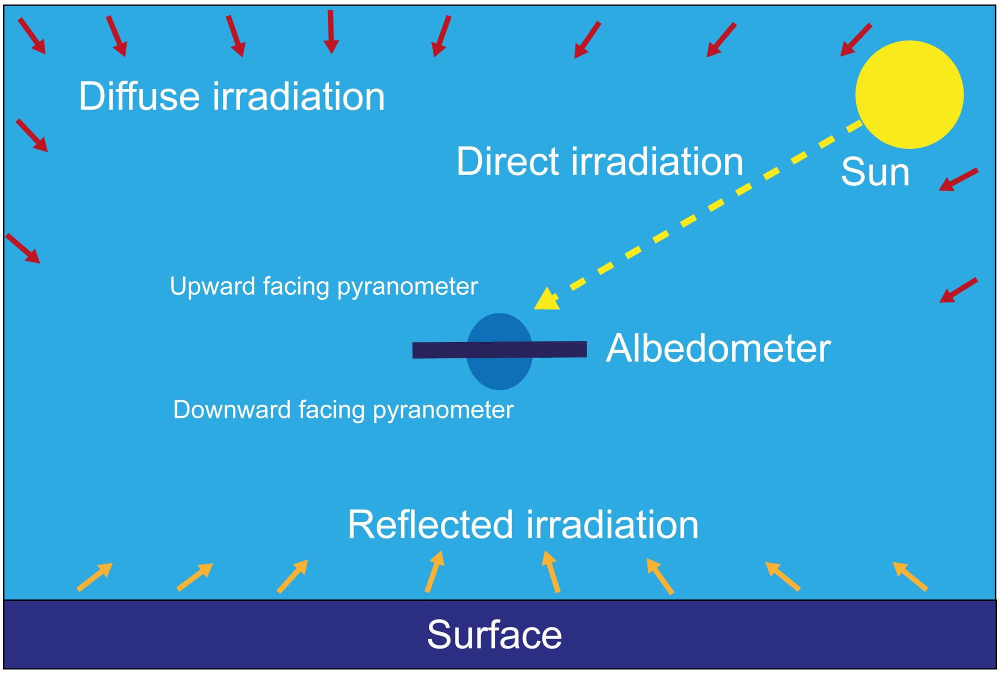
Diffuse irradiation
Direct irradiation
Sun
Upward facing pyranometer
Albedometer
Downward facing pyranometer
Reflected irradiation
Surface

Figure 3.4: Working principle of the albedometer.

The data sheet of the albedometer can be found in appendix B. The albedometer that was used can be seen in figure 3.5.

Materials

The materials that are used for the albedo measurements can be found in table 3.4 along with the surface area of the materials that are used.

All experiments consist of a series of reference measurements, which implies a measurement done

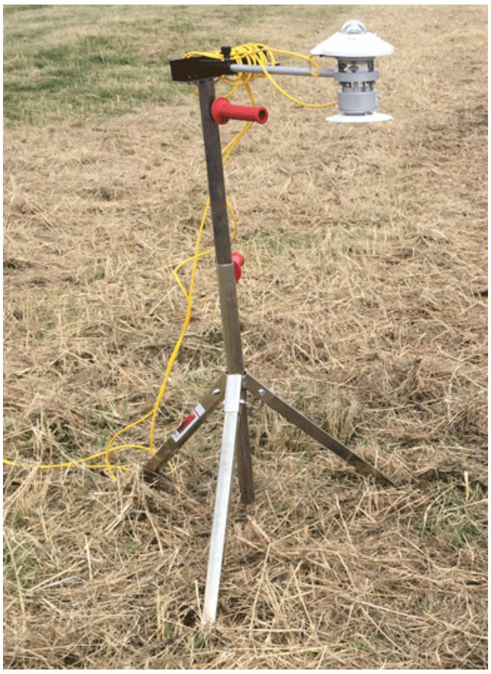

Figure 3.5: The albedometer that was used for the measurements.

Table 3.4: The different materials for which the albedo measurements were done.

Material	**Area (m^2)**
Green grass	-
Dry grass	-
Plastic	1
Bitumen	0.48
Red tiles	0.28
Black tiles	0.32
Metal	0.14
White coated metal	0.18
Gray coated metal	0.13
Gravel	0.51

without a material sample. Since the location in which the measurements are performed consist of either green or dry grass, these are the materials which are referred to as reference materials in the results.

Neglected effects

The following effects are neglected for the measurements:
1. The measurements were done on a wide flat area in which the effect of far located objects are neglected,
2. The roughness effects of the land has been neglected,
3. The inhomogeneity of the land has been neglected.

Changing parameters

In order to determine the influent factors for albedo, many different experiments were performed. For the different experiments one parameter is changed while the other parameters are kept constant.

1. Changing the orientation of the materials,
2. Changing the azimuth of the albedometer,
3. Changing the height of the albedometer,
4. Changing the area of the reflective surface,
5. Changing the reflective surface materials,
6. Measuring for diffuse only conditions.

It should be noted that, further experiments and investigations were performed to develop a more comprehensive model for albedo. More details can be found in appendix D which is potentially the draft material for a future possible publication.

3.4.2. Measurement results and discussion

The albedo results of the measurements were plotted as a function of the global horizontal irradiance, which is the irradiance received on the top part of the albedometer. This was done in order to see the change in albedo as a result of the change in irradiation. It should also be noted that the pyranometers that are used for the measurements give the irradiance Wm^{-2} in whole numbers. This means that especially in the low irradiance regions, the albedo seems to oscillate significantly. If the upper pyranometer registers an increase of $2Wm^{-2}$, the lower pyranometer might still not register any change, which results in a decreasing albedo reading. This does not mean, however, that the irradiance incident on the lower pyranometer did not increase, but the increase is not enough to be shown.

Changing the reflecting surface sample orientation

First the effect of the change in sample orientation is measured. The plotted results of this measurements can be seen in figures 3.6 and 3.7.

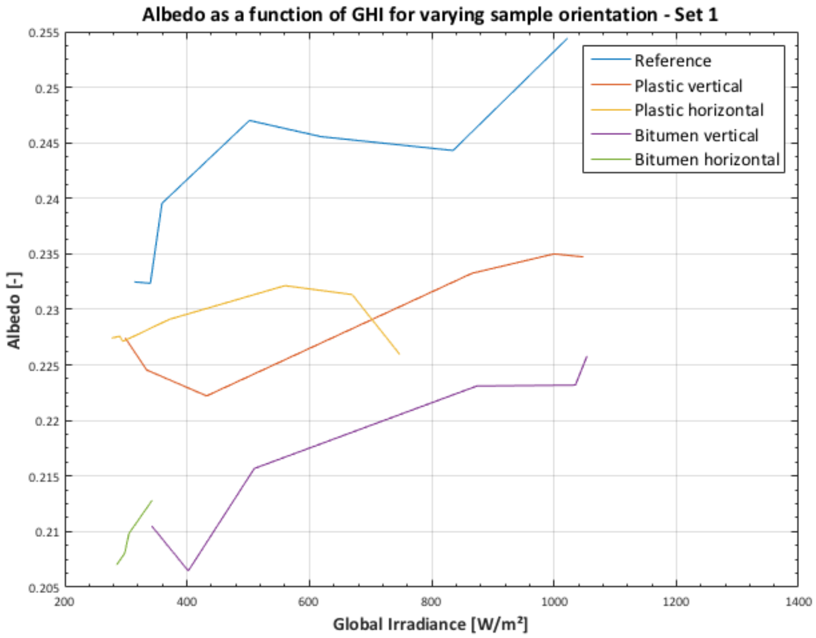

Figure 3.6: The albedo as a function of GHI for different reflecting surface sample orientations for set 1.

Changing the orientation of the reflecting surface samples do not seem to have influence on the albedo of the material. For plastic, the plot for both orientations are very close to each other. The plots cross each other on 2 locations for both sets of orientations. Especially in figure 3.7, it becomes very clear that there is no significant gap between the lines. In the case of bitumen, the results are less

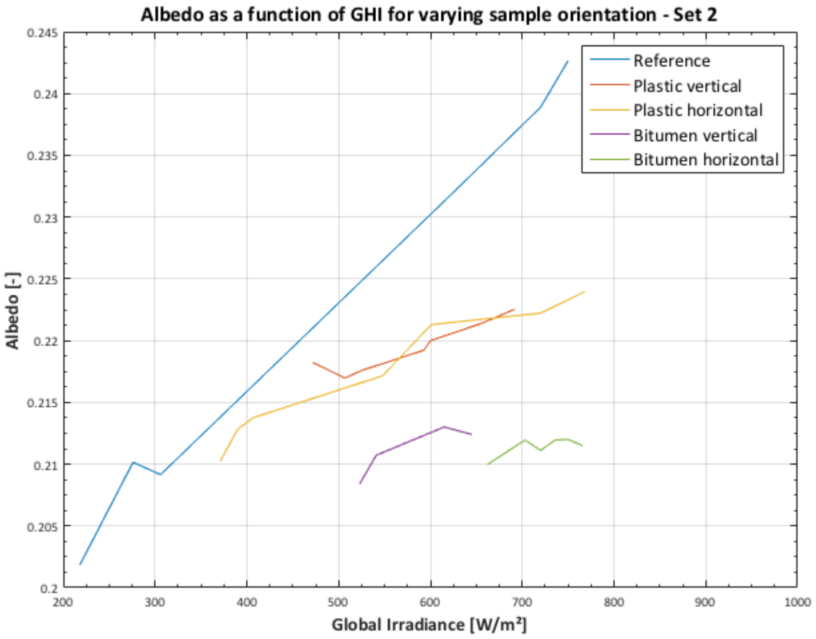

Figure 3.7: The albedo as a function of GHI for different reflecting surface sample orientations for set 2.

clear, since the results of both measurements do not overlap each other. However, also for bitumen, the gap between the plots are insignificant.

Changing the azimuth of the albedometer

The effect of the azimuth of the albedometer is tested by directing the albedometer in the direction of the sun for one series of measurements, while changing the direction of the albedometer by 45 degrees for another series of measurements.

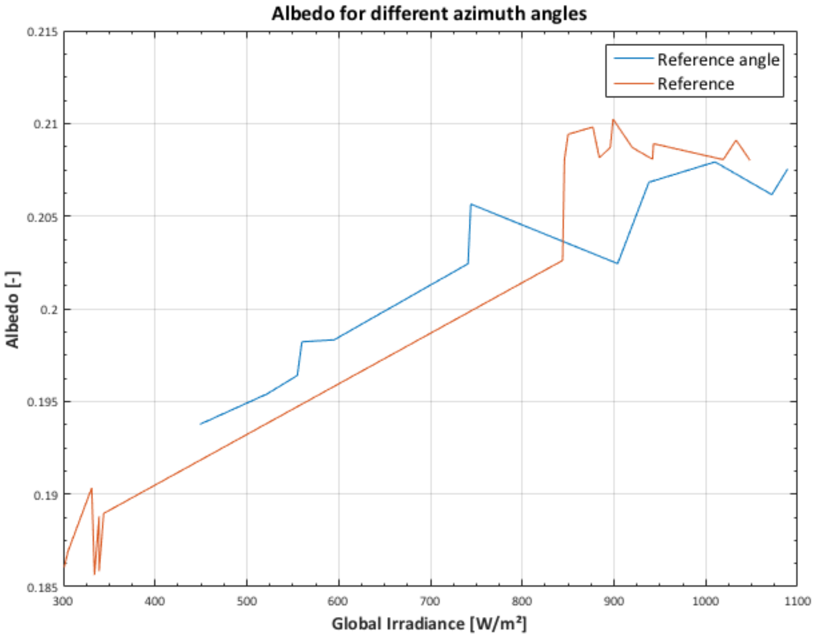

Figure 3.8: The albedo as a function of GHI for different azimuth angles of albedometer.

From the results of 3.8 it seems that the azimuth of the albedometer has no influence on the value of albedo.

Changing the height of the albedometer

The measurements are performed by setting the albedometer up on different heights from the reflecting surface. These measurements are done for the reference material as well as for bitumen. For each series of measurements, the height was increased by approximately 10cm. The minimum height for the albedometer was 92cm from the reflecting surface sample, up to a maximum height of 160cm.

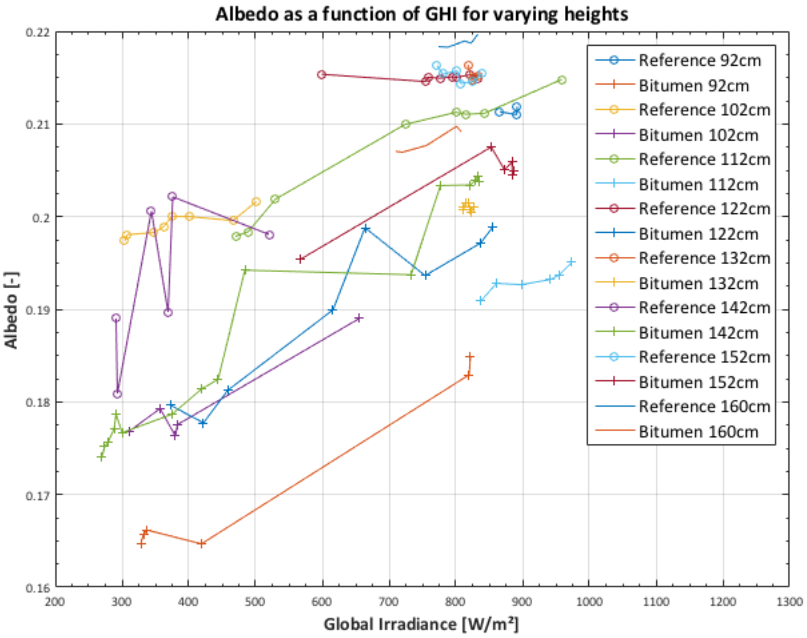

Figure 3.9: The albedo as a function of GHI for different albedometer heights.

To see the results for the reference material and for bitumen separately, see appendix C. Changing the height of the albedometer with respect to the reflecting surface material seems to have little influence on the reference material, since the maximum difference of albedo is found to be approximately 0.01 between the measurements regarding the reference material. For the bitumen material, however, the maximum difference of albedo is approximately 0.03, which is more significant. Interesting to see is that for the highest position for the albedometer, the bitumen material has the closest albedo as compared to the reference material, while for the lowest height, the difference between the reference material and the bitumen is largest. This makes sense, because the view factor of the bitumen sample is much larger when it is closer to the albedometer. Since, the bitumen has a lower albedo than the reference material, which is green grass, the albedo reduces when the albedometer height is reduced.

Changing the area of the reflective surface

The plastic material is cut up for different surface areas in order to find the effect of changing the surface area of the reflective surface material. These measurements are only performed for plastic along with a series of reference measurements.

Plastic has a lower albedo than the reference material. A larger plastic sample therefore results in a lower albedo, while decreasing the size increases the albedo up to the point where the albedo is the same as for the reference material. The reference measurements are very concentrated, therefore the measurements of the reference do not overlap the measurements of the smaller surface area plastic. In the case of changing the surface areas, the view factor is affected in the same way as in the case when the height of the albedometer was changed. The view factor increases for an increasing reflective surface area, causing the albedo to decrease when the albedo of the reflective surface area is lower than the reference material and increase when it is higher.

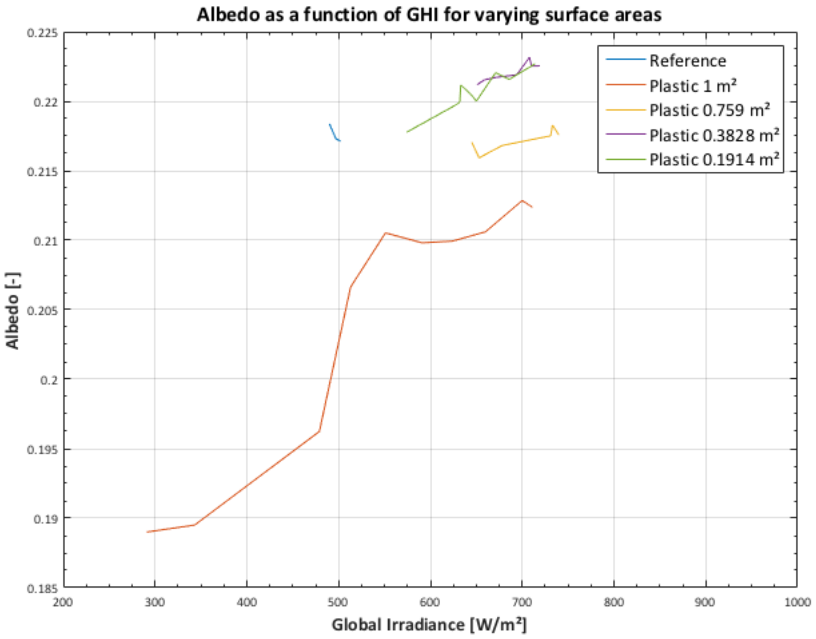

Figure 3.10: The albedo as a function of GHI for different surface areas.

Changing the reflective surface materials

A series of albedo measurements were done for different surface materials including the reference material. These measurements are done by placing the different reflecting surfaces directly under the albedometer. The albedo measurement results can be found in figures 3.11 and 3.12.

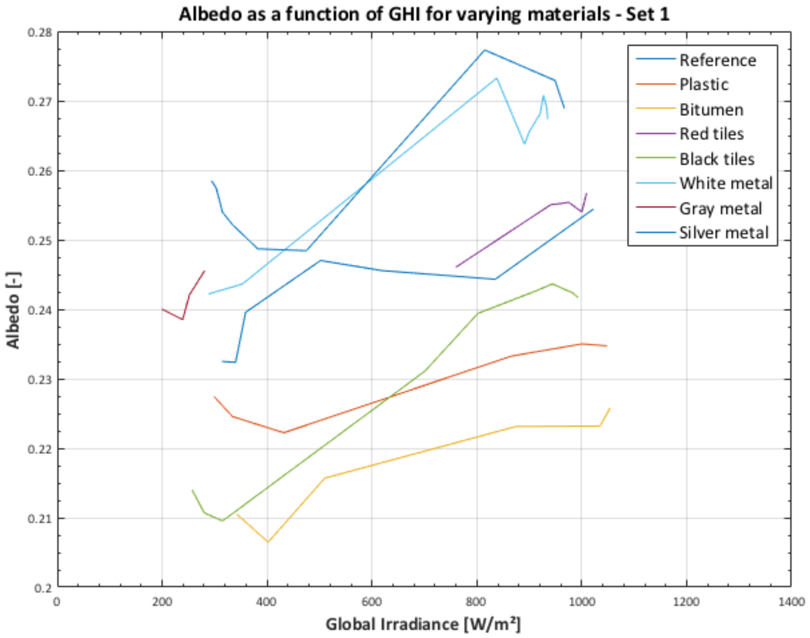

Figure 3.11: The albedo as a function of GHI for different materials for set 1.

It is interesting to see which materials have an higher albedo as compared to other materials. The albedo values displayed in the graphs are however not the actual albedo values of the materials except for the reference material, which is dry grass. This is due to the areas of reflecting surface materials,

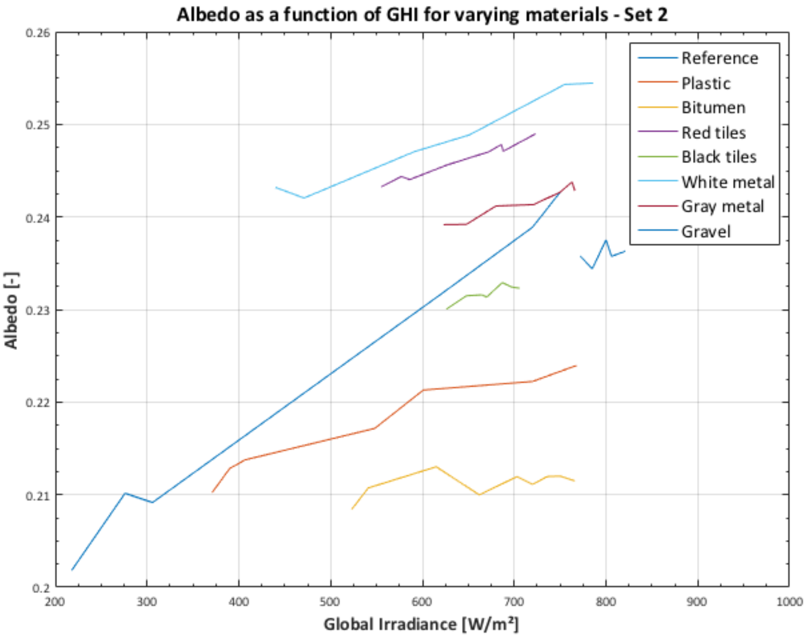

Figure 3.12: The albedo as a function of GHI for different materials for set 2.

causing the view factor to not be 1. In fact, the albedo displayed in the graphs are a mix between the albedo of dry grass and the corresponding reflective surface material. However, there is still important information to be found from the plots. The albedo clearly seems to be a variable instead of a constant.

Measuring for diffuse only conditions

Finally a series of albedo measurements are done on a cloudy day, where the direct component of the irradiance is assumed to be negligible in comparison to the diffuse component, therefore only diffuse irradiance is incident on the upper pyranometer as well as on the surfaces. Figure 3.13 shows a series of albedo measurements for two materials including the reference material for overcast sky conditions.

The albedo of the different reflecting surface materials do not significantly change for a change in GHI. The maximum difference in change is observer for bitumen, where the difference is approximately 0.006. It seems that the albedo is constant for diffuse irradiance.

3.4.3. Measurements conclusions

The measurements have shown that first of all, the sample orientation and changing the azimuth of the albedometer has no significant effect on the albedo. The albedo seems to increase as the GHI increases. From the results of the albedo measurements regarding the changing height of the albedometer, as well as the changing area of the reflective surface, it can be concluded that the view factor from the albedometer to the reflecting surface is one of the key factors that determine the albedo of a surface. Another factor which has influence on the albedo is the irradiance on the upper pyranometer as well as on the reflecting surfaces. Also the weather conditions play a role in determining the albedo, since the albedo behaves differently under cloudy conditions as the albedo seems to become constant when there is only diffuse irradiation. In order to measure the albedo of a reflecting surface it seems that it is important to consider a whole range of irradiances, as well as different weather conditions and the view factor of the reflecting surface should approach unity. In all other cases, the albedo that is measured will give the albedo for that exact location and the corresponding time of the day and time of the year in which the measurements were done. The measured albedo can then be used to determine the irradiance as a result of reflectance, but only for that specific time and location in which the measurements are performed. Even in such a case, a change in the environment will consequently change the albedo. If the albedo of all the materials in the surroundings would be known, including the exact geometry of all the surfaces and the instantaneous irradiances and weather conditions, the

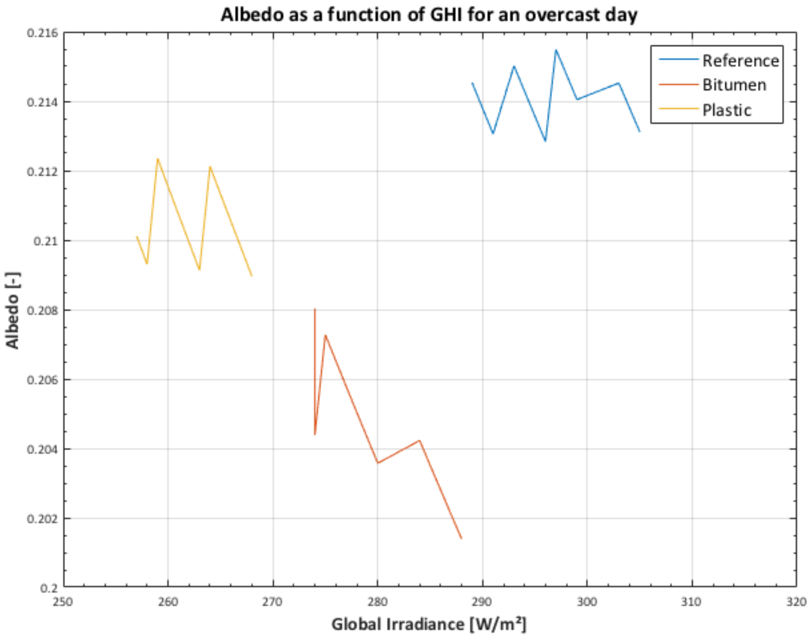

Figure 3.13: The albedo as a function of GHI for diffuse irradiation only.

irradiance as a result of reflected light can then be determined. If a change in the environment would occur, only that change would have to be implemented in the model to determine the new albedo.

3.5. Spectral albedo

Until now, the albedo factor has been determined for the spectral range of the albedometer, which is 285nm to 2800nm as can be found in appendix B. The fraction of the reflected light can also be considered as spectral reflectance, or reflectance per wavelength [12]. As an example, grass reflects light mainly in the green part of the spectrum, which is the spectrum between 495nm and 570nm. Logically, this is the reason why grass has the color green. The spectral reflectivity of green grass can be seen in figure 3.14.

The increase in reflectivity in the green part of the spectrum is partly responsible for the green color of grass. This does of course not mean that grass only reflects in the green part of the spectrum. Clearly the red part of the spectrum has a relatively high albedo according to figure 3.14, from which it would seem that grass should in fact be red. However, the spectral irradiance of the sun is not evenly distributed over the whole spectrum. The green part and the blue part of the AM1.5 spectrum are larger than the red part as can be seen from figure 3.15.

The combined reflected wavelengths of all spectra result in the green color of grass which humans observe. The main spectrum in which green grass reflects light is in the infrared and the microwave spectra. This can be clearly seen in figure 3.16.

When integrating the spectral reflectivity of green grass for the spectral range of the albedometer, the value that is obtained is 19.74%. However, the reason why the albedometer does not always show an albedo value of 19.74 for green grass is due to the changing solar spectrum. Both the direct and the diffuse component of the solar irradiance have a different spectral irradiance curve. This can be seen in figure 3.17.

Also, the solar spectrum of the direct component is greatly dependent on the air mass as can be seen in figure 3.18.

The received power is the result of a combination of the DNI spectrum as well as the DHI spectrum. Since the spectral irradiance received by the grass changes all the time due to changing weather conditions and a changing air mass, so does the measured albedo change continuously. According to

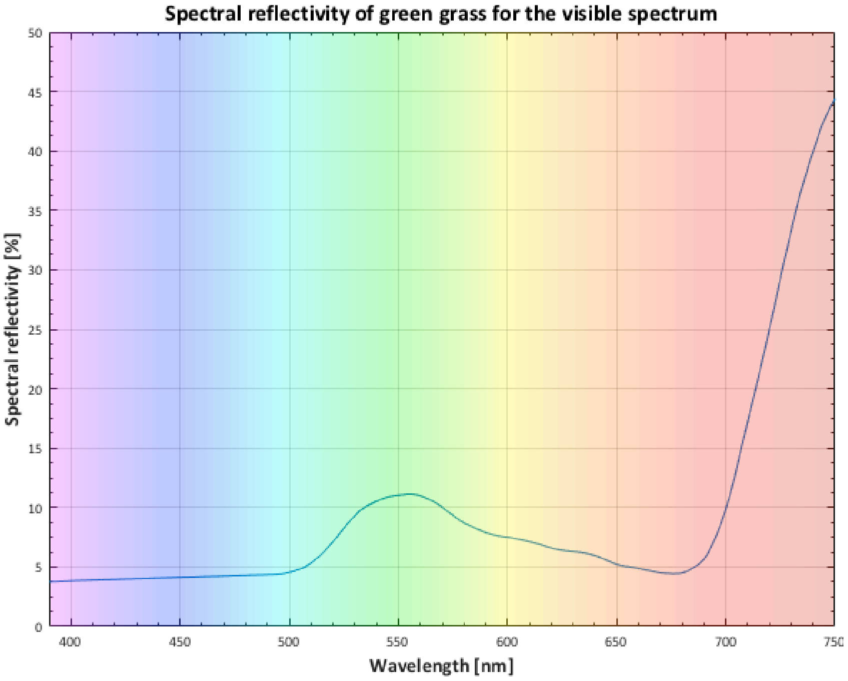

Figure 3.14: The spectral reflectivity of green grass for the visible spectrum [8].

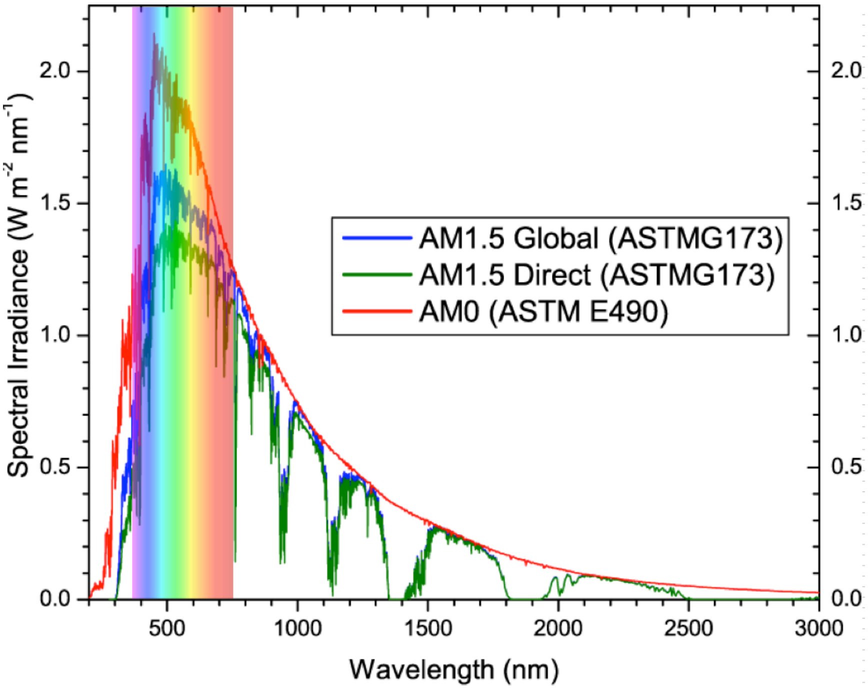

Figure 3.15: The spectral irradiance of the AM1.5 spectrum [9].

the paper draft of appendix D, the albedo can be written as in equation 3.2.

$$\alpha = R\left(F_{S\to A_1} + \frac{1}{H+1}F_{S\to A_2}\right), \tag{3.2}$$

where

$$R = \frac{\int R(\lambda)G(\lambda)\,d\lambda}{\int G(\lambda)\,d\lambda}, \tag{3.3}$$

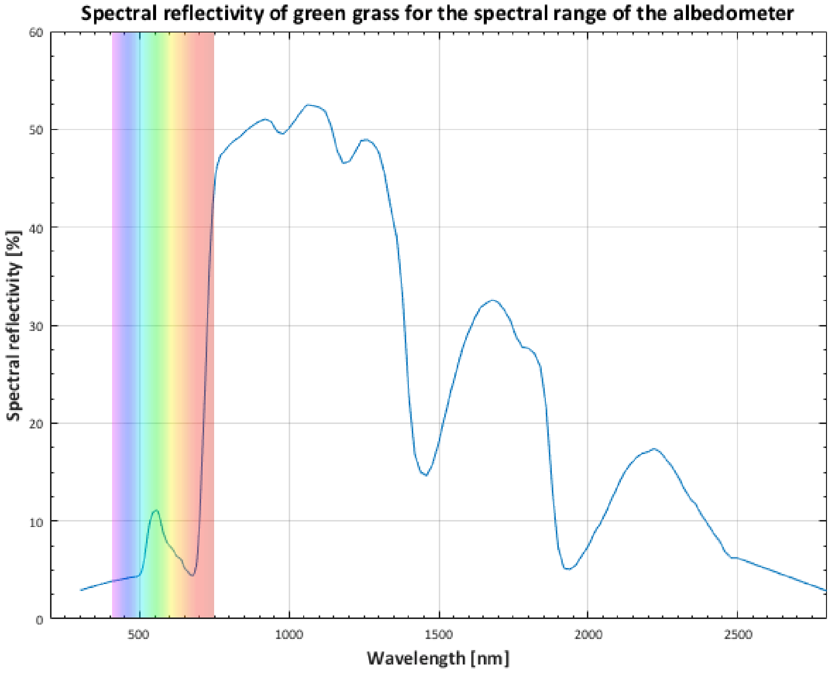

Figure 3.16: The spectral reflectivity of green grass for the spectrum of the albedometer (285nm to 2800nm) [8].

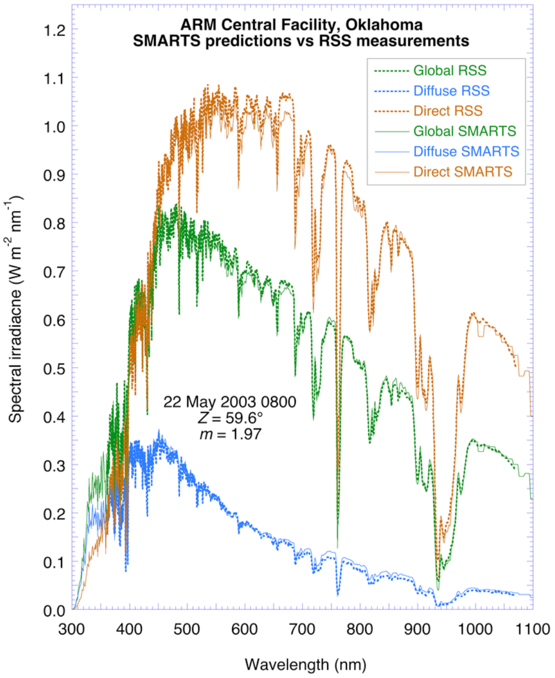

Figure 3.17: The spectral irradiance curve of the direct normal, diffuse horizontal and the global horizontal component of the solar irradiance calculated by Solar Gate [10] from the data of Gueymard [11].

R(λ) is the spectral reflectivity found in the ASTER data [8] and G(λ) is the spectral irradiance. F$_{S\rightarrow A_1}$ is the view factor from the albedometer to the non shaded areas, while F$_{S\rightarrow A_2}$ is the view factor to the shaded areas. Finally, H is defined as:

$$H = \frac{DNI\ \cos(AOI)}{DHI}. \tag{3.4}$$

Now it becomes clear that the albedo is indeed dependant on the reflectivity. Also, when there are

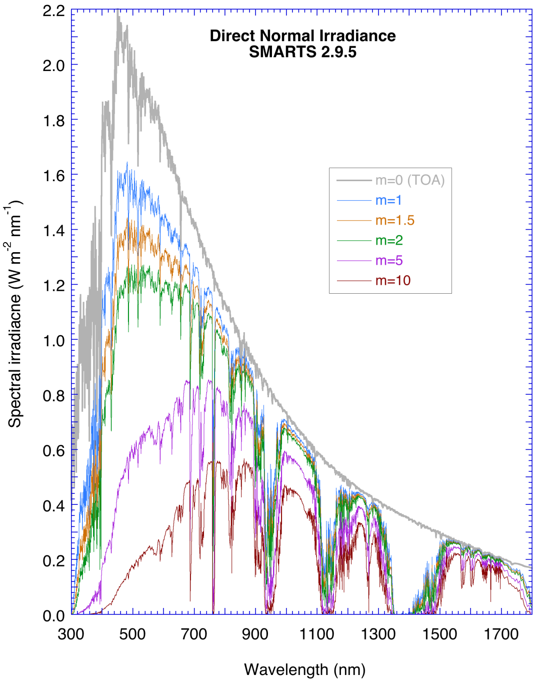

Figure 3.18: The spectral irradiance curve of the direct normal irradiance for different air mass values calculated by Solar Gate [10] from the data of Gueymard [11].

no shaded areas, the view factor of the shaded areas are consequently 0, while the view factor of the non shaded areas become 1 by definition. Therefore the albedo becomes the same as the reflectivity. However, the albedo cannot become larger than the reflectivity resulting in:

$$\alpha \leq R. \tag{3.5}$$

In literature, the term albedo of a material is often used to describe the fraction of light which is reflected from a material, when in fact it is not the albedo, but the reflectivity, which is the property of a material. Albedo is dependent on the reflectivity of the material. What is measured by an albedometer, however, is the albedo and it should be used in PV systems to determine the power which is reflected.

3.6. Importance of spectral albedo

Considering spectral albedo can alter the resulting power output of a PV system. Different PV technologies hold different band gaps. A band gap is the minimum energy of a photon that is needed for a valence electron to become a conduction electron, upon which the electron becomes free to move and become a charge carrier to conduct electricity. The photons with an energy below the band gap of the PV cell will simply either be reflected or become thermal energy. The photons with an energy above the band gap are eligible to be absorbed by the absorber material of the PV cells. In order to increase the usable part of the spectral irradiance, the chosen PV technology could be based on the spectral reflectivity of the materials in the surroundings. This enables a better optimization of PV system design, because it enables the selection of PV materials based on the environment in which it will be placed. This is especially important for bi-facial modules and vertically mounted PV modules, but it may also be important for PV modules with a high tilt, which is common in the northern latitudes [12].

The spectral albedo of various common urban materials can be found in figures 3.19, 3.20 and 3.21.

When comparing the spectral albedo of different materials to the external quantum efficiency (EQE) of different PV technologies it becomes more clear which PV technology should be used for the reflecting surface material. The EQE curves of different PV technologies can be seen in figure 3.22.

Combining the EQE of different PV technologies and the spectral reflectivity of surface materials, Brennan [12] has found the effective albedo of the materials for each of the PV technologies as can be seen in figures 3.23, 3.24 and 3.25.

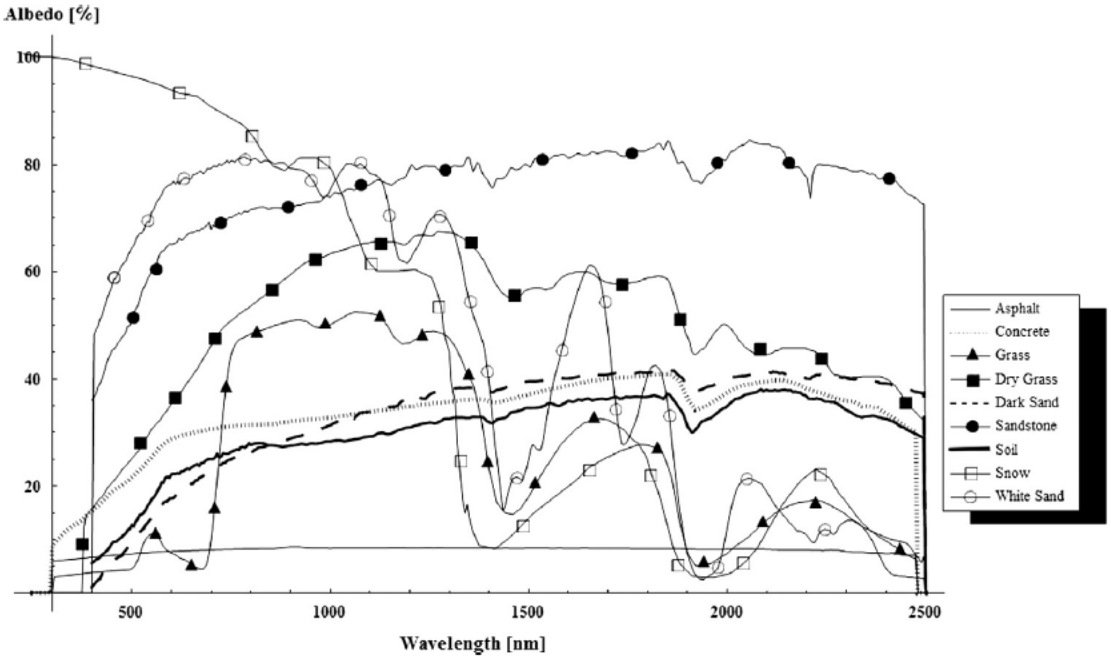

Figure 3.19: The spectral reflectivity of common solar PV farm materials [12].

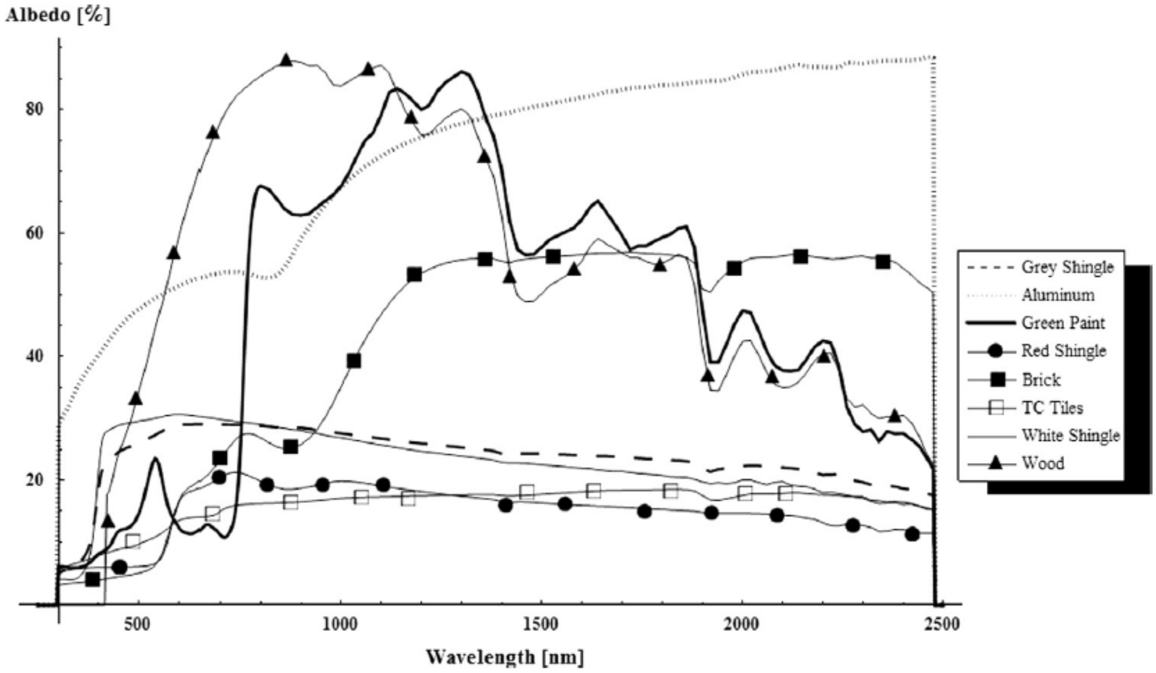

Figure 3.20: The spectral reflectivity of common rooftop materials [12].

For most PV technologies the effective albedo is relatively the same for different materials, however, in the case of paint, grass, brick and wood, the differences can be substantial. As an example, amorphous silicon or organic PV technology should not be combined with a grassy environment. Crystalline silicon or micro crystalline silicon perform best in the case of grass, with an effective albedo of approximately 0.28, while amorphous silicon has an effective albedo of approximately 0.09. Choosing the right PV technology might increase the irradiance as a result of reflectance by as much as 3 times. Also for other reflective surface materials it can be important to choose the right PV technology for that

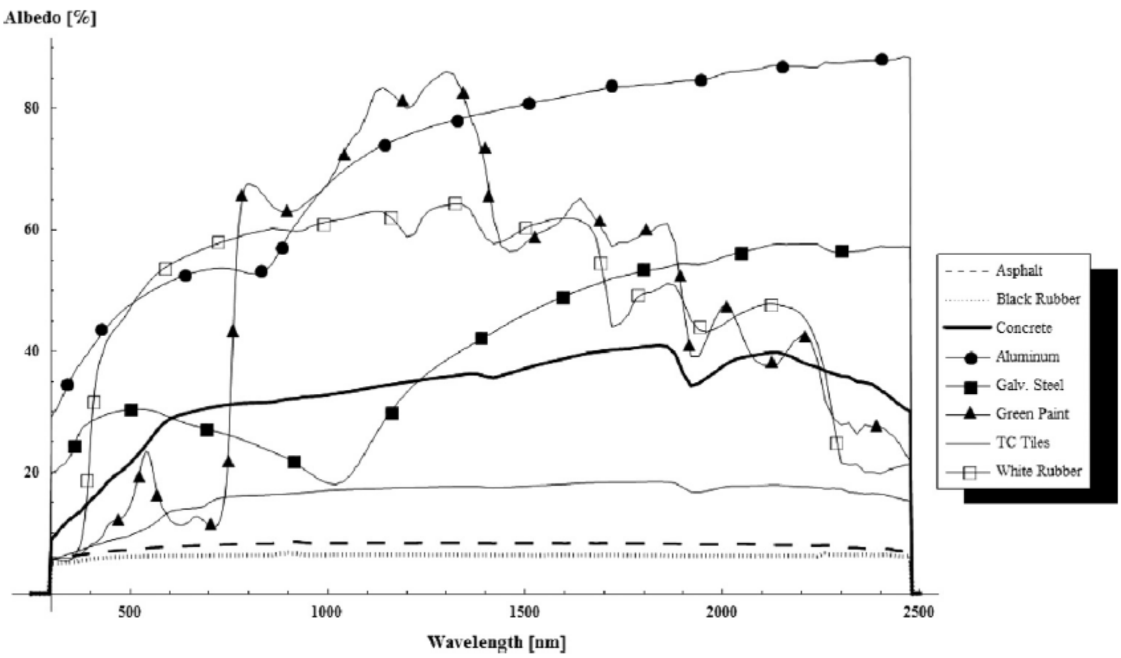

Figure 3.21: The spectral reflectivity of various commonly found materials [12].

Figure Captions

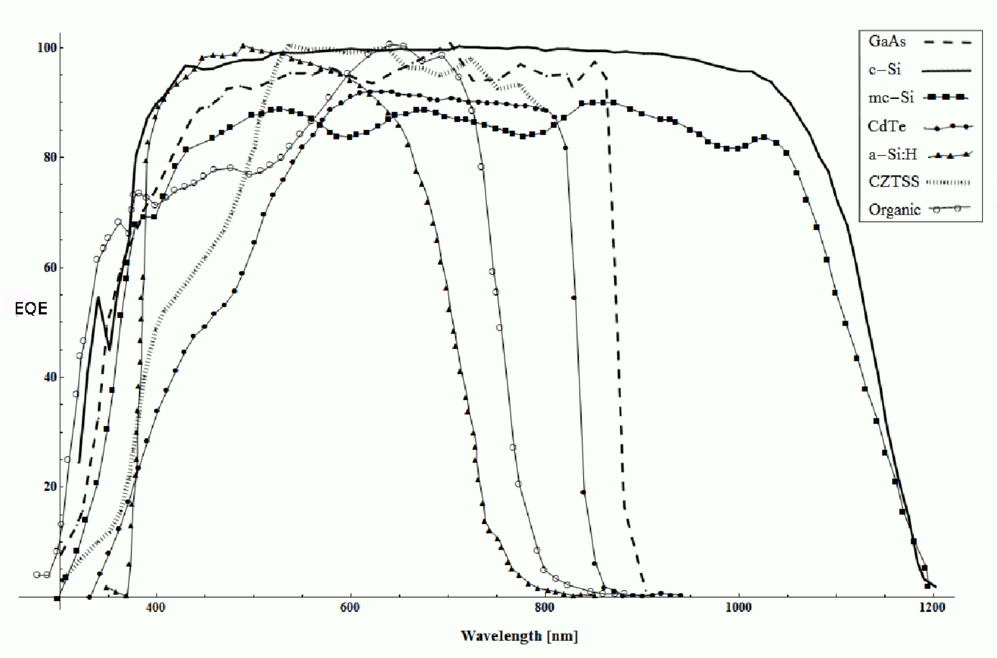

Figure 3.22: The EQE of different PV technologies [12].

environment.

According to Russell [35], especially for bifacial modules, the power output can be increased significantly by choosing the correct material for the environment. The output power can be increased by 7.5% and 4% by choosing snow and white sand, respectively. The power output may also be decreased when choosing the wrong material for the environment. As an example, red bricks might decrease the output power by 2.9%.

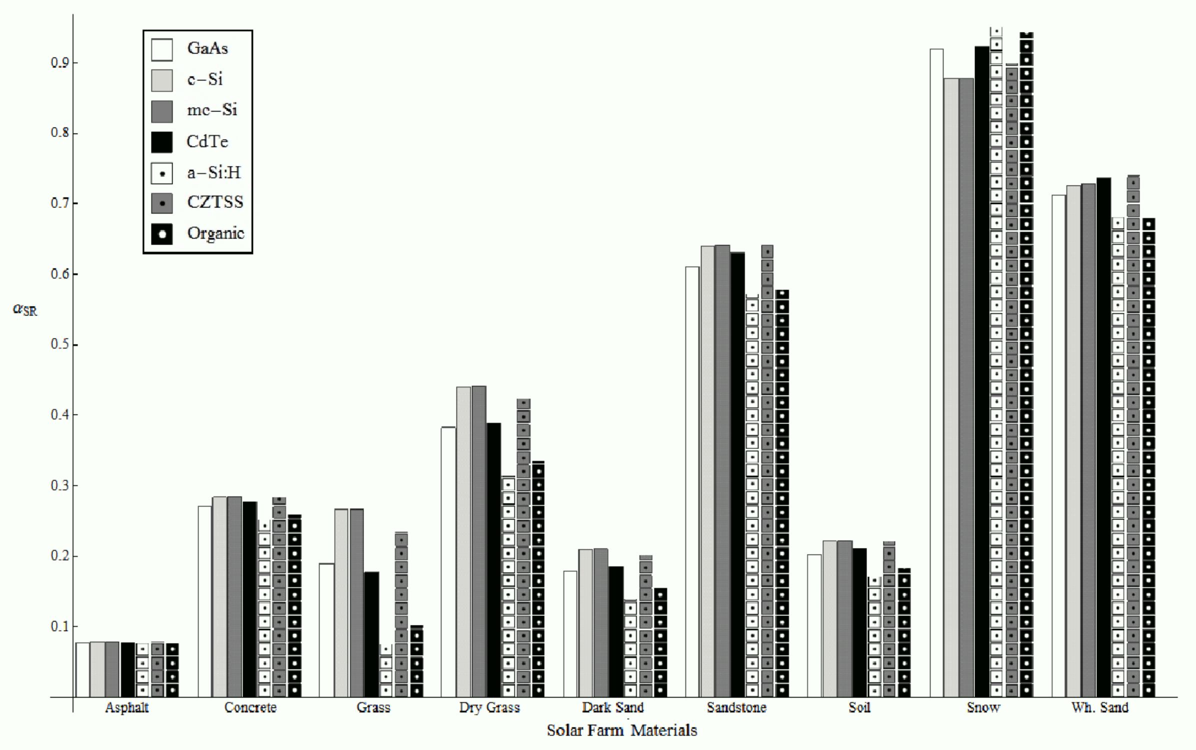

Figure 3.23: The effective albedo of common solar PV farm materials for different PV technologies [12].

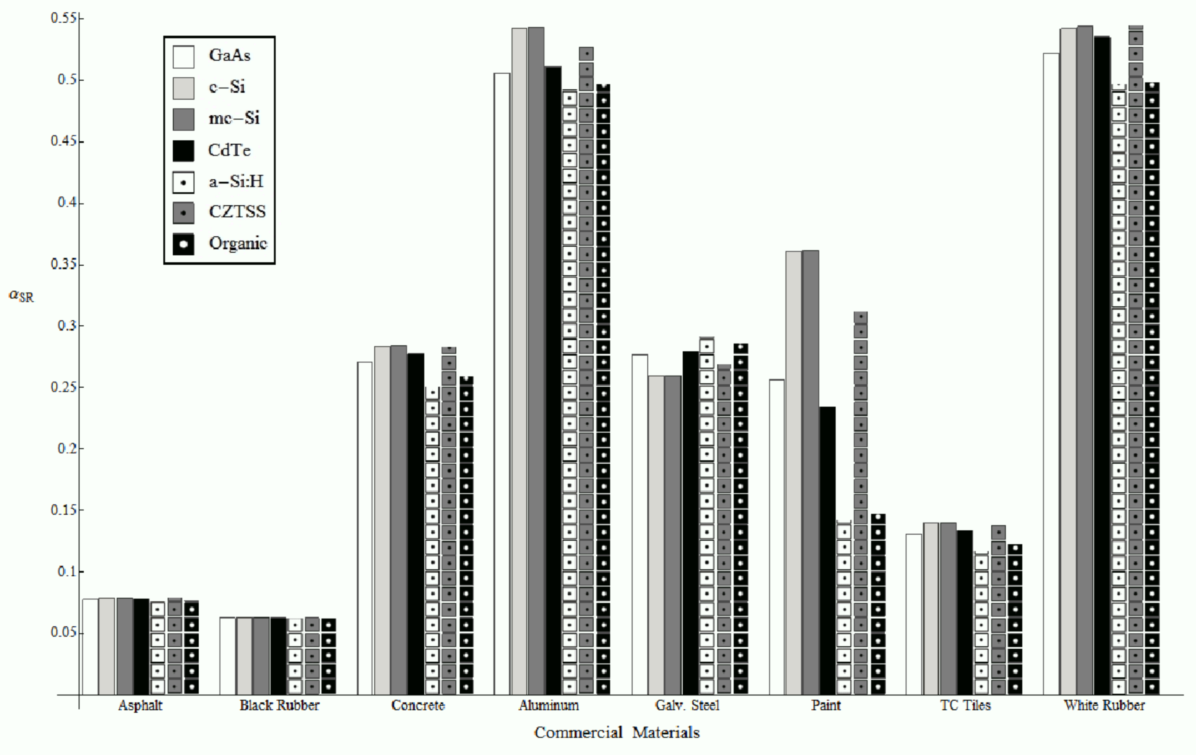

Figure 3.24: The effective albedo of commonly found materials for different PV technologies [12].

3.7. Conclusions

A conclusion that can be drawn from this chapter is that the albedo is a very complex concept.The discrepancy between the different sources should make it clear that there is still too much uncertainty

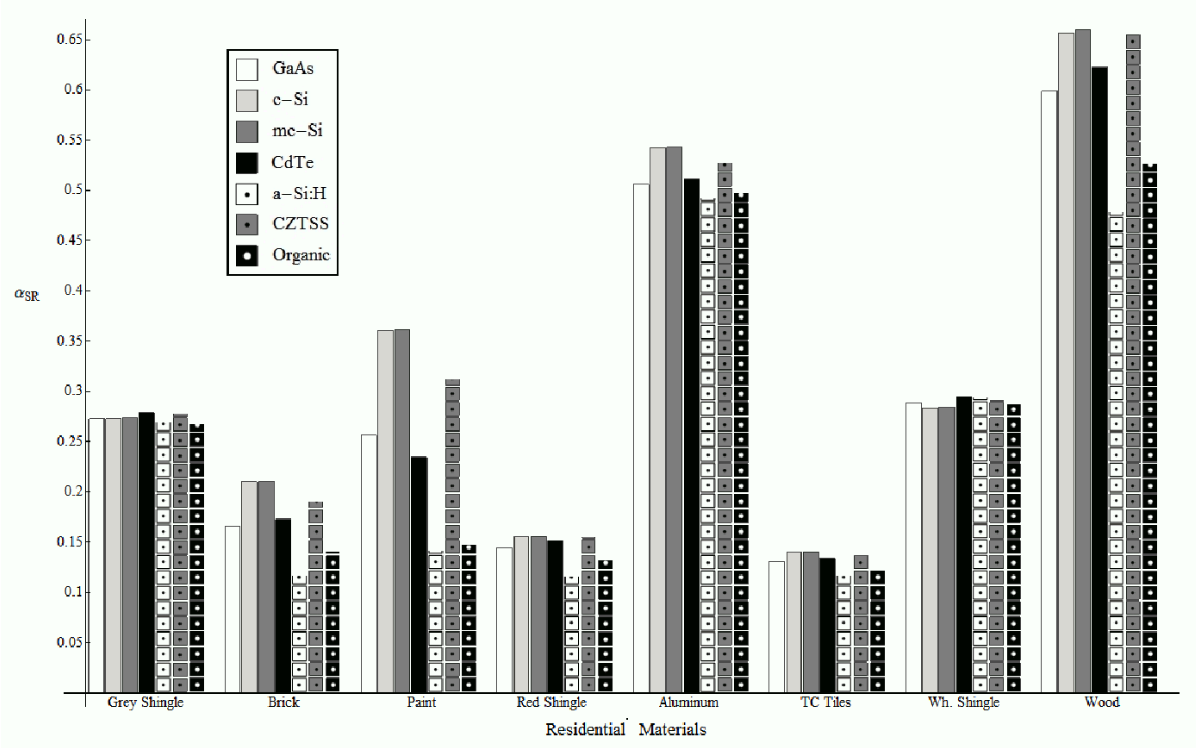

Figure 3.25: The effective albedo of common rooftop materials for different PV technologies [12].

concerning the topic which is albedo, while it proves to be significant in certain situations. Measurements have shown that the albedo seems to change with respect to the irradiance, view factor from the albedometer to the reflecting surface and weather conditions. The albedo that is measured is the location specific albedo and it should not be used for any other location. Changing the location means that the geometry and the materials of the surroundings change. Measuring the albedo above a material and claiming that the measured value is the albedo factor of that material is not true. Even more so, if the albedo has been measured for a location, it will change with respect to time due to a change in the irradiance and weather conditions. The albedo will behave differently during cloudy conditions compared to clear sky conditions. A new concept is therefore introduced, which should address all the factors which change the albedo. The spectral reflectivity of the material along with the spectral irradiance is are expected to be the actual factors which describe the albedo. Research is being done to create a model which is able to give the actual albedo using Aster data [8].

The spectral reflectance becomes even more important when considering the different band gaps of PV technologies as the output power can be increased by choosing the right PV technology depending on the materials surrounding the PV modules. According to Russell [35] the output power can be increased by at least 7.5% or reduced by 2.9% when choosing the wrong material.

4

LiDAR data and simulation framework

This relatively short chapter aims to explain the crucial subject for this thesis, which is LiDAR. Also the uses and imporance of LiDAR along with the simulation framework is made clear. Finally the reason why the Unity 3D game engine was chosen as the simulation framework is given.

4.1. LiDAR

For many applications it is important to know what a certain location looks like. By looking at for example: satellite images, a great deal of important information on a location can be seen. However, for some applications it is not enough to simply know that there are buildings or trees in an area, but it is also necessary to know the dimensions of these objects including the height. To accurately predict the yearly irradiance on a PV module it is also important to know the height of buildings, trees and other objects since these might block the sun.
LiDAR comes from light detection and ranging. According to ESRI [36], LiDAR is ”an optical remote-sensing technique that uses laser light to densely sample the surface of the earth, producing highly accurate x,y,z measurements”. LiDAR is a cost effective alternative for techniques such as photogrammetry which is a technique in which photos are used to determine the distance between two points. When doing this multiple times for different points, the location of the points of which an object consists of can be mapped accurately in x,y,z coordinates. However, this technique requires high quality photos of a location from multiple locations.

4.2. How does LiDAR work

LiDAR works by sending out and receiving laser pulses of which the difference in time of sending the ray out and receiving it will be measured. Now by using the speed of light, the distance of the plane from which the laser is sent out to the point of impact is calculated. The other known parameters are the coordinates of the plane, the height of the plane and the angle in which the laser beams are sent out. By doing this for every 0.5m, the point cloud of the area under the plane will be made.

4.3. What format does LiDAR use

The acquired LiDAR data can be used in several formats including the TIFF or GeoTIFF format and the LAS or LAZ (Compressed LAS file) format. When processed, all of these formats can be used. The TIFF format stands for ”tagged image file format” meaning that a TIFF file is in essence an image. From AHN [37], the GeoTIFF file format can be downloaded which will provide a 2 dimensional image with grey scale pixels. These pixels hold the height of a specific location which is determined by the x and y position on the image. The white colors can be set to the minimum height, while the black colors are set to the maximum height or the other way around. These are called ”height maps”.

4.4. Compatibility with Unity3D

For the simulation, the Unity3D game engine is used and therefore it should be compatible with the height map. In order to achieve compatibility, the TIFF file is first processed using geographic information system (GIS) software. The following steps are taken in order to turn the TIFF file to a format which can be used in the Unity3D game engine:
- Importing the TIFF file into the GIS software,
- Cut the image to a smaller size to reduce the file size and in order to make the program run faster (optional),
- Change the minimum and maximum values of the grey scale to the minimum and maximum values which are present in the area which is represented by the image,
- Remove the noise in the image by changing these values to the minimum height in order to prevent interference of these points with the simulation. Another option is to interpolate the unknown pixels with the surrounding pixels,
- Export the image in a format which is compatible with simulation software. In the case of Unity3D a portable network graphics (PNG) file format is usable,
- Import the processed PNG file into the simulation software,

An example of the final processed PNG file height map can be seen in figure 4.1.

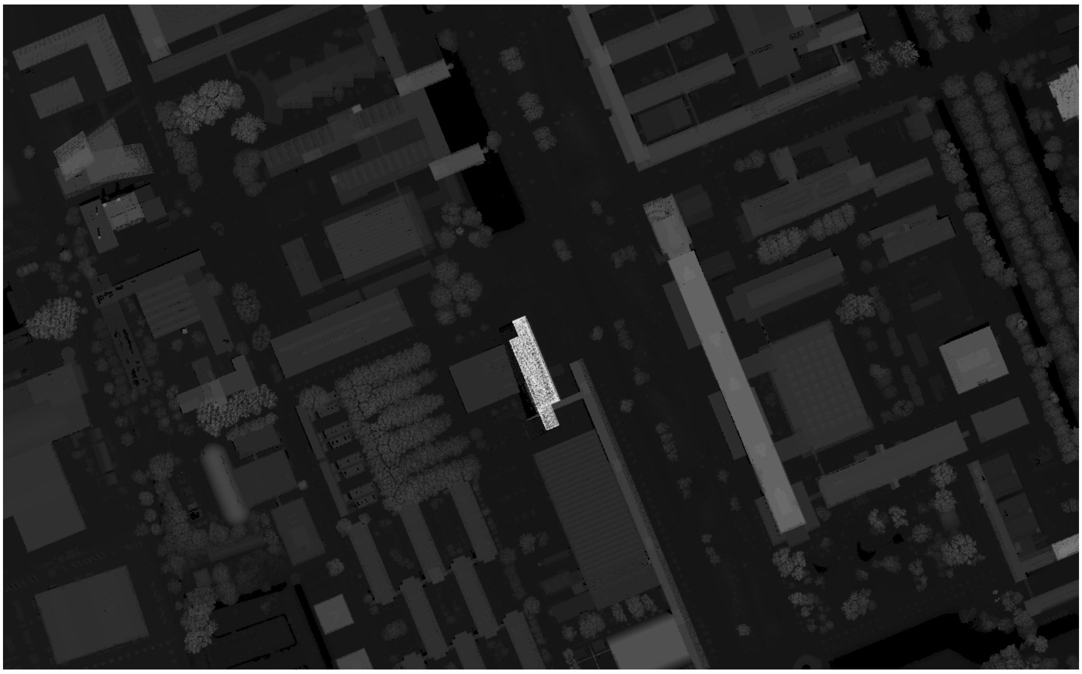

Figure 4.1: Heightmap of the TU Delft campus in a PNG file format for a 780 meter by 482 meter area.

This figure has a resolution of 0.5 meters, which means that for every 0.5 meters there is a height value or there are 9 height values in $1m^2$. Figure 4.1 has 1560 by 964 pixels. Since each pixel means half a meter, then the total length and width of this area is $\frac{964}{2} = 482\ meters$ by $\frac{1560}{2} = 780\ meters$, respectively. The length is in a north-south orientation, while the width is in a east-west orientation.

4.5. LiDAR terrain in Unity3D

In Unity3D, a height map can be applied onto a terrain, which creates a terrain object of the height map. This terrain object is a plane of which the x and y positions have been lowered or raised in accordance with the height map. The height map can only state that a certain position has the minimum height, maximum height or a height in between the two. The values for the minimum and the maximum height must be assigned in Unity3D. The heights in between the minimum and the maximum will be interpolated according to its gray scale value. The resulting terrain when using the gray scale image of figure 4.1 is shown in figure 4.2.

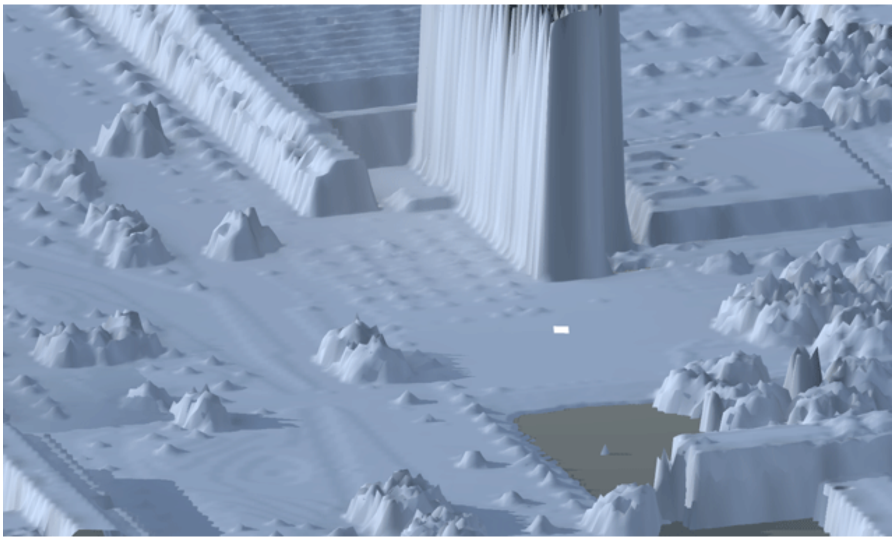

Figure 4.2: Unity3D game engine terrain of the EWI faculty building in the TU Delft campus

The resulting terrain is able to block ray casts which is important for the simulation. This will be explained in more detail in chapter 5 concerning the sky view factor and section 7.3 concerning the shading factor. Figure 4.3 shows a screen shot taken from Google Maps [13].

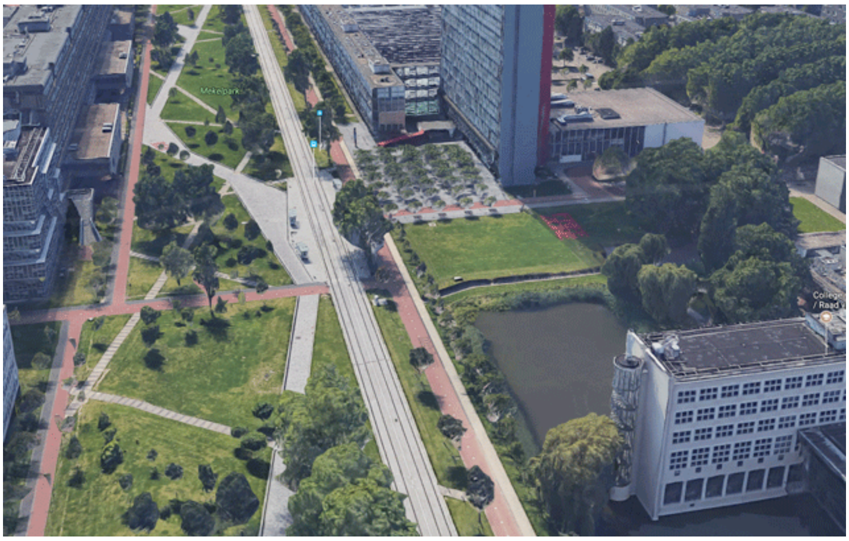

Figure 4.3: Google Maps terrain of the EWI faculty building in the TU Delft campus [13]

Great similarities can be seen between figure 4.2 and 4.3 since they have approximately the same point of views for the areas. However, there are still distinguishable differences. One of the differences is the texture which Google Maps has which lacks in the Unity3D terrain. This is however not a significant difference, because the texture is not required for the simulation. Another difference is the lack of multiple height points on a single (x,y) coordinate in the Unity3D terrain for objects like trees. This makes all objects seem as if they are extruded from the ground. However, this does not pose a problem for most of the PV systems since PV panels are not placed directly underneath a tree. In case that the terrain does intervene with a PV system, the terrain can be modified accordingly.

4.5.1. Modification of terrain in Unity3D

LiDAR data is not always up to date causing the simulation to be different from the real life situation. A large advantage of using the Unity3D game engine is that it allows the user to make detailed changes to the terrain. If for example a high building has been built on a location recently, it will not appear in the LiDAR data making it seem as if there is no building on the location. This might influence the yearly irradiation drastically since the high building might block a great deal of the sun. An object resembling the building can then be put in the simulation with custom dimensions which increases the accuracy of the simulation by making it more realistic. As an example, figures 4.4 and 4.5 show the unaltered and the altered simulation environment.

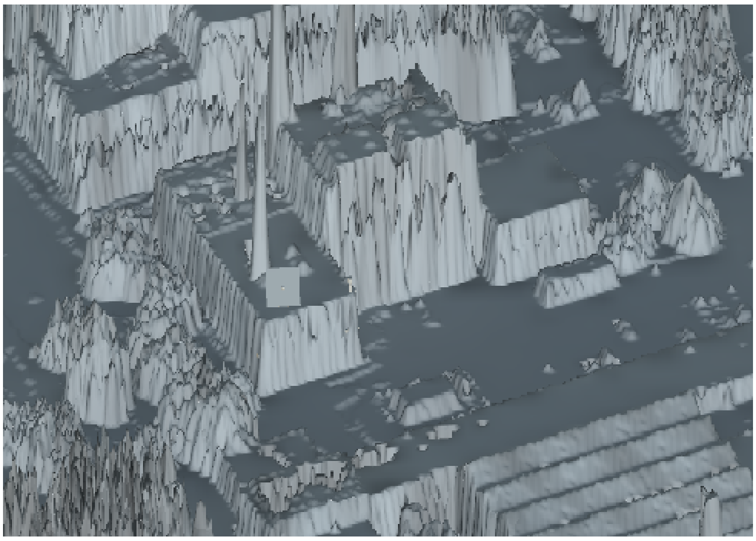

Figure 4.4: The unaltered simulation environment.

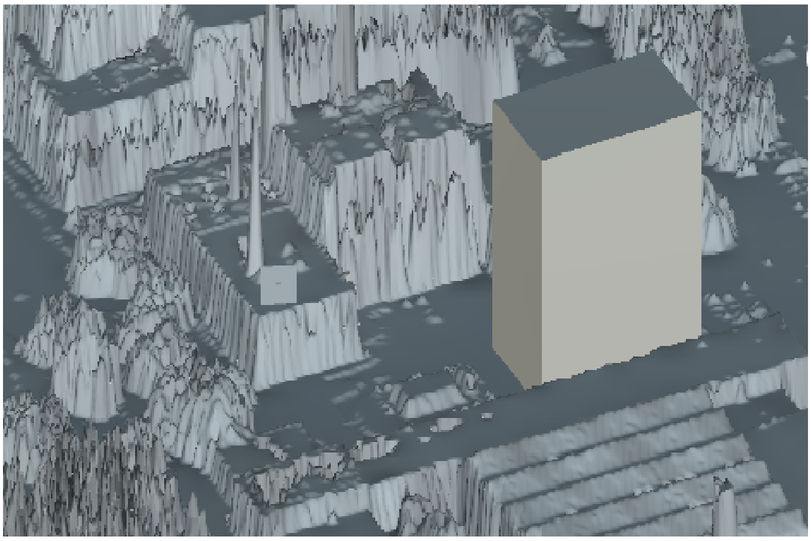

Figure 4.5: The altered simulation environment, where a block has been added, which represents a building.

4.6. Conclusions

LiDAR data is of significant importance for this project, because it saves an incredible amount of time, since the environment does not have to be produced manually. LiDAR also allows the user to see the actual environment in 3D, which potentially allows the consumer to see the PV system in real time on their roofs. Using the Unity 3D game engine allows for rapid changes to the environment. This way, the environment for which the simulation has to be done will be as it should be. Even more so, Unity 3D allows the user to change the environment such that it resembles the situation of the future. As an example, if a large building is planned to be built close to a PV system, by adding the planned building in the simulation, the impact of such a change can be made visible before it is even built.

5

Sky view factor

The sky view factor is the fraction of the visible area of an observer which is not obstructed by objects. In other words, it is a value between zero and unity which shows the amount of sky with respect to the total visible area of a point in space. Since the lower hemisphere of the visible area always consists of ground, the sky view factor will only take into account upper hemisphere. If the lower hemisphere would be taken into account, the sky view factor would be a value between 0 and 0.5. There are several methods which are used to obtain the sky view factor (or SVF as an abbreviation). This chapter will handle several of these methods and finally present a method which allows an accurate way to determine the SVF without the need to do in-field measurements in the location.

5.1. Geometric definition of the sky view factor

A part of the field of view of a PV module will always be blocked by the PV module itself, unless the PV module is placed flat on the ground. Therefore the SVF will at least be determined by the angle θ in which the PV module is placed with respect to the ground. An illustration of the SVF can be seen in figure 5.1.

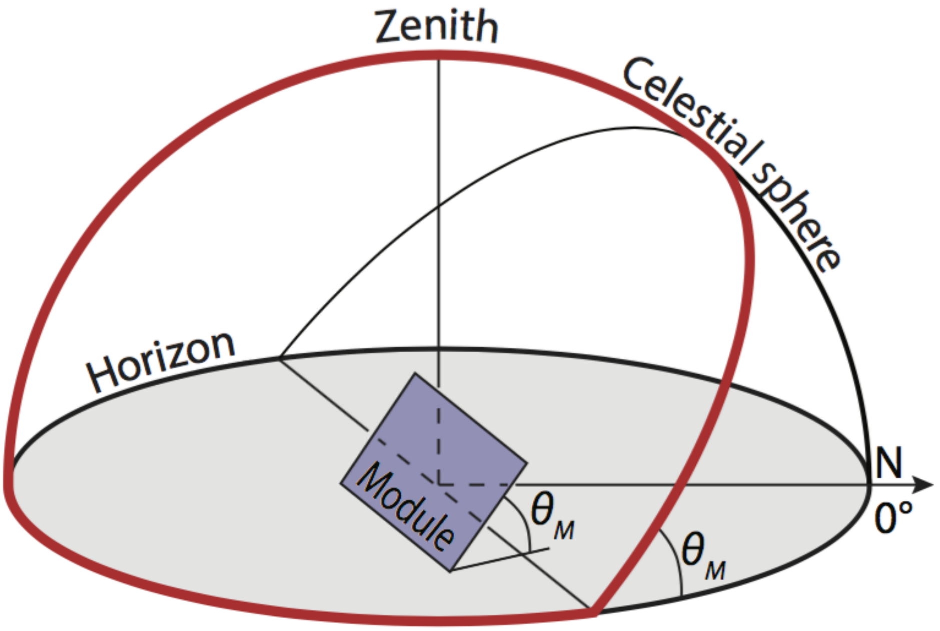

Figure 5.1: Illustrating the definition of the sky view factor , which is the fraction of the celestial hemisphere enclosed by the thick red line [4].

A mathematical formula can be used to calculate this SVF. This mathematical formula only requires the angle θ of the PV module:

$$SVF = \frac{1 + \cos\theta_M}{2} \tag{5.1}$$

This equation gives the plot of figure 5.2.

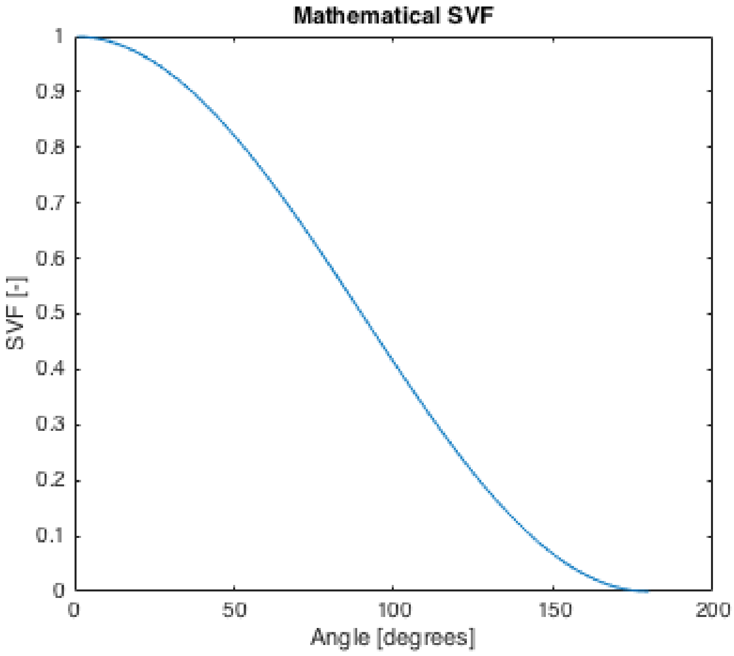

Figure 5.2: The plot of equation 5.1 for all angles of θ

.

As can be seen from the plot, when the angle of the PV module θ_M is minimum, the SVF is maximum and when θ_M is maximum, SVF is minimum. Therefore, in order to maximize the diffuse component, the angle of the PV module should be kept low. This is explained in detail in chapter 2.

Equation 5.1 has a large drawback since it is only accurate for large open areas in which the PV module will see no obstructions from any objects like buildings or trees. Also, when multiple rows of PV modules are placed in front of each other, this equation is no longer applicable.

5.2. Sky view factor using the Meteonorm software

Another way of determining the sky view factor is by using a fish eye camera [38]. A fish eye camera tool which is widely used is horicatcher of meteonorm which can be seen in figure 5.3 [14].

When a picture is taken using this tool, the entire upper hemisphere is recorded on a single picture. After processing this picture using the horicatcher tool of Meteonorm a so called SVF grid is made from which the SVF can be determined very accurately. Figure 5.4 shows an example of a SVF grid.

The sky view factor that has been determined for the SVF grid of figure 5.4 is 0.8896. The most important drawback of this tool is the need to go to the location of which the SVF is required. Therefore it is very time consuming to determine the SVF using this method. Also, when changes are required, this tool requires new pictures to be taken. However, since it is a very accurate tool, it is still in use very much.

5.3. Sky view factor using Chronolux

Another way of determining the SVF is by using the LSS Chronolux tool of Sketchup. This tool allows the user to determine the SVF with less accuracy compared to the horicatcher tool. Also it requires the user to either create the 3 dimensional environment using Sketchup or import the different objects

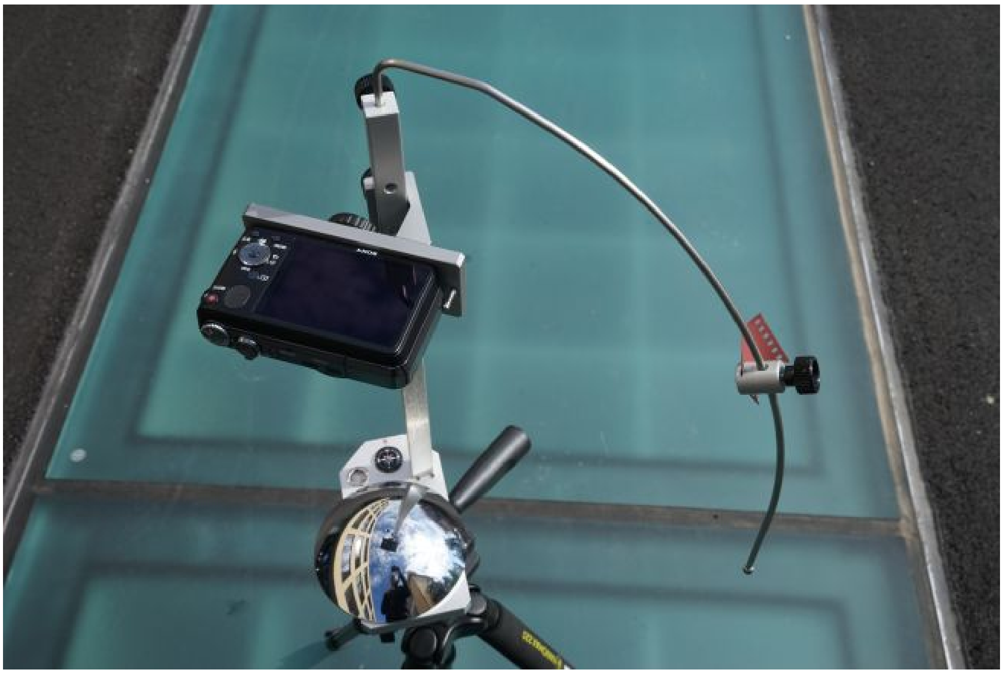

Figure 5.3: The horicatcher tool of meteonorm with a digital camera and a horizon mirror [14].

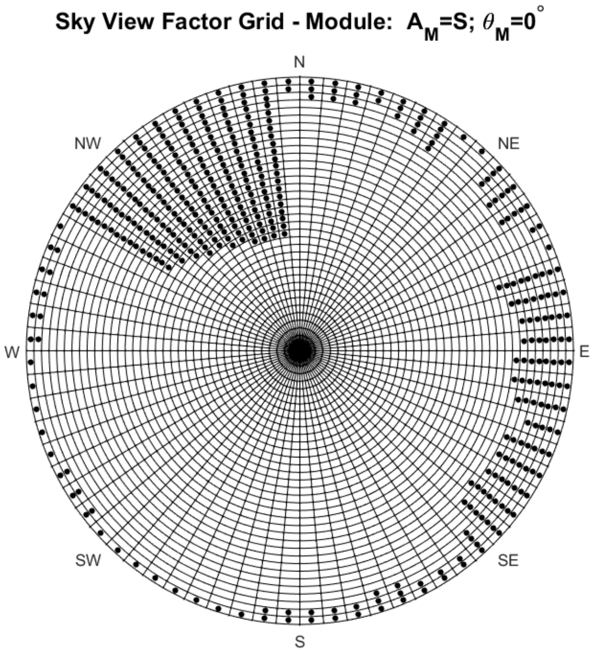

Figure 5.4: Sky view factor grid made by the horicatcher tool, which gives an SVF of 0.8896.

surrounding the area in which the SVF is required to be determined. This, however is not available for all locations.

5.4. Sky view factor using Unity3D with LiDAR data

Finally, the SVF can also be determined using the Unity3D engine together with LiDAR data. The terrain that is obtained from LiDAR data is able to intercept ray casts. This allows for a very easy, but effective way to determine the SVF. This method will be called the ray casting method. The ray casting method

to determine the SVF requires for a great amount of rays to be cast in all directions of an hemisphere, evenly distributed.
There are several methods to achieve an even distribution on a sphere. The objective of these methods is to achieve the most densely packed distribution of points on a sphere. The so called Rusin's disco ball method is able to pack the points most densely on a sphere [39]. However, it requires very specific number of points to be packed on a sphere. Another method is proposed by Saff and Kuijlaars [40]. Their method allows for any positive integer number to be used for the amount of points to be packed on a sphere, but it can pack less points on a sphere than Rusin's disco ball method. The method that is used in the simulation will be the Fibonacci lattice method [41], because it is able to pack the points more densely on a sphere compared to Saff and Kuijlaars, but it is still able to allow any positive integer number of points to be put on a sphere as opposed to Rusin's disco ball method. Boucher [42] has made a python script which is able to take any positive integer number x as an input and return an array of x points on a sphere distributed evenly over the sphere. Based on Boucher's code, a C# script was made which was then used in the simulation.
The Fibonacci lattice method gives an x number of points on a sphere which are evenly distributed over the sphere. In order to determine the SVF from this, an x number of rays are cast in all directions of these x number of points from the center of the sphere. These rays are cast in the same direction as the normal's of points x on the sphere. The further these rays reach, the larger the distance will be between the end points of these rays. This is illustrated in figure 5.5.

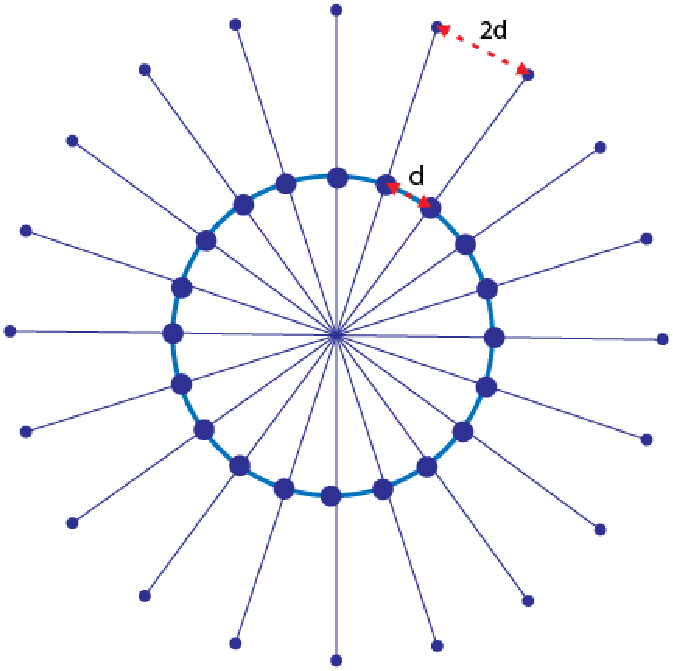

Figure 5.5: An illustration showing how the distance between the end points of the rays become larger when the distance of the end points to the center of the sphere increases.

In order to achieve a high accuracy for the SVF, a thorough saturation of rays in the simulation is necessary. This is done by increasing the number of rays that are cast. Figure 5.6 shows how the rays are cast from the PV module in all directions.

In the case of figure 5.6 a total of 50000 rays were cast. The blue lines are the directions of the ray casts and the red dots are where a ray hit a terrain. The rays that did not hit any terrain are not shown, but they are simulated nonetheless. The SVF is simply the division between the number of non-hits n by the total number of rays cast t with Lamberts cosine law applied to each ray. Lambert's cosine law implies that the rays that are cast with an angle closer to the normal of the surface from which it is cast will have more weight. This is explained in more detail in chapter 6. Without applying Lambert's law, we get equation 5.2 for the SVF.

$$SVF = \frac{n}{t} \tag{5.2}$$

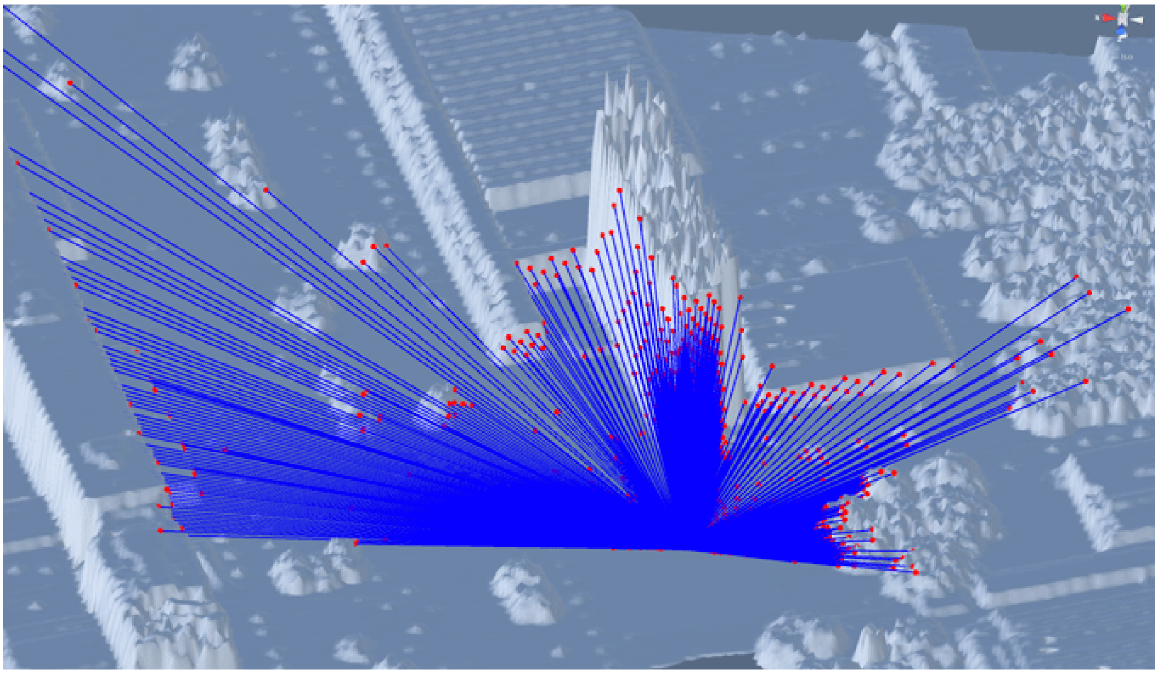

Figure 5.6: SVF prediction by ray casting in the simulation using 50000 rays.

Non-hits are rays which were not intercepted by any terrain or other objects. Therefore the hits h are the total number of rays cast t minus the non-hits n.

$$h = t - n \tag{5.3}$$

From equations 5.2 and 5.3, equation 5.4 follows.

$$SVF = \frac{t-h}{t} \tag{5.4}$$

After applying lamberts cosine law we obtain equation 5.5 which also takes into account the weight of each ray as a function of its angle with respect to the normal of the surface from which it is cast.

$$SVF = \frac{n}{t} = \frac{\sum_{i=1}^{i=x} n_i \cos\theta_i}{\sum_{j=1}^{j=y} t_j \cos\theta_j}, \tag{5.5}$$

where x is the counted number of non hits and y is the counted number of each ray. n_i is a ray that did not hit, while t_j is one of the total number of rays and $cos\theta_i$ and $cos\theta_j$ are their angles with respect to the normal of the surface from which the rays are cast respectively.
Therefore if either the number of non-hits are known together with the total number of rays cast along with the weight of each ray, the SVF can be calculated.
The SVF calculated using equation 5.1 and the SVF using the simulation with equation 5.5 have shown near identical results when the same geometrical situation is applied in the simulation, meaning that there are no obstacles in the environment and the same tilt angles are used. The SVF obtained from equation 5.1 is 0.8535534,while the SVF obtained from the simulation for the same situation is 0.8534572 using 10000 rays. The difference in percentage is a mere 0.0112712%. The difference in percentage when using just 100 rays is 1.2263% which is still relatively accurate.

5.5. Accuracy and simulation time of SVF with respect to amount of rays

Ray casting requires a lot of simulation time. Naturally, the simulation time increases for an increasing amount of total rays. The simulation time for 1 million rays can be approximately 300 seconds depending on the SVF of the location. However, this time is very low compared to the time which is needed to use the Horicatcher method or the time that is required to build the environment in Google Sketchup. The SVF which is found using 1 million rays is assumed to be the exact SVF for the simulation since the inaccuracies of the LiDAR data are more significant than the inaccuracy of the amount of rays used to determine the SVF. Figure 5.7 shows the SVF according to the simulation for an increasing amount of rays used, with a maximum of 1 million total rays.

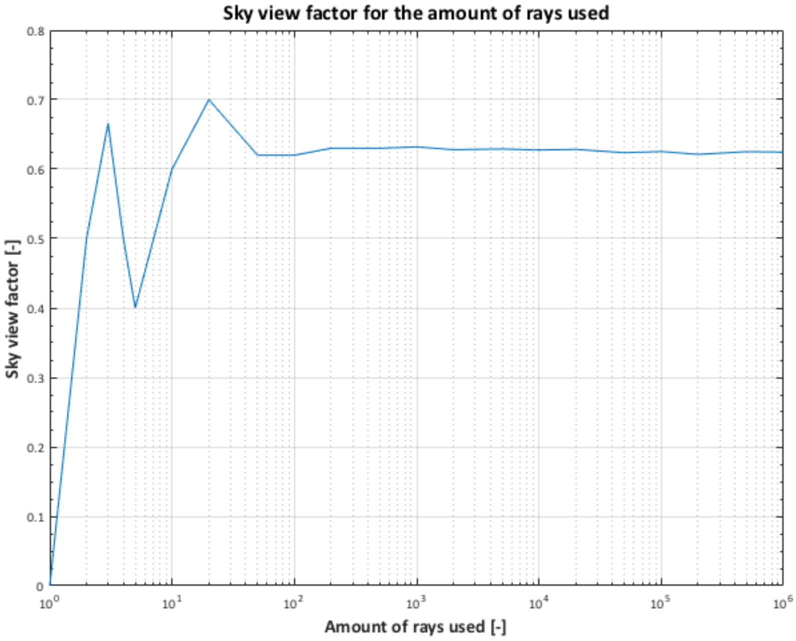

Figure 5.7: The SVF plot according to the simulation for a different number of total rays used.

The SVF seems to be stabilizing after a total of 1000 rays, however to know the exact accuracy for the different amount of rays that are used, the difference in percentage has been calculated. Figure 5.7 shows the difference in % for an increasing amount of total rays used (approaching 1 million rays).

According to this figure, the difference in percentage for 1000 rays is 0.35% as compared to 1 million rays. The difference in percentage becomes increasingly smaller for an increasing amount of rays. The smallest difference of 0.0028% is found for 200000 rays. Such accuracies seem to be satisfactory for the purpose of the simulation. In order to choose the perfect amount of rays used in the simulation, the simulation time is also checked and compared. As was mentioned before, the simulation time is approximately 300 seconds when 1 million rays are cast in total. The simulation times have been plotted for a number of total rays cast and they can be seen in figure 5.9.

Figure 5.9 shows a linear increase in the simulation time for an increase of the amount of rays used to determine the SVF. When increasing the amount of rays with an order of magnitude, the simulation time increases drastically. Therefore, it is important to keep the amount of rays used as low as possible. Since the 0.35% accuracy of the SVF seems to be sufficient and the simulation time is very low with only 0.36 seconds of simulation time, the amount of rays that will be used are kept to 1000 when determining the SVF.

5.6. Conclusions

The sky view factor can be easily calculated for a location without the need to do field work, which saves very much time. The ray casting model has shown very accurate results compared to the geometrical equation of the sky view factor. The simulation time in order to achieve a high accuracy sky view factor does not have to be very high, since a relatively small amount of rays are sufficient to have an accuracy which is no longer limited by the number of rays used, but with the resolution of the LiDAR data as an example. In 0.36 seconds of simulation time an accuracy of 0.35% can be achieved, while using only 1000 rays with respect to the sky view factor found using 1000000 rays. Increasing the amount of rays boosts up the accuracy even further, but the simulation time increases with it.

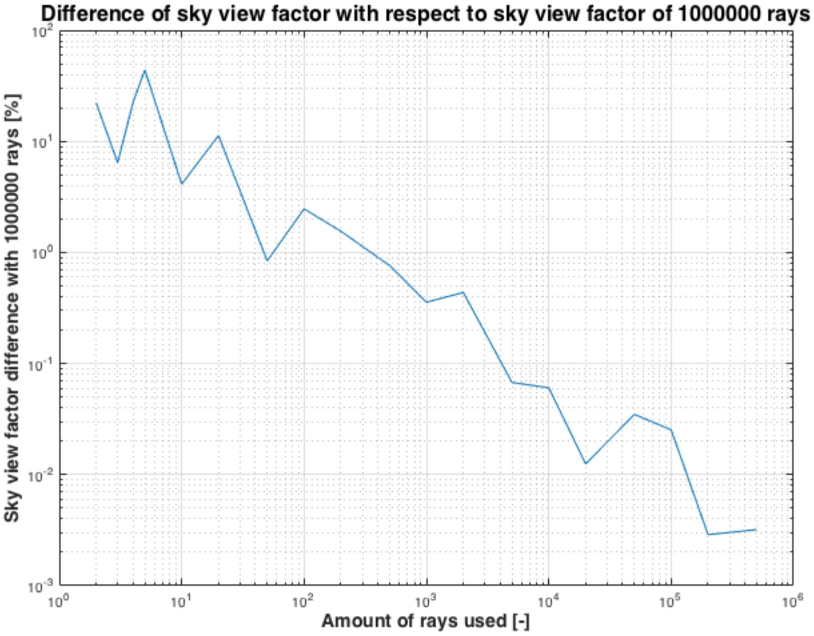

Figure 5.8: The difference of the SVF in % for a different number of total rays used.

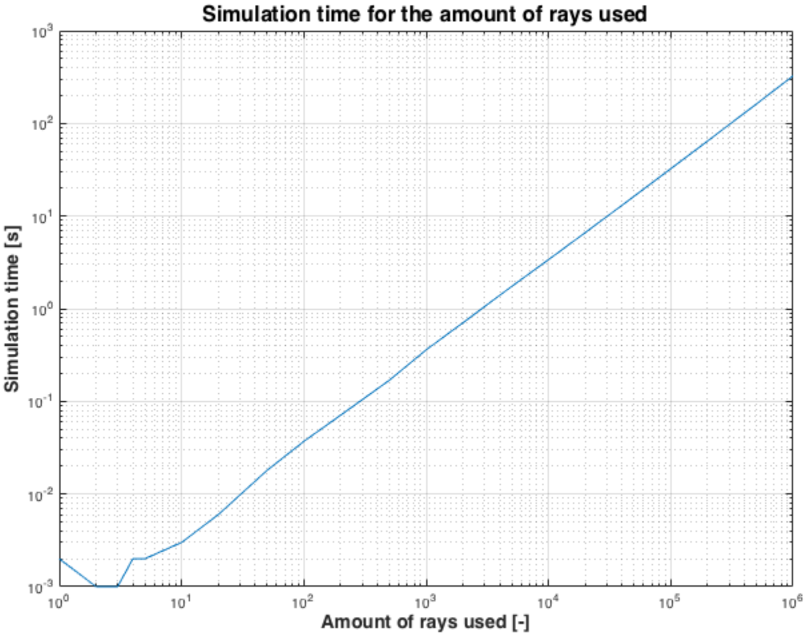

Figure 5.9: The simulation time for the amount of rays used.

6

View factor

An important difference between the model used in this thesis and the existing models is the use of the view factor. This chapter aims to explain in great detail what the view factor is, the way that it is estimated using the ray casting method and its validation using exact solutions. Also, the reciprocity rule is explained which allows the interchangeability of the view factor.

6.1. View factor

According to Mills [43], the definition of the view factor F_{12} is the fraction of radiation leaving area A_1 that is intercepted by area A_2. In the same way, F_{21} is the fraction of radiation leaving A_2 that is intercepted by area A_1. The shape factor is a geometrical concept that is dependant only on the size, shape and orientation of the surfaces. In the field of heat and mass transfer and optics, the view factor is used to determine the fraction of the radiation that leaves a surface which is intercepted by another surface. Therefore, to calculate the power that is transmitted between two surfaces, only the view factor and the net power of the source is required.

6.2. Mathematical problem

The view factor of a great number of two- and three- dimensional configurations have been defined and can be easily calculated using the corresponding algebraic formulas. These formulas are sufficient for many applications. However, to be able to calculate the view factor for every situation, a more complex equation has to be solved.

According to Mills [43], the radiation leaving a differential area dA_1 that is intercepted by area A_2 can be seen in equation 6.1.

$$F_{d1-2} = \frac{1}{\pi} \int\limits_{A_2} \frac{\cos\theta_1 \cos\theta_2}{L^2} dA_2, \tag{6.1}$$

where, F_{d1-2} is the view factor, A_2 is the area of the surface that intercepts the radiation from differential area dA_1, θ_1 is the angle between the normal of area A_1 and the line between area A_1 and A_2, θ_2 is the angle between the normal of A_2 and the line between area A_2 and A_1 and finally L is the length between dA_1 and A_2.

To calculate the view factor for the finite area A_1, the view factor of equation 6.1 is integrated over area A_1. Hence, the view factor F_{1-2} will become the radiation leaving a finite area A_1 that is intercepted by a finite area A_2 as can be seen in equation 6.2.

$$F_{1-2} = \frac{1}{A_1} \int_{A_1} \int_{A_2} \frac{\cos\theta_1 \cos\theta_2}{\pi L^2} dA_2 dA_1 \tag{6.2}$$

Now the area of the radiating surface A_1 is added to the equation making it a double integral equation. The double integral makes this a very challenging mathematical problem [43].

6.3. Reciprocity rule for view factors

From the symmetry of equation 6.2, it can be written that the view factor of an area A_1 that intercepts the radiation from a finite area A_2 is as is given in equation 6.3.

$$F_{2-1} = \frac{1}{A_2} \int_{A_2} \int_{A_1} \frac{\cos\theta_1 \ \cos\theta_2}{\pi L^2} dA_1 dA_2 \tag{6.3}$$

From equations 6.2 and 6.3, equation 6.4 follows.

$$A_1 F_{12} = A_2 F_{21} \tag{6.4}$$

This equation is the so called reciprocity rule which implies that the view factor F_{1-2} is related to view factor F_{2-1} by the ratio of surface A_1 and A_2.

6.4. Numerical method for determining the view factor using the Riemann method

Another way of determining the view factor between two surfaces is by approaching the problem numerically. Dobrowolski de Carvalho [44] uses an approximation of the double integral described in equation 6.2. The method that is used to approximate the double integral is with the use of the Riemann method [44]. The areas A_1 and A_2 are divided into a great number of small triangles, creating a mesh of the surface. By using the Riemann method [44], equation 6.2 can be re-written as is done in equation 6.5.

$$F_{i-j} = \frac{1}{A_i} \sum_{i=1}^{n} \sum_{j=1}^{m} \frac{\cos\theta_i \cos\theta_j}{\pi L^2} dA_j dA_i \tag{6.5}$$

The cosines i and j are given by equations 6.6 and 6.7.

$$\cos\theta_i = \frac{l_i(x_j - x_i) + m_i(y_j - y_i) + n_i(z_j - z_i)}{r} \tag{6.6}$$

$$\cos\theta_j = \frac{l_j(x_i - x_j) + m_j(y_i - y_j) + n_j(z_i - z_j)}{r} \tag{6.7}$$

According to Dobrowolski de Carvalho Augusto [44], using this method, the view factor can be approximated with a 0.06% error. To obtain such results, a great number of triangles were used. The numbers ranged from 3000 to 12400.

6.5. Determining the view factor using the Monte Carlo method

The Monte Carlo method is a widely used method to approximate complex systems. It is also widely used to check the validity of solved solutions. "Monte Carlo uses random sampling and statistical modelling to estimate mathematical functions and mimic the operations of complex systems." [45]. The Monte Carlo method can estimate the view factor with great accuracy, however the simulation time is the largest drawback of this method. In order to achieve high accuracies the simulation time can be up to 170360 seconds, which is more than 47 hours. In order to achieve a fully automated PV system method, such simulation times are too large. Using less samples reduces the simulation time, but the uncertainty increases drastically [45]. Therefore, the Monte Carlo method is not viable to use in this specific application.

6.6. Determining the view factor using ray casting

In the introduction of chapter 6, the definition of the view factor according to Mills [43] was given as "the fraction of radiation leaving area A_1 that is intercepted by area A_2". The term radiation which is used in this definition also includes light which is a form of radiation. Therefore, the view factor can also be approximated using ray casting since radiation is the transfer of energy through space in the form of particles or waves. In order to approximate the F_{i-j}, area A_i should emit an x amount of rays in every direction from A_1. Now the y amount of rays that intercepted by area A_j must be counted. The resulting view factor is calculated as in equation 6.8.

$$F_{i-j} = \frac{y}{x} \tag{6.8}$$

The rays can either be cast randomly in all directions in the 3D space or they can be cast in the direction of an x amount of points on a sphere which are evenly distributed over the sphere. Since using the method which distributes the rays randomly gives an uncertain and a different distribution every time, it is therefore evidently better to use the method which evenly distributes the rays. Equation 6.8 gives the view factor from a sphere with area A_i to an area A_j. It is important to note that here the radiating surface is a sphere which radiates light in all directions evenly distributed.

6.7. Comparing the results of ray casting with exact solutions

To prove that the method which uses ray casting to obtain the view factor works, the results have to be in line with the exact solutions for view factors. The exact solution for the view factor for a differential sphere to a sphere with radius r can be calculated since the geometry is relatively simple. According to Chung et al. [46], the view factor from a spherical point source, or differential sphere to a sphere can be found from exact solution of equation 6.9.

$$F_{d1-2} = \frac{1}{2}(1 - \sqrt{1 - R^2}), \tag{6.9}$$

where R is defined as $R = \frac{r}{h}$ and h is the distance from sphere 1 to the center of sphere 2. As an example, the distance h and radius r have been defined to be 200 and 50 respectively for the equation as well as the simulation. The equation can be solved as is done in equation 6.10.

$$F_{d1-2} = \frac{1}{2}(1 - \sqrt{1 - R^2}) = \frac{1}{2}(1 - \sqrt{1 - (\frac{r}{h})^2}) = \frac{1}{2}(1 - \sqrt{1 - (\frac{50}{200})^2}) = 0.015877 \tag{6.10}$$

When casting 200000 rays from sphere 1 in the simulation, 3175 rays are intercepted by sphere 2. This situation as used in the simulation has been illustrated in figure 6.1.

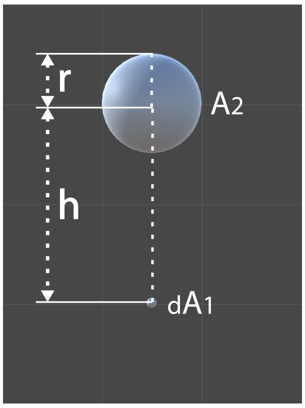

Figure 6.1: The view factor for a differential sphere dA_1 to sphere A_2 where h is the distance between differential sphere 1 and the center of sphere 2 which has a radius r.

Using equation 6.8, the view factor for the simulation can be calculated as well. This is a simple division which is also done in the simulation as is done by equation 6.11.

$$F_{d1-2} = \frac{3175}{200000} = 0.015875 \tag{6.11}$$

There is a 0.013% difference between the simulation and the exact solution. Therefore, the simulation does indeed seem to deliver the same results as the exact solution.

A PV module however, is not a sphere, but a plane object and therefore the simulation has to be corrected for it. The exact solution for the view factor from a differential planar surface to a sphere with radius r can be found from equation 6.12.

$$F_{d1-2} = R^2, \tag{6.12}$$

where R is again defined as $R = \frac{r}{h}$ and h is the distance from surface 1 to the center of sphere 2. Using the same parameters for h and r, the view factor is again calculated as in equation 6.13.

$$F_{d1-2} = R^2 = \frac{r}{h} = (\frac{50}{200})^2 = 0.0625 \tag{6.13}$$

For the simulation, the radiating object also has to behave like a planar surface and therefore the rays have to be corrected for it. According to Juds [47], diffuse light is scattered according to Lambert's law which means that the light which is scattered follows a cosine relationship. This means that the intensity is reduced as the angle between the light and the normal of a surface increases. This is illustrated in figure 6.2.

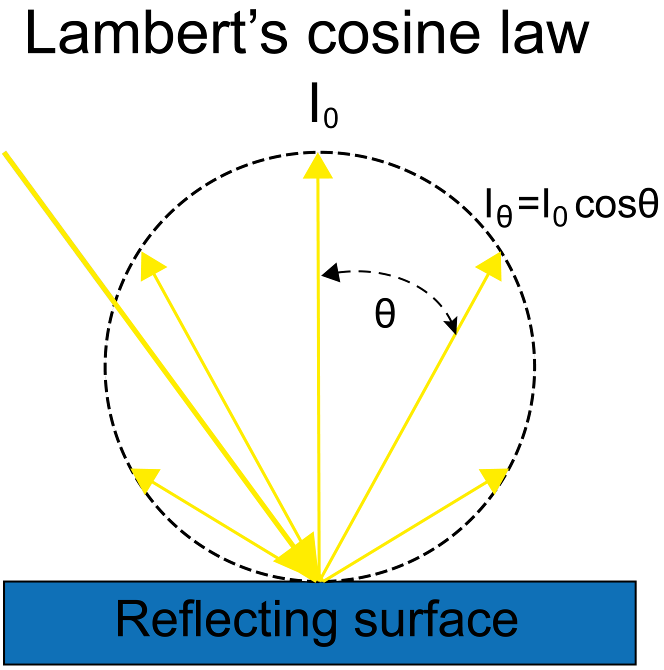

Figure 6.2: Lambert's law showing how the reflected intensity decreases as the angle of the reflected beams increase with respect to the normal of the reflecting surface.

The lambertian intensity of the light is defined in equation 6.14.

$$I_\theta = I_0 \cos\theta, \tag{6.14}$$

where I_0 is the intensity of the light which has a 0 degrees angle with respect to the normal of the surface. This is the maximum intensity for the reflected light. To correct for Lambert's law in the simulation, the rays that are intercepted by A_2 will be counted accordingly. This means that each ray hitting surface A_2 will have a factor $cos\theta$. This is defined in equation 6.15.

$$y = \sum_{i=1}^{i=n} y_i \cos\theta_i, \tag{6.15}$$

where n is the total number of ray hits on A_2. y_i is a ray which has hit area A_2 with an angle θ_i to the normal of A_1. Finally y is the total number of hits on A_2 which has been corrected according to Lambert's law.

Not only the rays that hit A_2, but also the remaining rays are emitted evenly distributed in all directions of a sphere and therefore they have to be corrected according to Lambert's law as well. First of all, the directions which the rays are cast to are limited to the hemisphere facing the normal of the surface since the light which is reflected has an angle of maximum 90 degrees from the normal of the surface by definition. The corrected total number of rays emitted are defined in equation 6.16.

$$x = \sum_{j=1}^{j=m} x_j \cos\theta_j, \tag{6.16}$$

where m is the total number of rays that are cast which have an angle smaller than 90 degrees to the normal of surface A_1 and x_j is a ray which has an angle $\theta_j$to the normal of surface A_1. The corrected equation for the view factor which is used in the simulation is defined in equation 6.17.

$$F_{di-j} = \frac{y}{x} = \frac{\sum_{i=1}^{i=n} y_i \cos\theta_i}{\sum_{j=1}^{j=m} x_j \cos\theta_j} \tag{6.17}$$

Using the view factor equation which has been corrected for a planar geometry, the view factor from a differential planar surface to a sphere with radius 50 is determined. The distance from the differential planar surface to the center of the sphere is again set to be 200. The corrected total number of rays casts and rays hits are 50000 and 3078 respectively. Using equation 6.17 the view factor 6.18 is determined.

$$F_{d1-2} = \frac{y}{x} = \frac{\sum_{i=1}^{i=n} y_i \cos\theta_i}{\sum_{j=1}^{j=m} x_j \cos\theta_j} = \frac{3078}{50000} = 0.06158 \tag{6.18}$$

The difference in percentage between the simulation and the exact solution as was found from 6.13 is now 1.5%. Therefore, the simulation is also capable to determine the view factor from a planar surface to a sphere object. However, this situation is for when the angle of sphere 2 is 0 degrees with respect to the normal of surface 1. The exact solution for this geometry is also available:

$$F_{d1-2} = \cos\theta\ R^2, \tag{6.19}$$

where θ is the angle between sphere 2 and the normal of surface 1 while the R is defined as $\frac{r}{h}$ and h is the distance between surface 1 and center of sphere 2 and r is the radius of sphere 2. By taking 45 degrees for θ and 150 and 50 for h and r respectively, the resulting view factor is calculated in equation 6.20.

$$F_{d1-2} = \cos\theta R^2 = \cos 45(\frac{r}{h})^2 = \cos 45(\frac{50}{150})^2 = 0.078567 \tag{6.20}$$

When running the simulation for the same parameters, the resulting view factor is found to be 0.0776. The difference in percentage between the exact solution for the view factor and the view factor obtained from the simulation is 1.24%. A trend of approximately 1% difference can be seen between the exact solutions and the simulation. When comparing this value to the results of the Monte Carlo method as was used by Hoff [48], the ray casting method seems to be delivering more accurate results since Hoff [48] claims a 2.2% error with simulation times of 4 minutes.

The simulation for the view factor of LiDAR data surfaces consists of multiple planar objects. Therefore it is necessary that the simulation works for these geometries. According to Hamilton and Morgan [49] the exact solution for the view factor from a differential planar surface to a finite parallel planar rectangle where the normal of surface 1 passes through the corner of surface 2 is found in equation 6.21.

$$F_{d1-2} = \frac{1}{2\pi}(\frac{A}{\sqrt{1+A^2}}\tan^{-1}(\frac{B}{\sqrt{1+A^2}}) + \frac{B}{\sqrt{1+B^2}}\tan^{-1}(\frac{A}{\sqrt{1+B^2}})), \tag{6.21}$$

where $A = \frac{a}{c}$ and $B = \frac{b}{c}$ with a and b being the sides of the rectangle and c being the distance between surface 1 and the corner of surface 2 which the normal of of surface 1 passes through. This is illustrated in figure 6.3.

To compare the results of the simulation to the exact value of F_{d12}, the values 300, 200 and 100 are chosen for a, b and c respectively in both the simulation and equation 6.21. This gives 3 and 2 for A and B respectively. Using these parameters in equation 6.21, the exact view factor for F_{d12} is found solving equation 6.22.

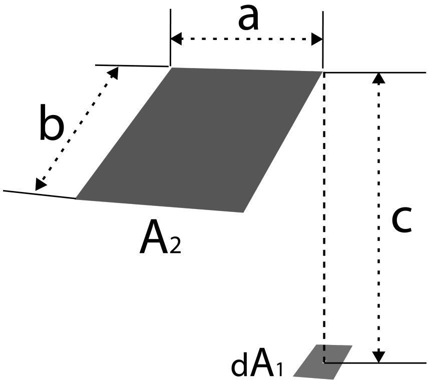

Figure 6.3: The view factor for a differential planar surface 1 to finite parallel rectangle surface 2 where normal of surface 1 passes through a corner of surface 2.

$$F_{d1-2} = \frac{1}{2\pi}(\frac{3}{\sqrt{1+3^2}}\tan^{-1}(\frac{2}{\sqrt{1+3^2}}) + \frac{2}{\sqrt{1+2^2}}\tan^{-1}(\frac{3}{\sqrt{1+2^2}})) = 0.21758 \tag{6.22}$$

The same geometry and parameters together with equation 6.17 have been used for the simulation which gives a view factor of 0.21756. The difference between the exact value of the view factor and the view factor which has been found using the simulation using 200000 rays in total has a difference in percentage of 0.009%. This proves that the view factor of a differential plane to a planar surface can also be found using the simulation with the corrected equation 6.17.

6.8. Using the reciprocity rule to determine the view factor from the surface to the PV module

Equation 6.17 gives the view factor for PV module -> A_j because the rays are cast from the position of the PV module. A_j is one of the surfaces which are visible to the PV module. In the simulation, A_j is a surface which diffusely reflects the light from the sun. Therefore it is necessary to know the view factor F_{j-i} as opposed to F_{i-j} which is obtained from equation 6.17. However, when the area of the PV module and the area of A_j is known, the view factor F_{j-i} can be easily determined using the reciprocity rule which has been explained in section 6.3. From equation 6.4 the view factor F_{j-i} can be derived resulting in equation 6.23.

$$F_{j-i} = F_{i-j}\frac{A_{PV}}{A_j} \tag{6.23}$$

This makes it very easy and relatively fast to calculate the view factor for each of the surfaces F_{j-i}. There is no need to solve the double integral formula 6.2 and this rule is applicable to any geometry of the surfaces. The view factor that is obtained for each of the surfaces can be used to calculate what part of the reflected light will reach the PV module.

6.9. Conclusions

When looking at the comparison between the simulation results and the exact solutions it becomes clear that the view factor can be accurately determined using the ray casting method. One of its strongest points is the fact that the complex double integral does not need to be solved. However, the strongest application of the ray casting method is the ability to determine the view factor of multiple surfaces at the same time. Along with the reciprocity rule this creates a very powerful tool which allows the estimation of the view factor from thousands of surfaces to the PV module in a matter of minutes instead of days if the view factor of each surface to the PV module had to be determined one by one.

7

Sun path

The sun path is an essential tool for all irradiance models since it is needed to determine the angle of incidence on a PV module. The model used in this thesis takes it a step further and also checks for shading. This chapter explains how the position of the sun is determined. Then, the shading factor is explained along with its uses and importance. Also, the way that the angle of incidence is determined is shown and finally, the importance of the simulation time steps are made clear.

7.1. Sun path

The Sun path is the path that the Sun seems to take from the perspective of the surface of the Earth. In fact, what is observed, is the trajectory of the Earth around the Sun and the rotation of the Earth. the Sun path of a location changes daily, seasonally and even yearly. In order to calculate the annual irradiation on a surface, the exact path of the Sun over the whole year is required for that location. The position of the Sun from the perspective of the surface is expressed in the solar azimuth and solar altitude. The solar azimuth (A_s) is the angle of the Sun with respect to the North and the solar altitude (a_s) is the angle of the Sun with respect to the horizon. This is illustrated in figure 7.1 where in this case the observer is the location of the surface and the object is the Sun.

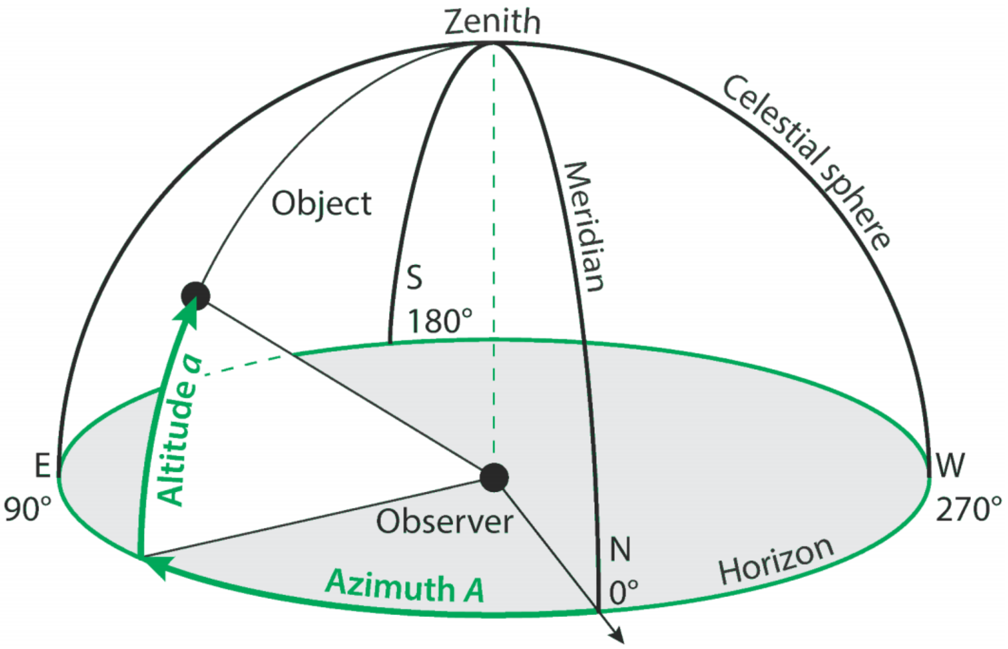

Figure 7.1: An illustration of the solar azimuth (A_s) and the solar altitude (a_s) [4].

The range of the solar azimuth is from 0 to 360 degrees and its orientation is clockwise with North, East, South and West being 0, 90, 180 and 270 degrees, respectively. The range of the solar altitude is -90 to 90 degrees, where the negative angles represent the Sun being below the horizon.
The location of the surface is expressed in the longitude and latitude, where the longitude (λ_0) is the angle of the location with respect to the prime meridian or Greenwich meridian, which is located in England. The latitude (ϕ_0) is the angle between the location and the Equator. This is illustrated in figure 7.2.

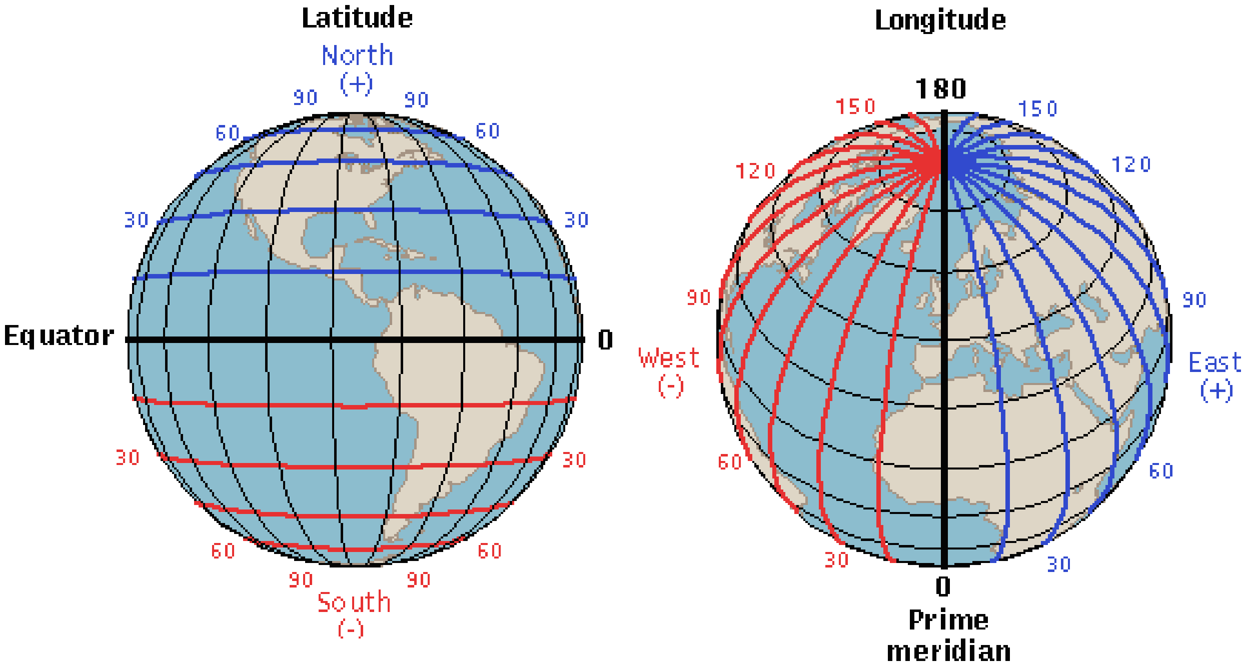

Figure 7.2: An illustration of the latitude (ϕ_0) and the longitude (λ_0) [15].

It is noteworthy that North gives a positive latitude and south gives a negative latitude. Also, Eastward from the Greenwich meridian gives a positive longitude and Westward from the Greenwich meridian gives a negative longitude. The range of the latitude is -90 to 90 degrees, while the range of the longitude is -180 degrees to 180 degrees.

7.2. Position of the Sun

The three parameters required to determine the azimuth and altitude of the Sun are the time, the longitude and latitude of the location. The longitude and latitude of the location are static in most cases, while the time can be either static if the azimuth and altitude are required only for a single time step or a variable.

The azimuth of the Sun is given by equation 7.1.

$$A_S = \tan^{-1}\left(\frac{\upsilon}{\xi}\right) = \tan^{-1}\left(\frac{-\sin\theta_L \ \cos\lambda_S + \cos\epsilon \ \sin\lambda_S}{-\sin\phi_0 \ \cos \ \theta_L \ \cos\lambda_S - (\sin\phi_0 \ \sin\theta_L \ \cos\epsilon - \cos\phi_0 \ \sin\epsilon)\sin\lambda_S}\right) \tag{7.1}$$

, where υ and ξ are the numerator and the denominator of equation 7.1 respectively and the altitude of the Sun is given by equation 7.2.

$$a_S = \zeta = \sin^{-1}\left(-\cos\phi_0 \ \cos \ \theta_L \ \cos\lambda_S + (\cos\phi_0 \ \sin\theta_L \ \cos\epsilon - \sin\phi_0 \ \sin\epsilon)\sin\lambda_S\right). \tag{7.2}$$

θ_L is the local mean sidereal time, which is the angle between the vernal equinox and the meridian. The vernal equinox is the position of the Sun around the 21 of March (which is the moment in which the sun passes exactly over the equator) and ϵ is the axial tilt angle which is approximately 23.429 degrees. These concepts can be seen in figure 7.3.

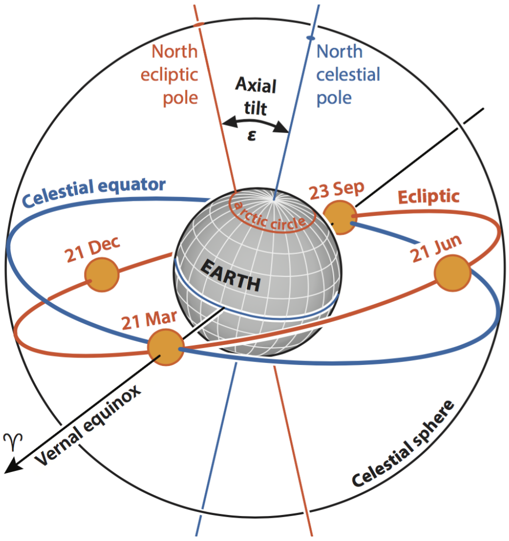
North ecliptic pole
Axial tilt
ε
North celestial pole
Celestial equator
23 Sep
Ecliptic
arctic circle
21 Dec
EARTH
21 Jun
21 Mar
♈
Vernal equinox
Celestial sphere

Figure 7.3: An illustration of the apparent movement of the Sun around the Earth, where the vernal equinox is depicted with Υ and the axial tilt $\epsilon \approx 23.4$ degrees [4].

The local mean sidereal time θ_L is given by equation 7.3.

$$\theta_L = GMST\frac{15}{h} + \lambda_0, \tag{7.3}$$

where GMST is the Greenwich mean sidereal time which is approximated by equation 7.4.

$$GMST = 18.697374558h + 24.06570982441908h\ D + 0.000026h\ T^2, \tag{7.4}$$

in which h is the hour angle. D and T are the amount of days and centuries elapsed since the first of January 2000, respectively. The hour angle h is given by equation 7.5.

$$h = \theta_L - \alpha, \tag{7.5}$$

where α is the right ascension. These concepts are made clear by figure 7.4.

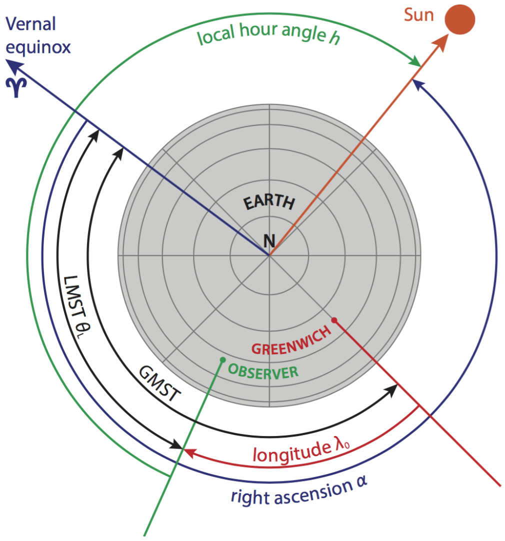
Vernal equinox
♈
local hour angle h
Sun
EARTH
N
LMST θL
GMST
GREENWICH
OBSERVER
longitude λ0
right ascension α

Figure 7.4: An illustration of the hour angle h, GMST, LMST θ_L, right ascension α and longitude λ_0 [4].

λ_S is the ecliptic longitude of the Sun, which is given by equation 7.6.

$$\lambda_S = q + 1.915^o + \sin\ g + 0.02^o \sin 2g, \tag{7.6}$$

for which q is the mean longitude of the Sun corrected for the aberration of the light and is given by equation 7.7.

$$q = 280.459^o + 0.98564736^o D \tag{7.7}$$

and the mean anomaly of the Sun g is given by equation 7.8.

$$g = 357.529^o + 0.98560028^o D. \tag{7.8}$$

The obtained altitude of the Sun a_S is given between -90 and 90 degrees, which is the required range for the altitude of the Sun. The azimuth of the Sun however, is also given between -90 and 90 degrees, which is not the required range. The range required for the azimuth is 0 to 360 degrees and in order to fulfill this requirement, first the quadrant that A_s is in has to be found and for it, the statements of 7.9, 7.10 and 7.11 are checked.

$$If\ \xi\ >\ 0 \wedge \upsilon\ >\ 0\ \rightarrow\ A_s = A_s \tag{7.9}$$

$$If\ \xi\ <\ 0\ \rightarrow\ A_s = A_s + 180^o \tag{7.10}$$

$$If\ \xi\ >\ 0 \wedge \upsilon\ <\ 0\ \rightarrow\ A_s = A_s + 360 \tag{7.11}$$

A more elaborate description of the position of the Sun is given by the Solar Energy book by Smets et al. [4].

7.3. Shading factor

The shading factor (SF) is a factor which implies what fraction of a PV module does not receive any direct radiation. This fraction is a number between 0 and 1, however in some applications the shading factor can also be only 0 or 1. When the time step of a simulation is rather large, it is sufficient to use a binary shading factor.

Shading is determined by checking whether there is an obstruction between the Sun and the PV module surface. This checking is done in the simulation by performing a ray cast in the direction of the center of the PV module. This ray is either able to reach the PV module, implying that there is no shading on the PV module, or it can hit an object in between, meaning that there is shading on the PV module on that exact time step. In the first case, the shading factor would be 0 and in the second case the shading factor would be 1. This has been illustrated in figure 7.5.

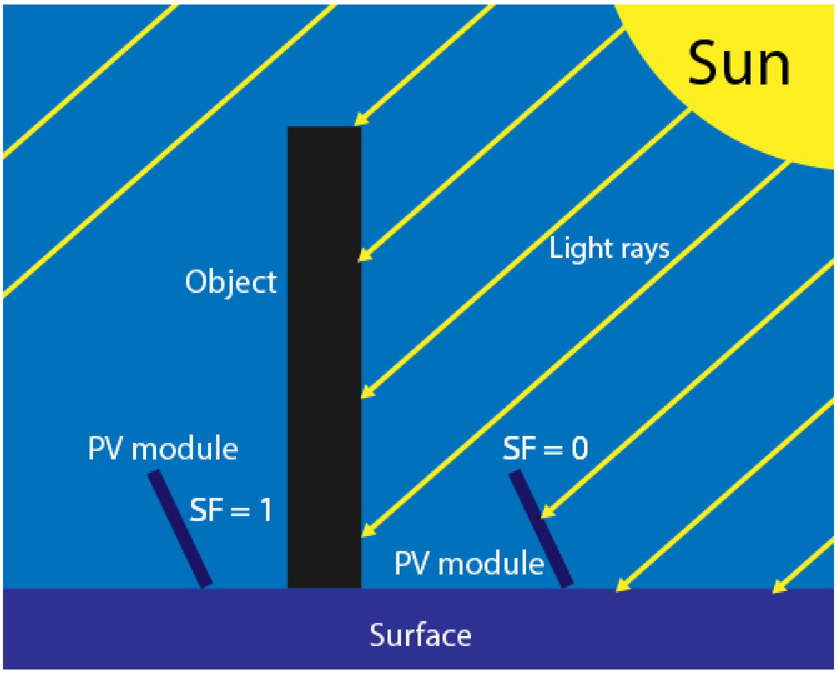

Figure 7.5: An illustration for the concept of shading factor.

The illustration resembles a 2 dimensional situation, but of course the same concept holds up for a 3 dimensional case.
The three factors which determine the shading factor are the geometry of the surroundings of the location, position of the PV module and the time. The three dimensional geometry of the location is obtained using LiDAR data and then the PV module can be placed anywhere in the three dimensional environment, where after the shading factor can be determined with respect to time, thus resulting in a shading analysis limited by the accuracy of the LiDAR data.

7.3.1. Shading analysis example

Using the simulation model, a shading analysis has been made for a real world scenario. Also a shading analysis has been done for a solar bike station in front of the faculty of electrical engineering, mathematics and computer science (EWI), because this location is the main location where the simulation is tested on. The shading factor has been given in percentages. For each month, the 21st day has been chosen to perform the shading analysis on. Of course, the shading analysis can be done for each day of the year and with smaller time steps. Also, for the shading analysis, the shading was checked on 9 points of the PV modules. This could also be done for example for 36 points on the PV module or on each of the PV cells of a PV module.
Figure 7.6 shows the southward orientation view of the solar bike station in front of the EWI building.

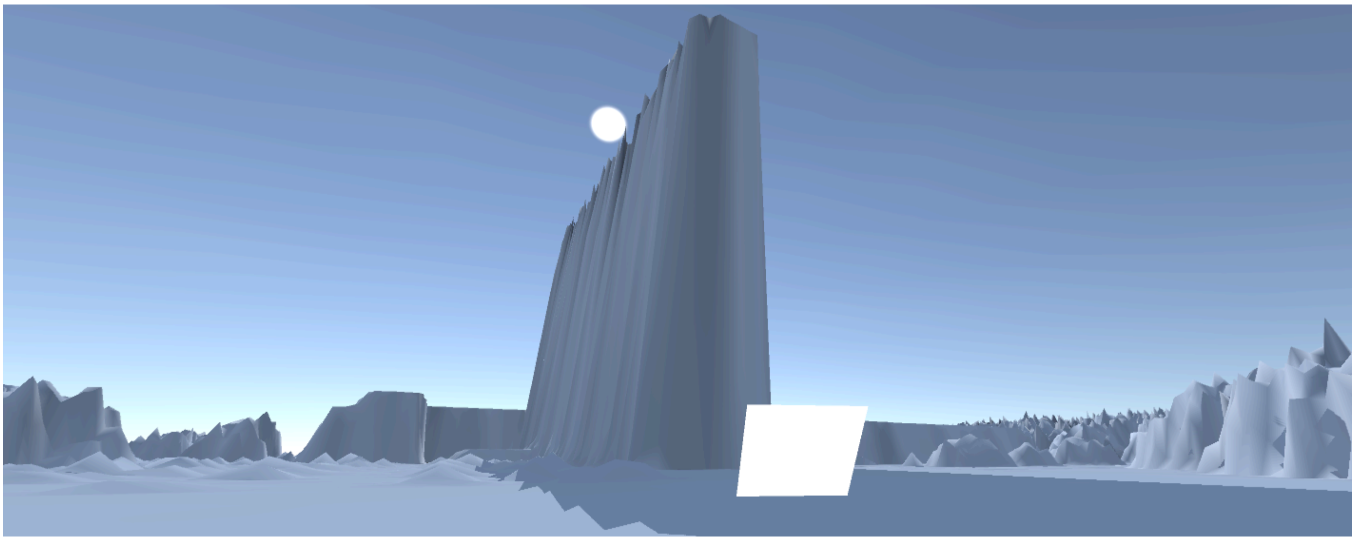

Figure 7.6: The solar bike station with the EWI building to its southward direction.

It is clear that since the EWI building is at the southern side of the solar bike station, there will be shading in the middle of the day. The results of the shading analysis on the solar bike station have been tabulated in table 7.1.

From 7.1 it becomes clear that indeed during the day a large shade casts over the PV module. During winter, there is even more shade because the Sun does not reach as high.
For another scenario, PV modules have been placed upon the roof of a power station in the campus of TU Delft and the shading factor for different times has been determined. For the analysis a dual axis solar tracker and single axis solar tracker PV systems have been used. Figure 7.7 shows how the PV modules are placed upon the roof of the power station.

The results of the analysis have been tabulated for the dual axis solar tracker and single axis solar tracker PV systems in tables 7.2 and 7.3 respectively.

Compared to the results of the shading analysis of the solar bike station, the results of the power station are more promising. Of course however, tracking the Sun will increase the chance that the Sun will radiate on the front surface of the PV module instead of the back side of the PV module, which will not result in any power production unless a bifacial PV module is used. The main advantage, however, is due to the more open area in front of the power station. Mounting the PV modules on the building considerably reduced the shading as well. In order to know what the impact of placing the PV modules at the back side will be, another shading analysis has been done, where the PV modules are moved

Table 7.1: Shading factor of solar bike station in front of the EWI building.

SF (%)	**Jan**	**Feb**	**Mar**	**Apr**	**May**	**Jun**	**Jul**	**Aug**	**Sep**	**Okt**	**Nov**	**Dec**
0:00	100	100	100	100	100	100	100	100	100	100	100	100
1:00	100	100	100	100	100	100	100	100	100	100	100	100
2:00	100	100	100	100	100	100	100	100	100	100	100	100
3:00	100	100	100	100	100	100	100	100	100	100	100	100
4:00	100	100	100	100	100	100	100	100	100	100	100	100
5:00	100	100	100	100	100	100	100	100	100	100	100	100
6:00	100	100	100	100	100	100	100	100	100	100	100	100
7:00	100	100	100	100	100	66	100	100	100	100	100	100
8:00	100	100	100	100	11	0	22	100	100	100	100	100
9:00	100	100	100	0	0	0	0	0	55	100	100	100
10:00	100	66	0	0	0	0	0	0	0	0	100	100
11:00	0	0	0	0	0	0	0	0	0	0	11	22
12:00	0	0	0	0	0	0	0	0	0	0	0	11
13:00	55	22	22	22	0	0	0	0	66	100	100	100
14:00	100	100	100	100	66	100	100	100	100	77	100	100
15:00	33	33	11	0	0	0	0	0	0	0	11	33
16:00	0	0	0	0	0	0	0	0	0	0	0	11
17:00	11	0	0	0	0	0	0	0	0	0	66	100
18:00	100	22	22	11	0	0	0	11	33	100	100	100
19:00	100	100	77	33	0	0	0	22	100	100	100	100
20:00	100	100	100	33	0	0	0	33	100	100	100	100
21:00	100	100	100	100	66	55	55	100	100	100	100	100
22:00	100	100	100	100	100	100	100	100	100	100	100	100
23:00	100	100	100	100	100	100	100	100	100	100	100	100

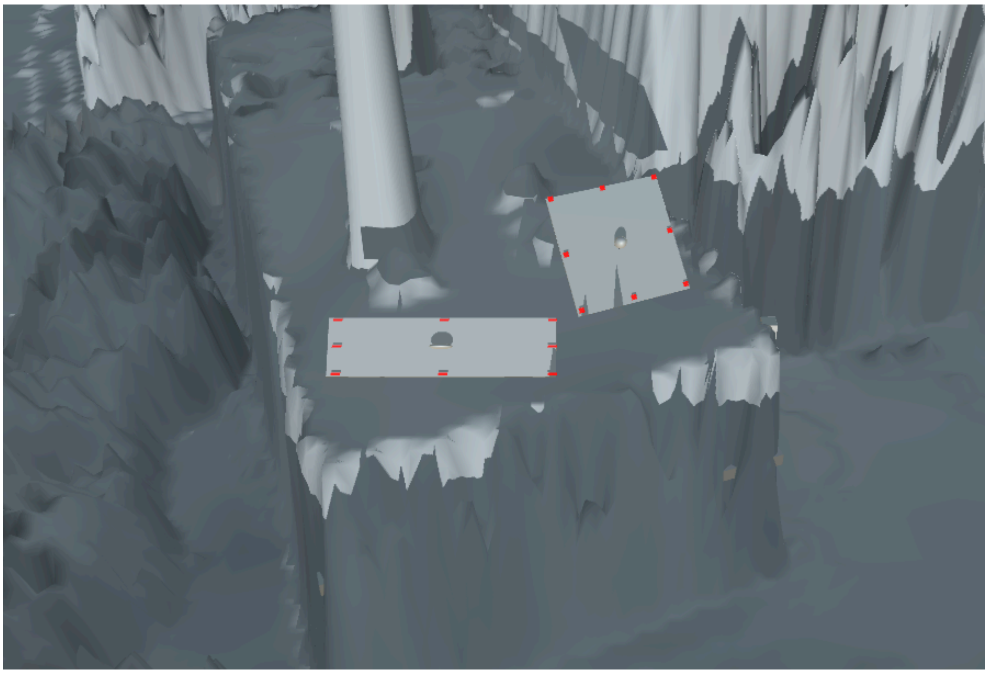

Figure 7.7: An illustration showing the PV modules placed on the roof of the power station.

to the other side of the chimney, which is referred to as spot 2. Figure 7.8 shows a screen shot of the simulation for how the PV modules for both spots are placed [1].

---

[1] The study was performed as request of architectural council of Delft municipality.

Table 7.2: Shading factor of the dual axis solar tracker in percentages.

SF (%)	Jan	Feb	Mar	Apr	May	Jun	Jul	Aug	Sep	Okt	Nov	Dec
0:00	100	100	100	100	100	100	100	100	100	100	100	100
1:00	100	100	100	100	100	100	100	100	100	100	100	100
2:00	100	100	100	100	100	100	100	100	100	100	100	100
3:00	100	100	100	100	100	100	100	100	100	100	100	100
4:00	100	100	100	100	100	100	100	100	100	100	100	100
5:00	100	100	100	100	100	100	100	100	100	100	100	100
6:00	100	100	100	100	100	66	66	100	100	100	100	100
7:00	100	100	100	100	0	0	0	100	100	100	100	100
8:00	100	100	100	0	0	0	0	0	100	100	100	100
9:00	100	100	0	0	0	0	0	0	0	100	100	100
10:00	22	0	0	0	0	0	0	0	0	0	66	66
11:00	0	0	0	0	0	0	0	0	0	0	0	55
12:00	0	0	0	0	0	0	0	0	0	0	0	0
13:00	0	0	0	0	0	0	0	0	0	0	0	0
14:00	0	0	0	0	0	0	0	0	0	0	0	0
15:00	11	11	0	0	0	0	0	0	0	11	11	11
16:00	22	11	11	11	11	11	11	11	11	11	22	22
17:00	77	22	11	11	11	11	0	0	22	11	100	100
18:00	88	44	22	11	0	0	0	11	22	44	55	88
19:00	100	33	11	11	0	0	0	11	11	88	100	100
20:00	100	100	11	33	33	44	33	33	33	100	100	100
21:00	100	100	100	55	66	66	33	55	100	100	100	100
22:00	100	100	100	100	66	33	55	100	100	100	100	100
23:00	100	100	100	100	100	100	100	100	100	100	100	100

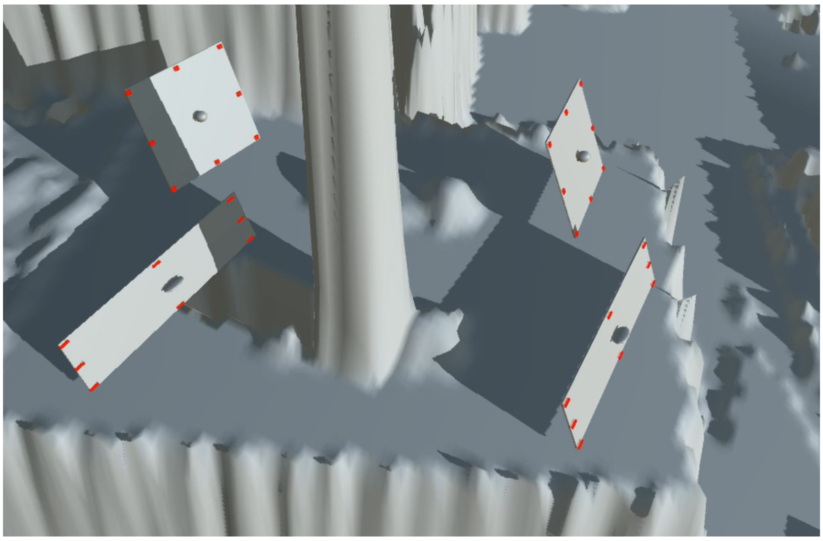

Figure 7.8: An illustration showing the PV modules placed on the roof of the power station for both spots, where the PV modules at the left hand side are the PV modules at the second spot and the PV modules at the right hand side are again the PV modules on the first or original spot.

The results have again been tabulated and can be seen for the dual axis solar tracker and single axis solar tracker both at the second spot in table 7.4 and 7.5, respectively.

When comparing the tables, it becomes obvious that placing the PV modules on the back side of the roof will cause significantly more shading and therefore from a maximum energy yield perspective it is not a wise choice.
Another great use of the shading analysis would be to analyze the shading of PV modules in a PV farm,

Table 7.3: Shading factor of the single axis solar tracker in percentages.

SF (%)	**Jan**	**Feb**	**Mar**	**Apr**	**May**	**Jun**	**Jul**	**Aug**	**Sep**	**Okt**	**Nov**	**Dec**
0:00	100	100	100	100	100	100	100	100	100	100	100	100
1:00	100	100	100	100	100	100	100	100	100	100	100	100
2:00	100	100	100	100	100	100	100	100	100	100	100	100
3:00	100	100	100	100	100	100	100	100	100	100	100	100
4:00	100	100	100	100	100	100	100	100	100	100	100	100
5:00	100	100	100	100	100	100	100	100	100	100	100	100
6:00	100	100	100	100	66	66	66	100	100	100	100	100
7:00	100	100	100	66	66	66	66	0	100	100	100	100
8:00	100	100	0	0	0	22	11	0	33	100	100	100
9:00	100	55	0	0	0	0	0	0	0	0	100	100
10:00	66	0	0	0	0	0	0	0	0	0	0	77
11:00	33	0	0	0	0	0	0	0	0	0	0	0
12:00	0	0	0	0	0	0	0	0	0	0	0	0
13:00	0	0	0	0	0	0	0	0	0	0	0	0
14:00	0	0	0	0	0	0	0	0	0	0	0	0
15:00	0	0	0	0	0	0	0	0	0	0	0	0
16:00	0	0	0	0	0	0	0	0	0	0	44	66
17:00	100	0	0	0	0	0	0	0	0	0	100	100
18:00	44	0	0	0	0	0	0	0	0	0	33	66
19:00	100	0	11	0	0	0	0	0	88	88	100	100
20:00	100	100	11	0	0	0	0	0	44	100	100	100
21:00	100	100	100	0	0	0	0	0	100	100	100	100
22:00	100	100	100	100	55	33	55	100	100	100	100	100
23:00	100	100	100	100	100	100	100	100	100	100	100	100

where PV modules often shade the PV modules mounted behind them. A shading analysis for each of the PV modules of a PV farm would be possible delivering great insights before constructing the PV farm. Also it would show shading of objects in the surrounding on some of the PV modules, while other PV modules may not be shaded. This creates an imbalance which is not preferred.

7.4. Angle of incidence

Another parameter which can be determined as a consequence of the knowledge of the position of the Sun with respect to the PV module is the angle of incidence (AOI or γ). The AOI is the angle between the normal of the PV module and the direction of the Sun from the PV module. This has been illustrated for a 2 dimensional case in figure 7.9.

For a 3 dimensional case, the AOI can also be determined if the positions of the PV module and the Sun are known. As was discussed previously, the position of the Sun is expressed in the altitude (a_s) and the azimuth (A_s), which are required to determine the AOI. The position of the PV module is described by the direction of the PV module normal in horizontal coordinates (A_M, a_M). A_M is the angle of the projection of the normal of the module onto the horizontal plane and due north while $a_M = 90 - \theta_M$. The angles regarding the PV module have been illustrated in figure 7.10.

The angles that are required to determine the AOI are now known and used in equation 7.12 [4].

$$\gamma = \cos^{-1}(\cos\, a_M\ \cos\, a_S\ \cos(A_M - A_S) + \sin\, a_M\ \sin\, a_S) \tag{7.12}$$

Equation 7.12 can also be written in terms of the tilt angle θ_M of the PV module as is done in equation 7.2 [4].

$$\gamma = \cos^{-1}(\sin\, \theta_M\ \cos\, a_S\ \cos(A_M - A_S) + \cos\, \theta_M\ \sin\, a_S), \tag{7.13}$$

where the tilt relates to the altitude of the PV module as is given by equation 7.14.

$$a_M = 90 - \theta_M. \tag{7.14}$$

Table 7.4: Shading factor of the dual axis solar tracker in percentages for the location at the back side of the roof behind the chimney.

SF (%)	**Jan**	**Feb**	**Mar**	**Apr**	**May**	**Jun**	**Jul**	**Aug**	**Sep**	**Okt**	**Nov**	**Dec**
0:00	100	100	100	100	100	100	100	100	100	100	100	100
1:00	100	100	100	100	100	100	100	100	100	100	100	100
2:00	100	100	100	100	100	100	100	100	100	100	100	100
3:00	100	100	100	100	100	100	100	100	100	100	100	100
4:00	100	100	100	100	100	100	100	100	100	100	100	100
5:00	100	100	100	100	100	100	100	100	100	100	100	100
6:00	100	100	100	100	100	100	100	100	100	100	100	100
7:00	100	100	100	100	100	100	100	100	100	100	100	100
8:00	100	100	100	100	100	100	100	100	100	100	100	100
9:00	100	100	77	88	100	100	100	88	66	100	100	100
10:00	55	44	55	55	55	77	66	55	44	33	66	100
11:00	11	22	22	22	22	33	33	22	11	0	22	22
12:00	22	11	0	0	0	11	0	0	0	22	22	44
13:00	33	0	0	0	0	0	0	0	0	0	22	22
14:00	11	0	0	0	0	0	0	0	0	0	0	11
15:00	33	33	33	33	33	33	33	44	44	55	33	33
16:00	55	44	44	33	11	11	11	33	44	44	88	55
17:00	66	44	11	0	11	11	0	0	22	11	44	100
18:00	55	44	22	11	0	0	0	11	22	44	100	88
19:00	100	33	11	11	0	0	0	11	11	44	100	100
20:00	100	100	0	0	0	0	0	0	33	100	100	100
21:00	100	100	100	33	0	0	0	33	100	100	100	100
22:00	100	100	100	100	88	77	66	100	100	100	100	100
23:00	100	100	100	100	100	100	100	100	100	100	100	100

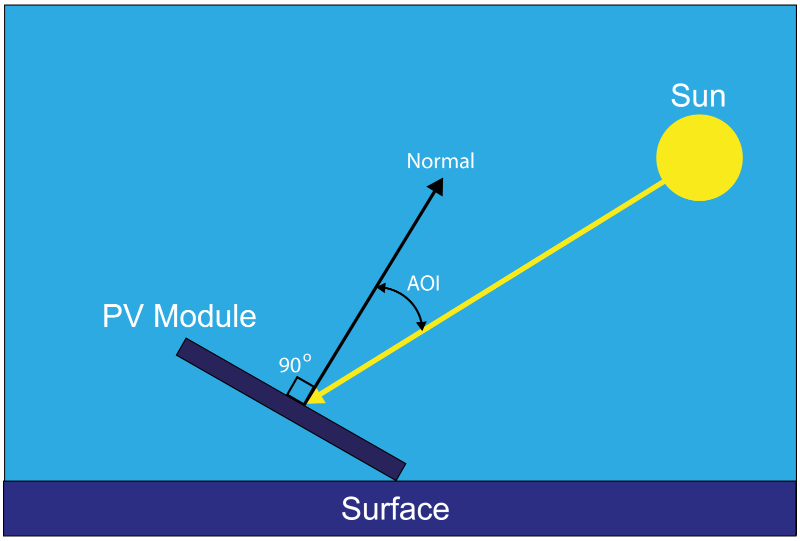

Figure 7.9: An illustration showing the concept of the angle of incidence.

A dual axis solar tracker will strive to keep the altitude of the PV module the same as the altitude of the Sun and also to keep the azimuth of the PV module the same as the azimuth of the Sun. Therefore, the AOI is 0 and thus cos 0 is 1, which means that the maximum direct irradiance is irradiated on a PV module. A single axis solar tracker will either strive to keep both azimuths the same or both altitudes the same. This will decrease the AOI as well, though not as much as a dual axis solar tracker. Now the AOI can be used in order to determine the G_M^{dir} on the PV module as was shown in chapter 2.

Table 7.5: Shading factor of the single axis solar tracker in percentages for the location at the back side of the roof behind the chimney.

SF (%)	**Jan**	**Feb**	**Mar**	**Apr**	**May**	**Jun**	**Jul**	**Aug**	**Sep**	**Okt**	**Nov**	**Dec**
0:00	100	100	100	100	100	100	100	100	100	100	100	100
1:00	100	100	100	100	100	100	100	100	100	100	100	100
2:00	100	100	100	100	100	100	100	100	100	100	100	100
3:00	100	100	100	100	100	100	100	100	100	100	100	100
4:00	100	100	100	100	100	100	100	100	100	100	100	100
5:00	100	100	100	100	100	100	100	100	100	100	100	100
6:00	100	100	100	100	100	100	100	100	100	100	100	100
7:00	100	100	100	100	100	100	100	100	100	100	100	100
8:00	100	100	22	55	66	100	100	77	44	100	100	100
9:00	100	55	11	0	0	11	0	0	0	11	100	100
10:00	55	66	11	0	0	0	0	0	11	66	77	100
11:00	100	88	44	11	0	0	0	11	44	77	66	66
12:00	77	44	33	33	33	33	33	33	22	44	33	88
13:00	44	33	33	33	33	33	33	33	33	33	44	44
14:00	0	0	0	0	33	11	0	0	22	33	33	11
15:00	33	33	33	33	22	11	33	33	33	33	33	33
16:00	33	22	0	0	0	0	0	0	0	0	11	100
17:00	33	0	0	0	0	0	0	0	0	0	0	100
18:00	66	11	0	0	0	0	0	0	0	22	100	100
19:00	100	0	0	0	0	0	0	0	0	33	100	100
20:00	100	100	0	0	0	0	0	0	44	100	100	100
21:00	100	100	100	22	0	0	0	0	100	100	100	100
22:00	100	100	100	100	55	11	44	100	100	100	100	100
23:00	100	100	100	100	100	100	100	100	100	100	100	100

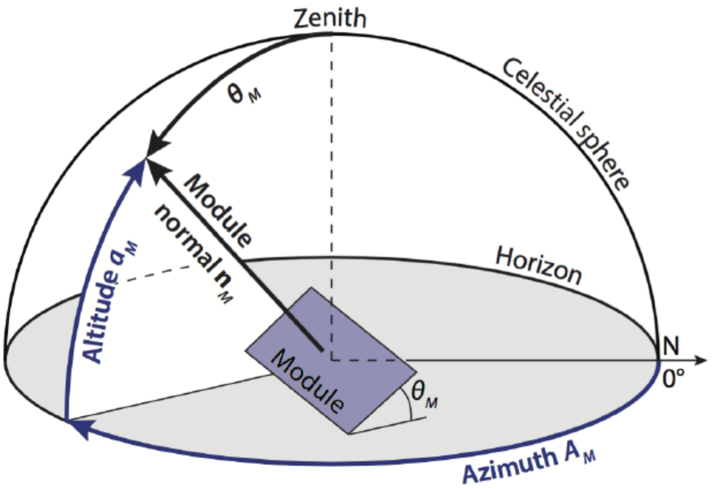

Figure 7.10: An illustration showing the angles regarding the PV module [4].

7.5. Simulation time steps

The simulation time steps basically determines how often the irradiance on a PV module is calculated. As the time steps become smaller, the simulation will increasingly resemble the real-time irradiation. As was discussed in chapter 2, an important aspect which determines the time step is the meteorological data that is available. Another aspect is the simulation time, because more time steps means more calculations and evidently more computation time. A time step which is too large may cause the simulation to skip certain situations. As an example, between 12:30 and 13:30, the Sun may pass behind a high building or any other object for that matter. If the simulation has a time step of 1 hour or less, the Sun will as a consequence pass behind the building at least 1 time, during a day. If there is a larger time step, this event might be skipped completely, while in reality this event would happen. As a result, the simulated irradiance is too high with comparison to the real irradiance, which might cause problems. Figures 7.11 and 7.12 show an illustration of a possible simulation scenario, with a time step of 1 hour and 2 hours, respectively.

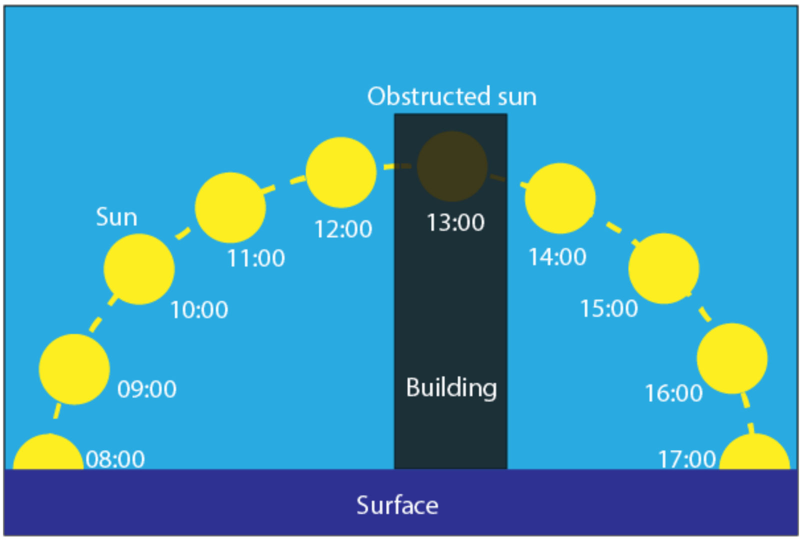

Figure 7.11: The Sun path with a time step of 1 hour, where the Sun for each time step is illustrated as a yellow circle and the actual sun path is illustrated as a dotted arc.

Figure 7.11 shows that for a time step of 1 hour, the event that the Sun is obstructed by a high building is indeed happening.

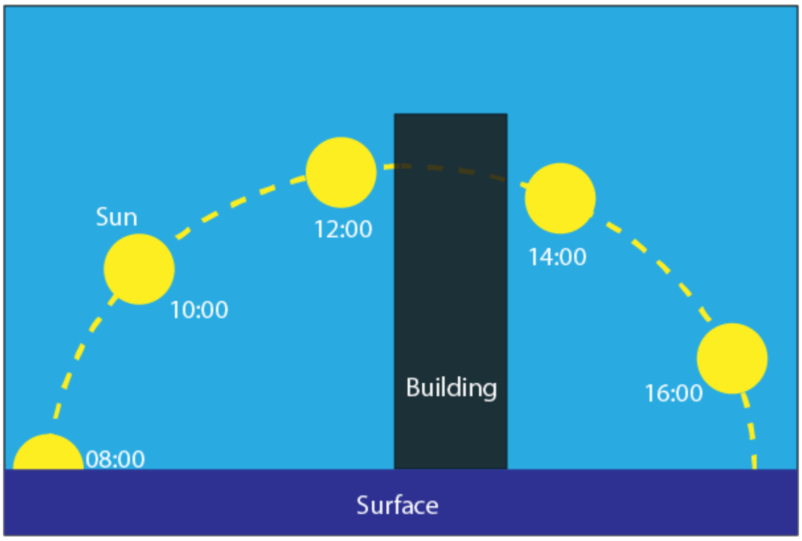

Figure 7.12: The Sun path with a time step of 2 hours, where the Sun for each time step is illustrated as a yellow circle and the actual sun path is illustrated as a dotted arc.

As can be seen from figure 7.12, the event that the Sun is obstructed by a high building does not happen, while it should have. This could happen for even more events and the effects would thus be higher.

If the simulation time step is 1 hour, the simulation would have to run the simulation for 8760 steps or 8784 steps depending on whether its simulating for a leap year or not. Now this number can be brought down if the steps in which the Sun is below the horizon are not computed. Figure 7.13 shows an illustration of the Sun hours for different latitudes per day.

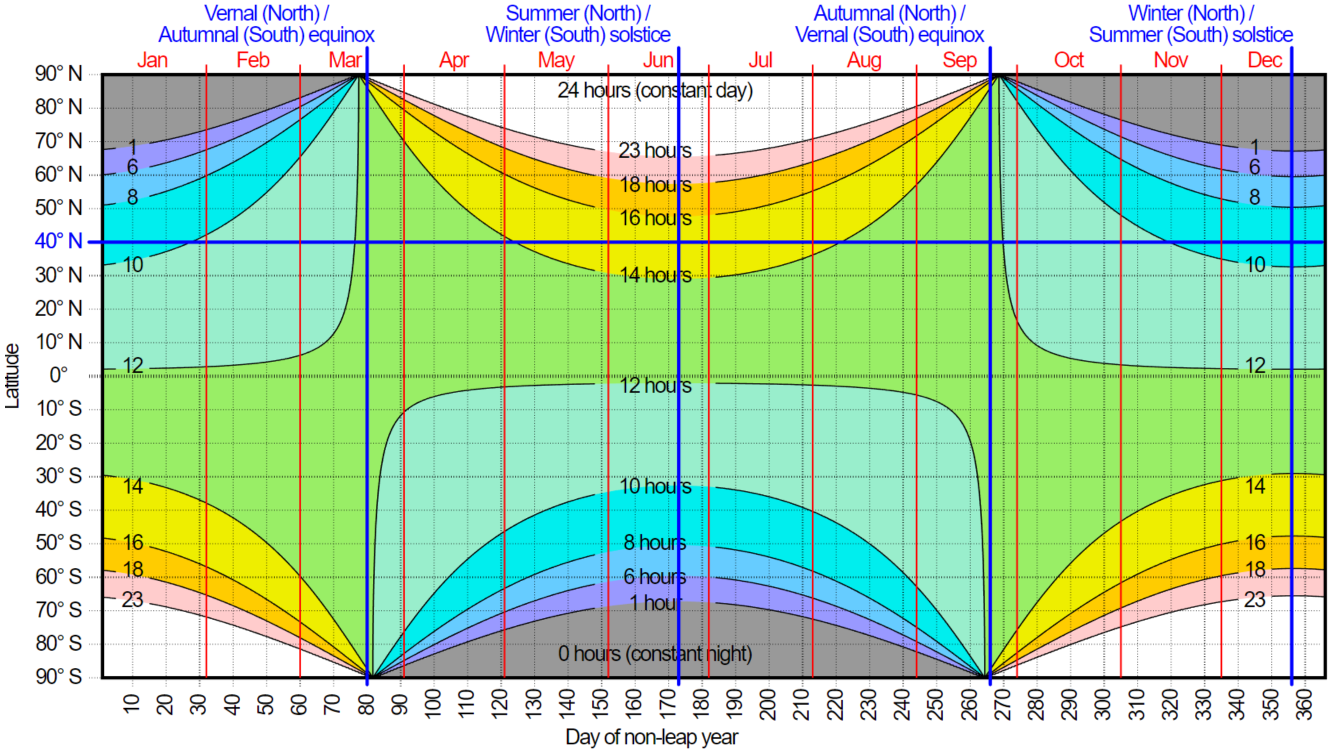

Figure 7.13: The Sun hours for different latitudes per day, where the blue line indicates the latitude of New York [16].

It becomes clear that for the northern hemisphere, less time steps are required for the winter as compared to the summer. For Delft, the simulation only has to run for approximately 8 hours on the 21st of December, while it has to run for approximately 16 hours on the 21st of June. On average there are approximately 12 hours per day in which the Sun is above the horizon over a year. Therefore, only 4380 time steps are required for the simulation, since the GHI is known beforehand for the other time steps.

7.6. Conclusions

The position of the sun is very important for the direct component of the sun since it affects the direct irradiance due to by means of the angle of incidence as well as the shading factor. A shading analysis can be done quickly to determine the shading throughout the day. The fact that this can be done fast is very useful since it can be used to reveal the least shaded locations for PV modules on a roof without having to estimate the total energy yield. This does not necessarily mean that the locations that are found are in fact the most optimal in terms of the total energy yield, however, it does give very useful indications of potential spots to place the PV modules.

Small simulation time steps may cause essential moments to be missed by the simulations. Smaller time steps are therefore preferred, but smaller time step does mean a higher simulation time. In the case of this thesis, the simulation time has been limited by the meteorological data.

8

Irradiance prediction

This chapter shows how an existing model predict the irradiance and how the ray casting model predicts the irradiance along with results of the annual energy yield predictions. A comparison between the two models is made, where after the effect of the albedo component on the irradiance is shown. Then the uses of the model for bifacial PV modules is shown along with results and how the energy yield on the back side of a bifacial PV module relates to the tilt angle. Finally, the bifacial PV module is compared to the monofacial PV module and conclusions are drawn.

8.1. Irradiance prediction

Determining the annual energy yield incident on a surface is the first step in the design of a PV system. Often when designing a PV system, there are certain criteria and bounds which have to be accounted for. A PV system may be bound to the usable areas on the roof of an household, while the household consumes a certain amount of energy. The PV system must then be designed at least such that the amount of energy that is consumed is produced by the PV modules using only the available roof areas. The energy incident on a roof is not always equal on all areas of the roof, therefore the most optimal location of the roof has to be found. In order to find this location, the energy incident on each part of the roof must be known. This requires a simulation.

8.2. Irradiance prediction using existing models

In this section, the irradiance prediction is done using a method which is fast, but does not take into account the environment of the PV system in question. The following assumptions are made for this model:

1. The location in which the PV system is located is completely flat,
2. The PV system has no shading,
3. The albedo is constant,
4. Meteonorm data is representative of the annual irradiance of the location.

The first two assumptions are especially important, because they are the key differences with respect to the irradiance prediction using the ray casting model, which is handled in section 8.3. Assumption 1 causes the sky view factor to be purely geometric in nature and assumption 2 causes the shading factor to be nonexistent.

The following variables do however have influence on the irradiance prediction:

1. Time at PV system location,
2. Longitude of PV system location,
3. Latitude of PV system location,
4. Azimuth of PV module,
5. Altitude of PV module,
6. Direct normal irradiance from Meteonorm data,
7. Diffuse horizontal irradiance from Meteonorm data,
8. Albedo factor.

From these variables, other variables are determined, which are consequently used in the calculation of the different components of irradiance on a surface. These variables are the altitude of the Sun, azimuth of the Sun, angle of incidence and the sky view factor. Finally together they are used to determine the total irradiance as a result of the three different components of irradiance.

8.2.1. The models used

For determining the direct component of irradiance, the model of equation 2.9 has been used, which was defined in equation 8.1.

$$G_M^{dir} = DNI \; cos \; AOI \tag{8.1}$$

For the diffuse component, the isotropic sky model has been used as shown in equation 2.11 of chapter 2.

$$G_M^{dif} = DHI \; SVF \tag{8.2}$$

Finally, the albedo component is approximated by Smets et al. [4] as in equation 8.3.

$$G_M^{ground} = GHI \; \alpha \; (1 - SVF) \tag{8.3}$$

8.2.2. Irradiance prediction using existing models results

The irradiance has been determined using the existing models for a tilted surface on an old power station in Delft using the meteorological data of Meteonorm. The powerstation that is used can be found in figure 8.1, whhere the PV module on the roof has been depicted as a blue square.

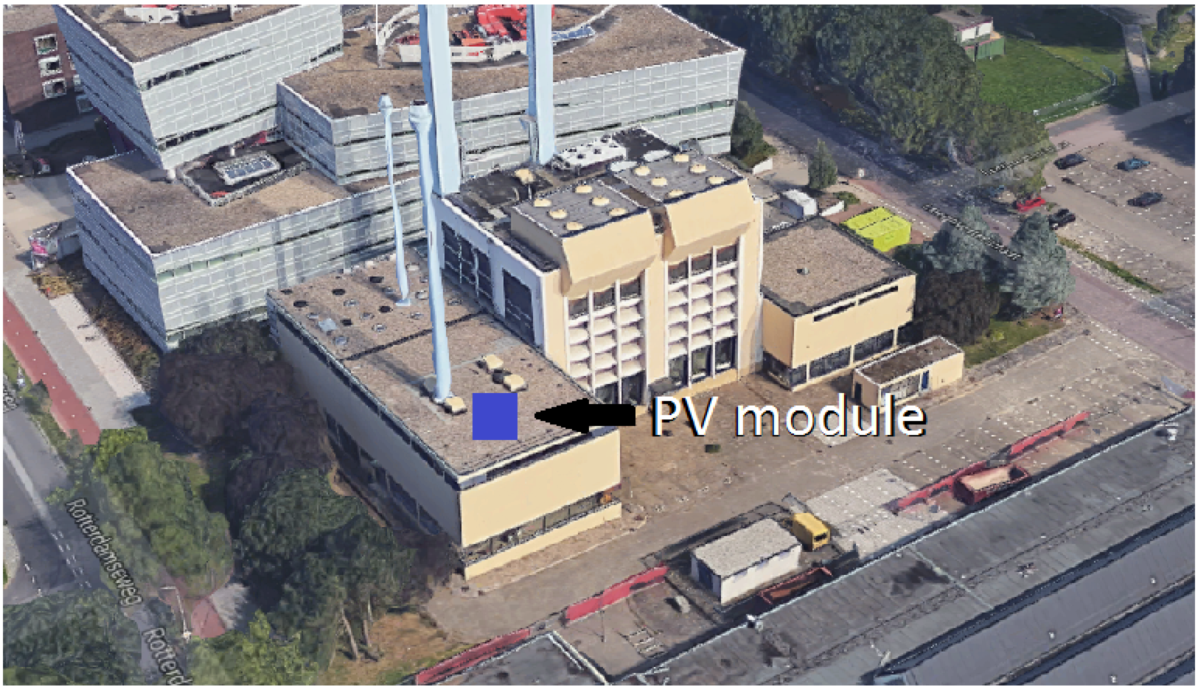

Figure 8.1: The power station used for the irradiance predictions, with the PV module depicted as a blue square [13].

The power station The variables that were used for the simulation can be seen in table 8.1. From the simulations the hourly irradiance on a surface has been determined for each of the three components of irradiance. The hourly direct irradiance G_M^{dir} on a surface can be seen in figure 8.2.

The direct component is the most unpredictable component of irradiance, since it can easily be blocked by clouds, however, it is still the most significant one with an annual energy yield of $622 kWh/m^2$. The second most significant component of irradiance is the diffuse component. The hourly diffuse irradiance G_M^{dif} on a surface can be seen in figure 8.3.

The diffuse component will always irradiate unless the Sun is below the horizon or if the visibility of the sky is completely blocked from the surface point of view. The total estimated annual energy yield

Table 8.1: The variables used to determine the irradiance on a surface.

Variables	Value
Longitude	4.4
Latitude	52
Azimuth	180°
Altitude	45°
Albedo factor	0.25

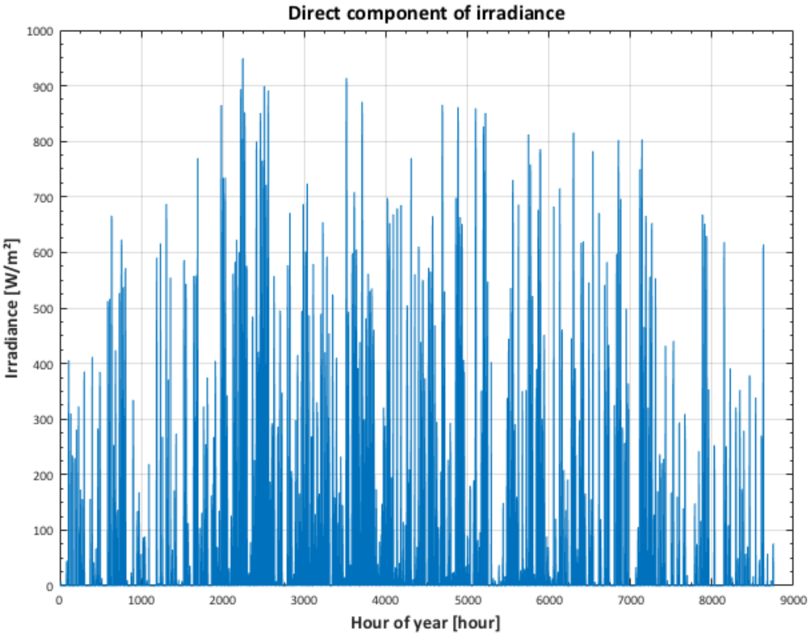

Figure 8.2: The direct component of irradiance per hour of a year for the existing model simulation.

of the diffuse component is $495kWh/m^2$. Finally, the albedo component has the least impact on the total irradiance. The hourly reflected irradiance G_M^{ground} on a surface can be seen in figure 8.4.

The annual energy yield due to the reflected irradiance is estimated to be $38kWh/m^2$, which is clearly less than the other components of irradiance. In fact, the albedo component accounts for 3.28% of the total predicted energy yield. The total hourly irradiance G_M on a surface can be seen in figure 8.5.

The total annual energy yield due to all components of irradiance is estimated to be $1156kWh/m^2$.

8.3. Irradiance prediction using the ray casting model

Using the ray casting model, the environmental factors are taken into account as well, making the method slower, but more reliable. The simulation time needed to estimate the annual irradiance on a surface is approximately 45 minutes, depending on the amount of surfaces that are adding to the albedo component of the irradiance. For the ray casting model, the assumptions that have been made are the following:

1. The geometry obtained using the Lidar data is realistic,
2. The albedo is constant,
3. Meteonorm data is representative of the annual irradiance of the location.
4. The PV module is initially assumed to be a differential surface.

Apart from the variables mentioned in section 8.2, the other factor which has an influence on the irradiance is the environment. Whenever the sun is behind a building, the shading factor becomes 1, thus the direct component of the sun is blocked. Depending on the location, the sky view factor is no

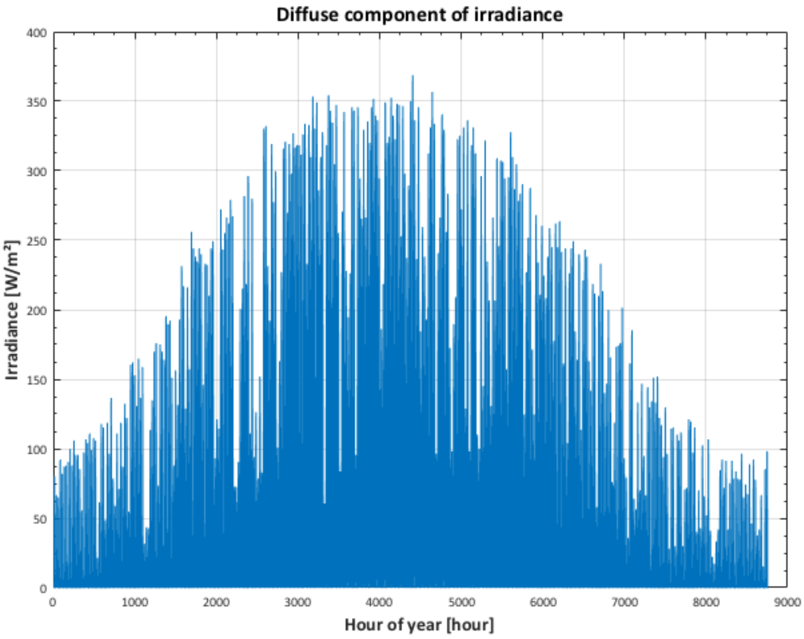

Figure 8.3: The diffuse component of irradiance per hour of a year for the existing model simulation.

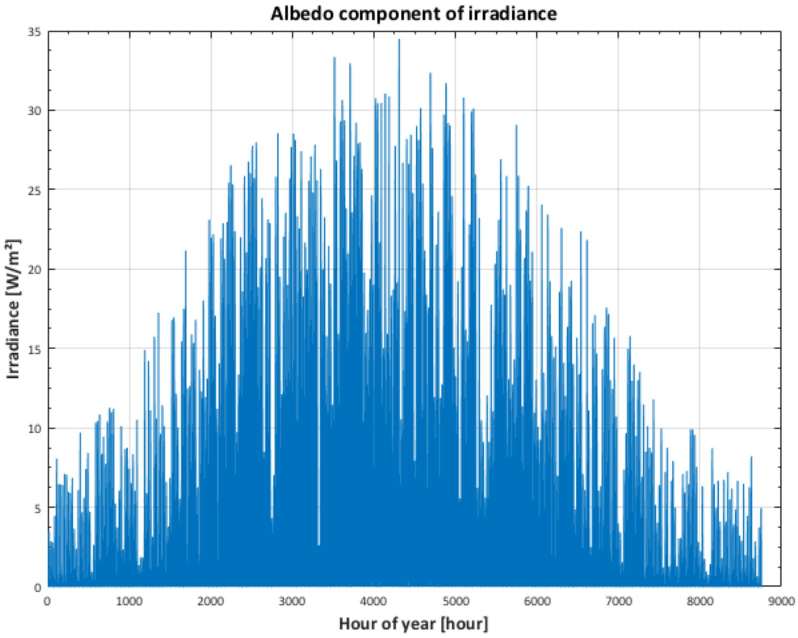

Figure 8.4: The albedo component of irradiance per hour of a year for the existing model simulation.

longer geometrical, therefore it is by definition either equal or smaller than the geometrical sky view factor. The shading factor and the new sky view factor result in the irradiance using the ray casting model to be equal to or smaller than the existing method. The sky view factor of the PV module is found by the method explained in chapter 5.

For the ray casting model, the same models for the direct component and the diffuse component have been used as was given in section 8.2. The reason is to make sure that the two models are similar except for the environment and albedo component.

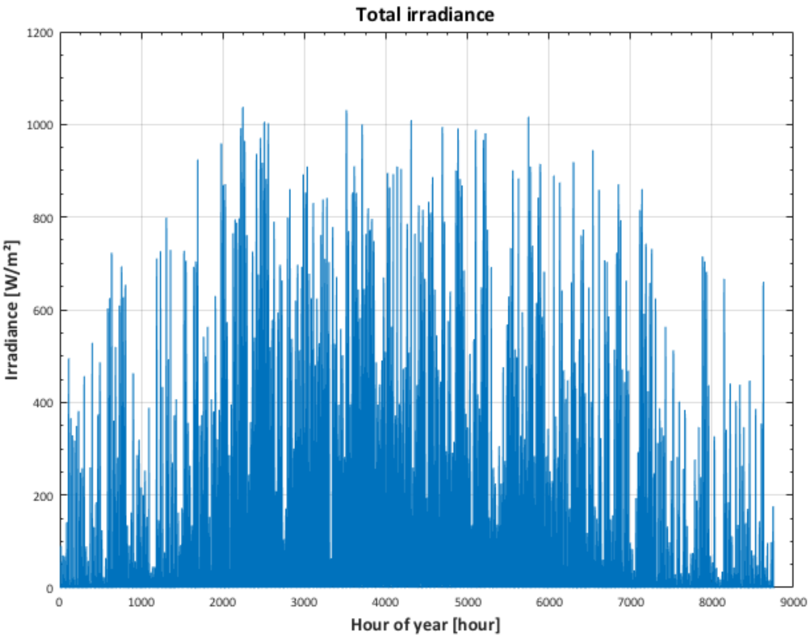

Figure 8.5: The total irradiance per hour of a year for the existing model simulation.

8.3.1. Albedo component using the ray casting model

In order to obtain the albedo component of the irradiance, many steps have to be taken. First, all the surfaces visible to the PV module are identified. This is done by sending out 500000 rays in all directions. If a ray hits a terrain, a 2 meter by 2 meter surface is placed on that exact location. Such a surface will be referred to as a ”hitpoint surface”. In order to keep the amount of hitpoint surfaces to a minimum, after 30 meters of distance from the PV module, the size of the hitpoint surface is increased depending on the distance. This is done by multiplying both the width and the height of the hitpoint surface by $2\frac{distance}{30}$. This eventually reduces the simulation time. The hitpoint surfaces with a greater distance to the PV module have a lesser impact on the albedo component of the irradiance and therefore it is less important to make them bigger. In the most ideal case, differential hitpoint surfaces should be used to obtain the most accurate results, however, with the current computational power this is not yet possible. Still, however, 2000 hitpoint surfaces are not unusual. The surfaces visible to the PV module have been made red in figures 8.6 and 8.7.

Next, another 500000 rays are sent out in all directions. Each ray that hits a hitpoint surface is counted for that specific surface according to lambert’s cosine law as was explained in chapter 6. This reduces the weight of the hit if the ray has been cast in an angle from the normal of the PV module. This ensures that a surface that is right in front of the PV module is much more significant than a surface that is on a great angle from the normal of the PV module. As an example, one hitpoint surface may be hit 1000 times, while another hitpoint surface may be hit just 1 time. In this way, a different number of hits are counted for each hitpoint surface. It should be noted that no hit is counted twice.

After the last ray has been sent, the view factor is calculated for each of the hitpoint surfaces. This is done by using equation 6.17, which was found in chapter 6 to be the view factor of a differential surface to a finite surface.

$$F_{di-j} = \frac{y}{x} = \frac{\sum_{i=1}^{i=n} y_i \cos\theta_i}{\sum_{j=1}^{j=m} x_j \cos\theta_j} \tag{8.4}$$

This gives the view factor from the PV module to each surface separately, however, for the albedo component, the view factor from each surface to the PV module is required. Instead of sending out 500000 rays for each of the surfaces to obtain the view factor from the hitpoint surface to the PV

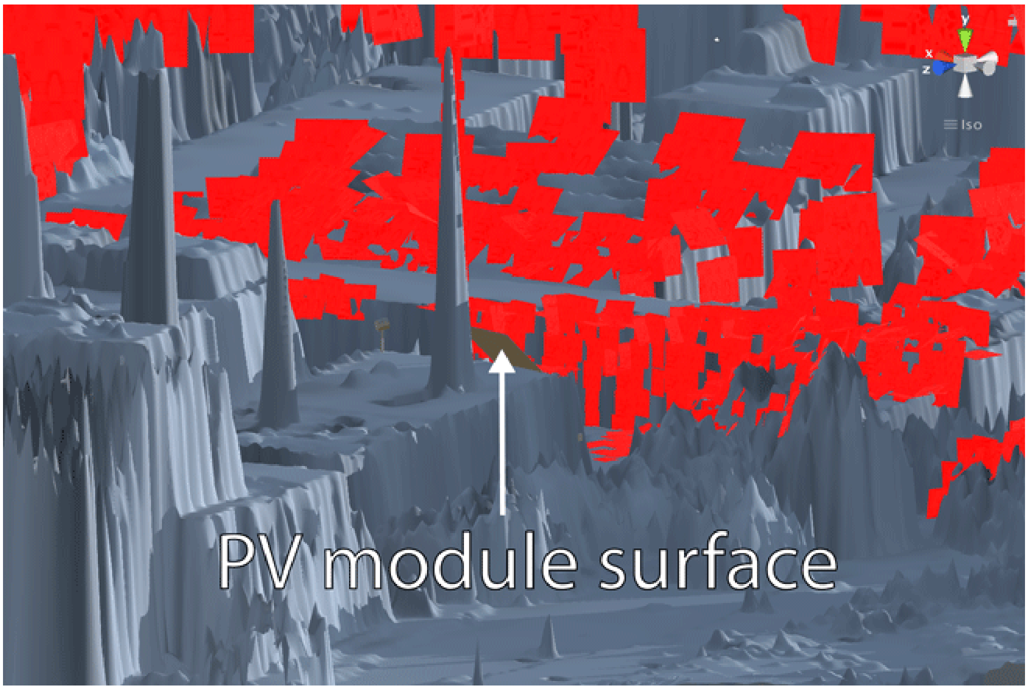

Figure 8.6: The surfaces visible to the PV module depicted by the red color with the PV module pointed by the arrow with latitude 51.999633 and longitude 4.368913 for the location.

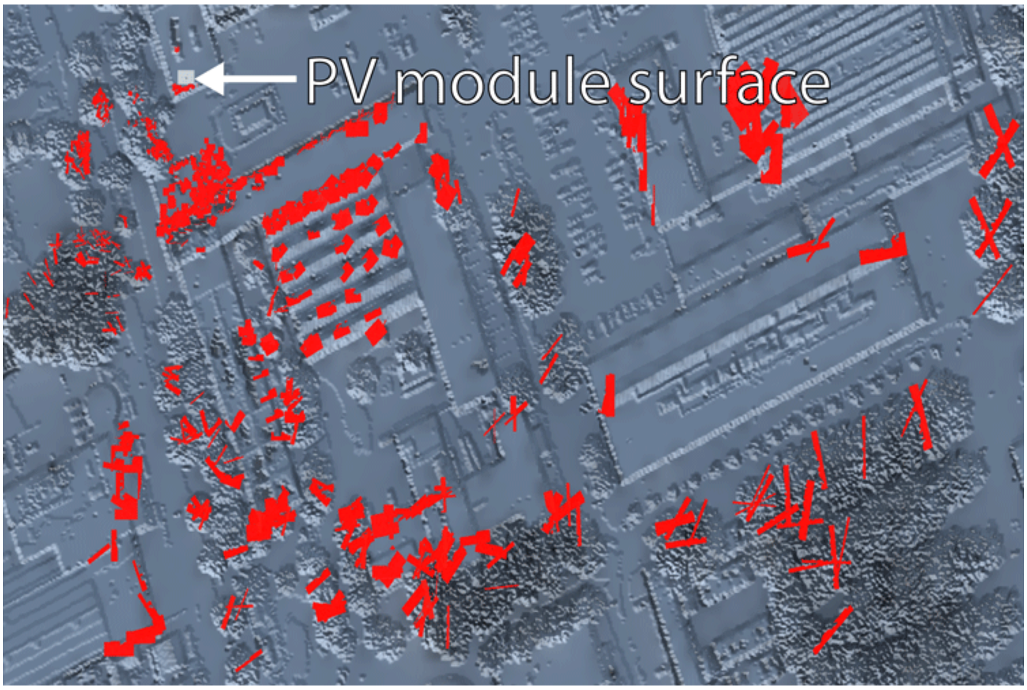

Figure 8.7: Top view of the surfaces visible to the PV module depicted by the red color with the PV module pointed by the arrow with latitude 51.999633 and longitude 4.368913 for the location.

module, the reciprocity rule of chapter 6 is applied.

$$F_{j-i} = F_{i-j}\frac{A_{PV}}{A_j} \tag{8.5}$$

This estimated simulation time that is saved by using the reciprocity rule is approximately 100 hours. For the reciprocity rule, the PV module is no longer regarded as a differential surface, but as a finite

surface with the area of the PV module. After using the reciprocity rule for each of the hitpoint surfaces, the view factor from each hitpoint surface to the PV module is now known. In other words, the fraction of radiated energy that leaves the hitpoint surface and received by the PV module is now known.
Now that the view factor is known, each of the hitpoint surfaces is treated in the same way as the PV module. First the sky view factor of each hitpoint surface is determined in the same way as is being done for the PV module. Next the shading factor is found by sending out rays in the direction of each of the hitpoint surfaces. In the same way as the PV module, if the ray does not reach the hitpoint surface, the shading factor for that hitpoint surface becomes 1 for that timestep. Using the same models as is being used for the PV module, the irradiance on the PV module is determined. The albedo factor determines the amount of irradiance that is reflected from the hitpoint surface, while the view factor determines the amount of reflected irradiance that reaches the PV module, resulting in equation 8.6.

$$G_M^{ground-n} = F_{HS-PV}\, \alpha\, \left(DNI\, \cos(AOI)\,(1-SF)\, +\, DHI\, SVF\right), \tag{8.6}$$

where F$_{HS-PV}$ is the view factor of a hitpoint surface HS to the PV module PV. Next to the view factor, the hitpoint surface specific variables are the albedo, AOI, SF and the SVF. The DNI and the DHI are assumed to be equal for all hitpoint surfaces. Equation 8.6 is the reflected irradiance on the PV module of a single hitpoint surface. The total reflected irradiance is consequently given by equation 8.7.

$$G_M^{ground} = \sum_{n=1}^{n=i} F_{HS_n-PV}\, \alpha_n\, \left(DNI\, \cos(AOI_n)\,(1-SF_n)\, +\, DHI\, SVF_n\right), \tag{8.7}$$

where n is the nth hitpoint surface of a total of i hitpoint surfaces.

8.3.2. Irradiance prediction using the ray casting model results

Again, the irradiance for each time step has been determined for a tilted surface in Delft using the same meteorological data and variables, but this time using the ray casting model. The hourly irradiance on a surface has been determined for each of the three components of irradiance. The hourly direct irradiance G_M^{dir} on a surface can be seen in figure 8.8.

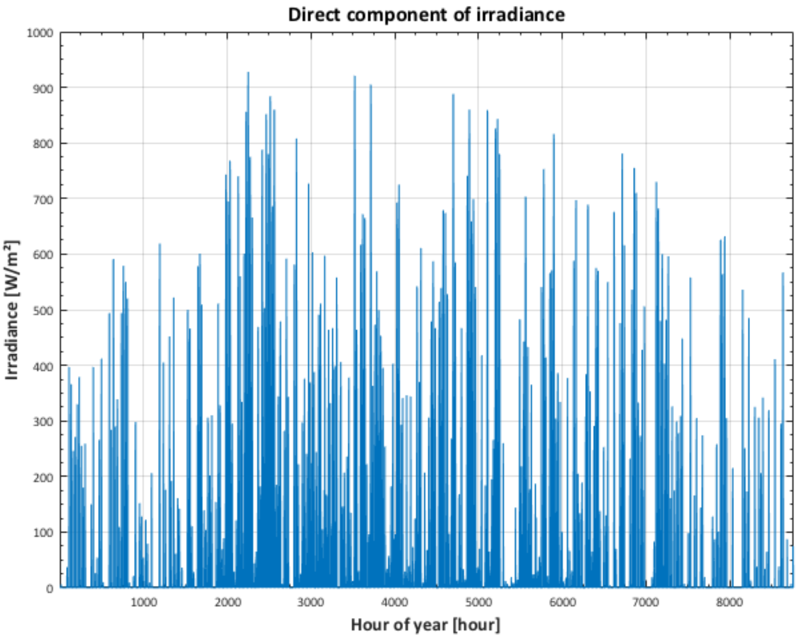

Figure 8.8: The direct irradiance per hour of a year for the ray casting model simulation.

The direct component has became even more unpredictable, since it is now dependant on the environment surrounding the PV module, since it can now be blocked by buildings as well, however, it

is still the most significant one with an annual energy yield of $524kWh/m^2$.
The diffuse irradiance, while being different in nature is now almost equally significant to the direct component. The hourly diffuse irradiance G_M^{dif} on a surface can be seen in figure 8.9.

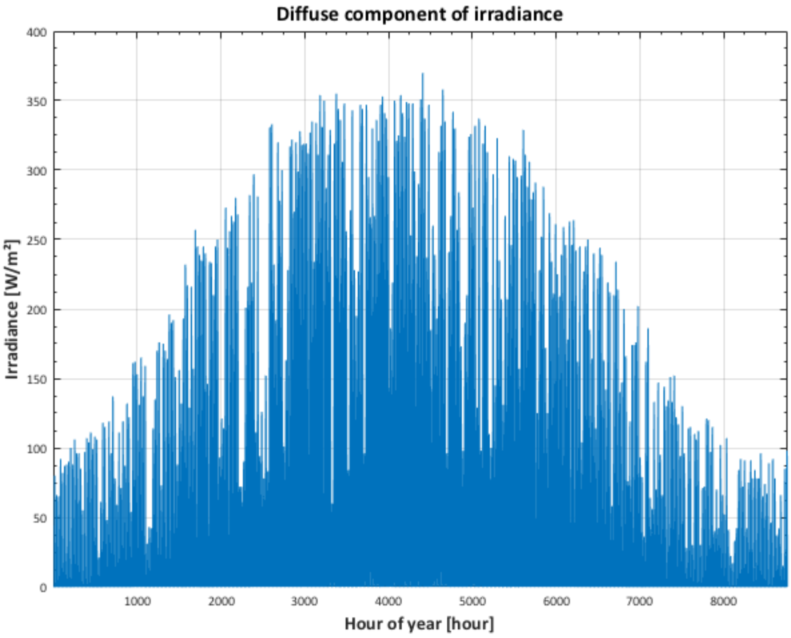

Figure 8.9: The diffuse irradiance per hour of a year for the ray casting model simulation.

The diffuse component of the simulation is only affected by the sky view factor. The sky view factor of the PV module in the simulation has been found to be 0.8326, which is almost the geometrical sky view factor of a 45 degrees tilted surface, which is 0.8535. This means that the PV module in the simulation has nearly no obstruction due to buildings or other objects. The only thing that has a significant impact on the sky view factor is the PV module itself. The estimated annual energy yield as a consequence of the diffuse component is $495kWh/m^2$.
The hourly reflected irradiance G_M^{ground} on a surface found using the ray casting model can be seen in figure 8.10.

The estimated annual energy yield due to the reflected irradiance is a mere $17kWh/m^2$, which clearly is not very much compared to the other components of irradiances.
Finally, the total irradiance G_M on a surface found using the ray casting model can be seen in figure 8.11, where the total estimated annual energy yield is $1037kWh/m^2$.

8.3.3. Comparison between the ray casting model and the existing model

It is interesting to see that the diffuse component of the irradiance is the same for both models. This is however due to the location of the PV module in the simulation, which has been placed upon a roof with very little obstructions, causing the sky view factor to be nearly the same. The direct component, however, has been affected much more. The ray casting model estimates that the direct component will deliver $98kWh/m^2$ less energy than what the existing model estimates. The albedo component has been affected by the simulation as well. The ray casting model estimates that the reflected irradiance is $21kWh/m^2$ less than what the existing models estimate. In total, the difference in annual energy is $119kWh/m^2$, from which 17% is due to the decrease in the albedo component, while the remaining part is due to the decrease in the diffuse component. This makes it clear that the existing models to estimate the irradiance are too optimistic.

8.3.4. Effect of albedo component on the irradiance

As was mentioned before, the albedo component has a 3.28% share in the total annual energy yield estimated by the existing model, which is not very much. It becomes even less according to the ray

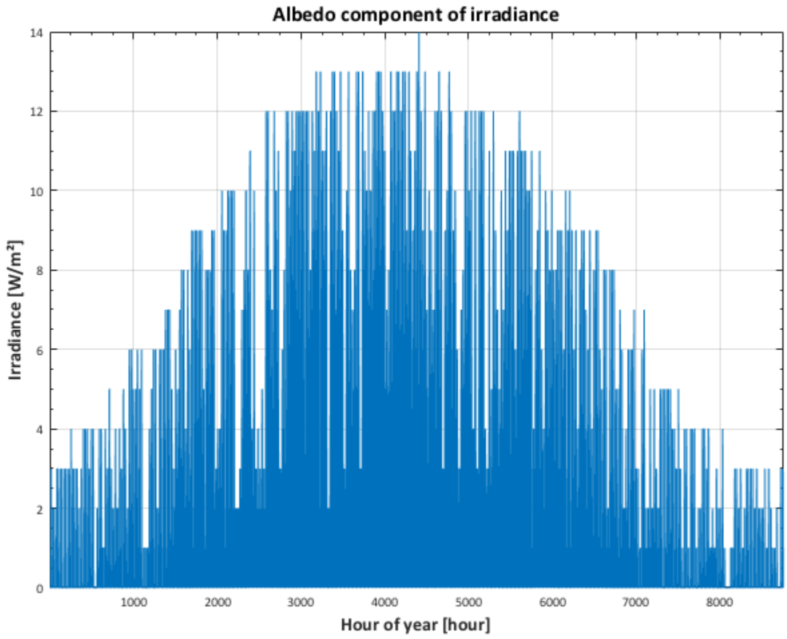

Figure 8.10: The reflected irradiance per hour of a year for the ray casting model simulation.

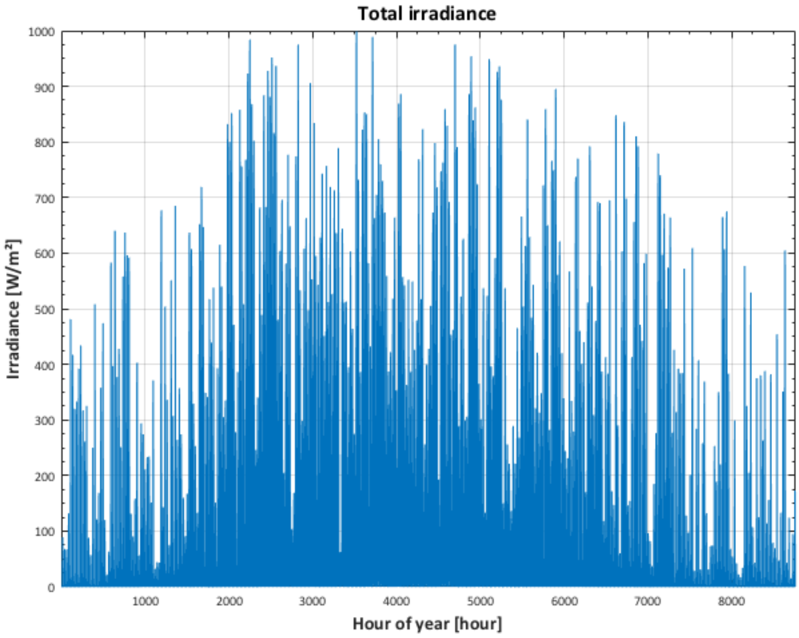

Figure 8.11: The total irradiance per hour of a year for the ray casting model simulation.

casting model, claiming a 1.65% share of the total annual energy yield. However, these simulations have been run for a 45 degrees tilted surface, which is not the optimal tilt for maximizing the reflected irradiance as has been discussed in chapter 3. Figure 8.12 shows the share of the albedo component of the total energy yield for different surface tilts at the studied location.

Clearly a large tilt results in a higher share of the albedo component. This is due to the view factors of the hitpoint surfaces to the PV module surface becoming higher for most of the surfaces. Also notable is the increase in the share of the albedo component for a 0 degrees tilt with respect to

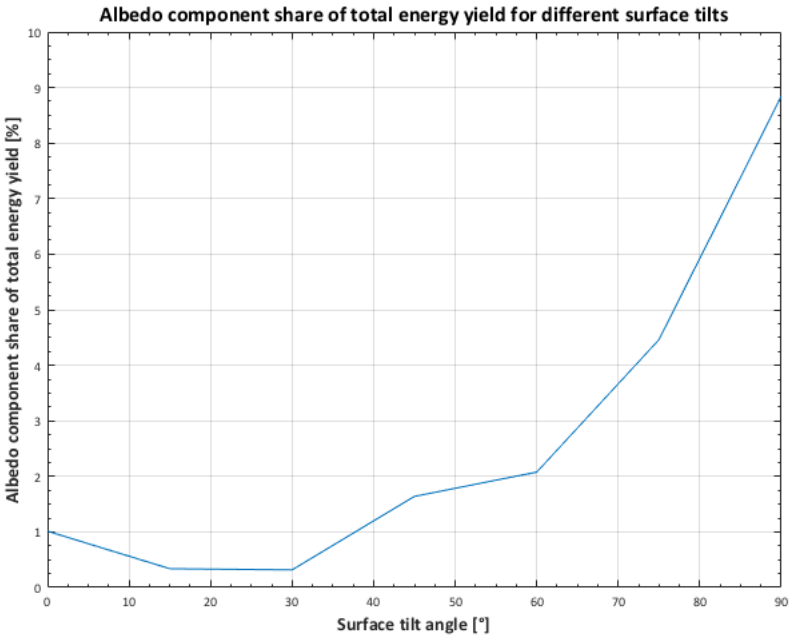

Figure 8.12: Albedo component share of total energy yield for different surface tilts.

the 20 degrees and even the 30 degrees tilt. This is due to the reflected irradiance from the surfaces behind the PV module, which for larger tilt angles were not visible. In chapter 3 it was discussed that for certain scenario's an albedo component with a 10% share of the total annual energy yield or more could be achieved. The 8.85% share that has been achieved using the ray casting model is very close to the mentioned 10%. The effect of the albedo factor on the share of the albedo component seems to be linear according to figure 8.13.

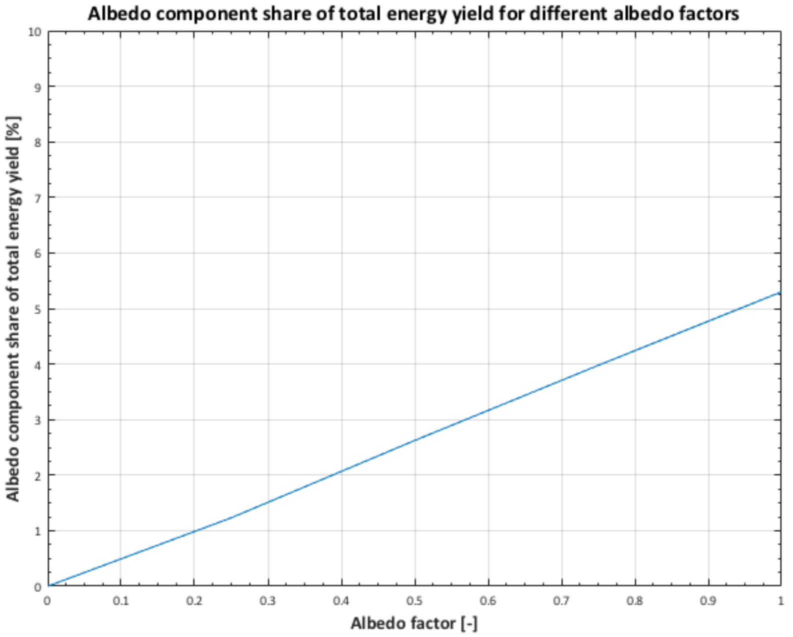

Figure 8.13: Albedo component share of total energy yield for different albedo factors.

If an albedo factor of 0.82 which is the albedo of fresh snow was used instead of 0.25(which is the albedo factor of concrete according to table 3.4, the share of the reflected irradiance would therefore increase by a factor of 3.28. This increase would make the albedo component of the irradiance even more significant. This is especially effective for locations which experience a lot of snow during the year. Also it proves that it is sensible to use a high albedo paint or other materials to increase the overall albedo factor of the surroundings.

8.4. Bifacial PV modules

In chapter 3 it was claimed that the reflected irradiance is mainly influential for bifacial PV modules. Bifacial PV modules are able to take in light from both the front and the back side, effectively increasing the yield of a single PV module. Logically, it is not possible to have both the front and the backside facing the Sun. It is therefore important to fix the module in such a way that both the front and the backside are utilized in a way that is beneficial for the total energy yield.

8.4.1. Different configurations

There are different ways of placing a bifacial PV module. One of the ways in which bifacial PV modules can be placed is simple in the exact same way as a normal PV module would be placed. For commercial uses, the PV module is then mounted closely onto a roof, leaving a small gap for the backside of the PV module. This means that only the light which is not absorbed and passes through the PV module has a chance of irradiating the backside of the bifacial PV module. This light can then be reflected by the roof and irradiate the backside of the bifacial PV module.

Another way of mounting a bifacial module is by mounting it a bit higher from the surface on which it is attached. This way, the backside of the bifacial PV module will have a wider view of the reflecting surfaces, therefore more light will irradiate the back side. Such a configuration can be seen in figure 8.14.

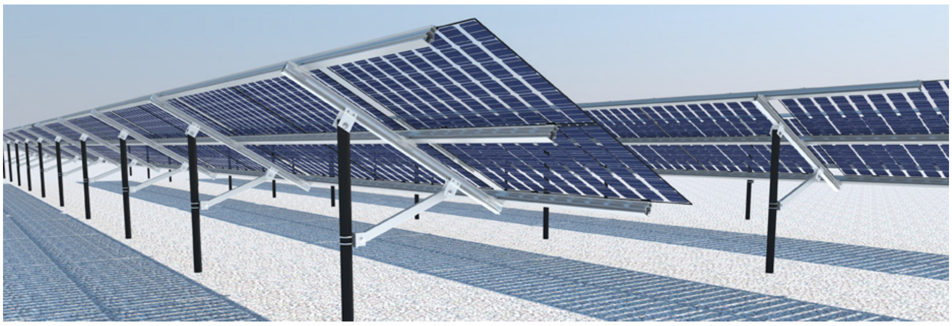

Figure 8.14: Bifacial PV modules mounted on a certain height above the ground [17].

A bifacial PV module may also be mounted in a vertical configuration. This is mainly useful in desert locations. In those locations the PV modules are heavily influenced by soiling, which means that particles stick on the PV module and consequently block the light. By putting the PV modules vertically, the particles are less likely to stick on the PV module and therefore the PV modules will require less cleaning. These PV modules may either be mounted in a way that the front side will be facing the equator or they may be mounted in an east-west configuration. A vertically mounted bifacial PV module can be seen in figure 8.15.

For the simulation, the PV module has been placed such, that it faces south. Then, the irradiance on both the front and the back side of the bifacial PV module has been estimated for different tilt angles. The visible surfaces to the back side of the PV module are depicted in red and can be seen in figure 8.16.

The share of the albedo component per tilt angle on the back side of the PV module can be seen in figure 8.17.

Logically, when the PV module has a tilt angle of 0 degrees, the PV module is flat, therefore, no irradiance due to the direct component or the diffuse component reaches the back side of the PV module. When increasing the tilt of the PV module, some direct irradiance as well as diffuse irradiance is able to reach the back side of the PV module, therefore reducing the share of the albedo component on the back side of the bifacial PV module. Also, the albedo component of the irradiance reduces in

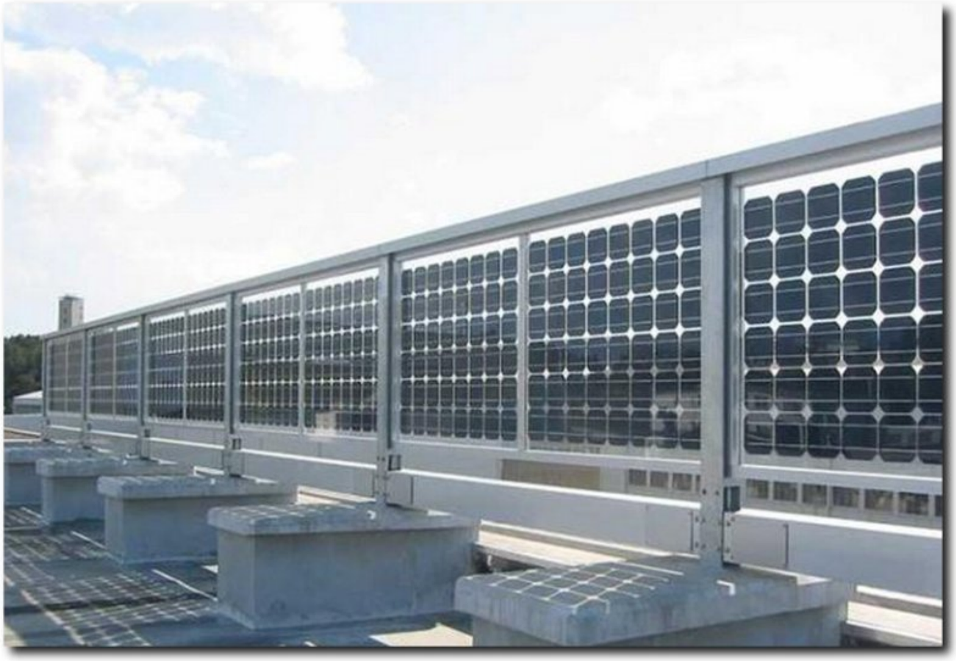

Figure 8.15: Vertically mounted bifacial PV modules [18].

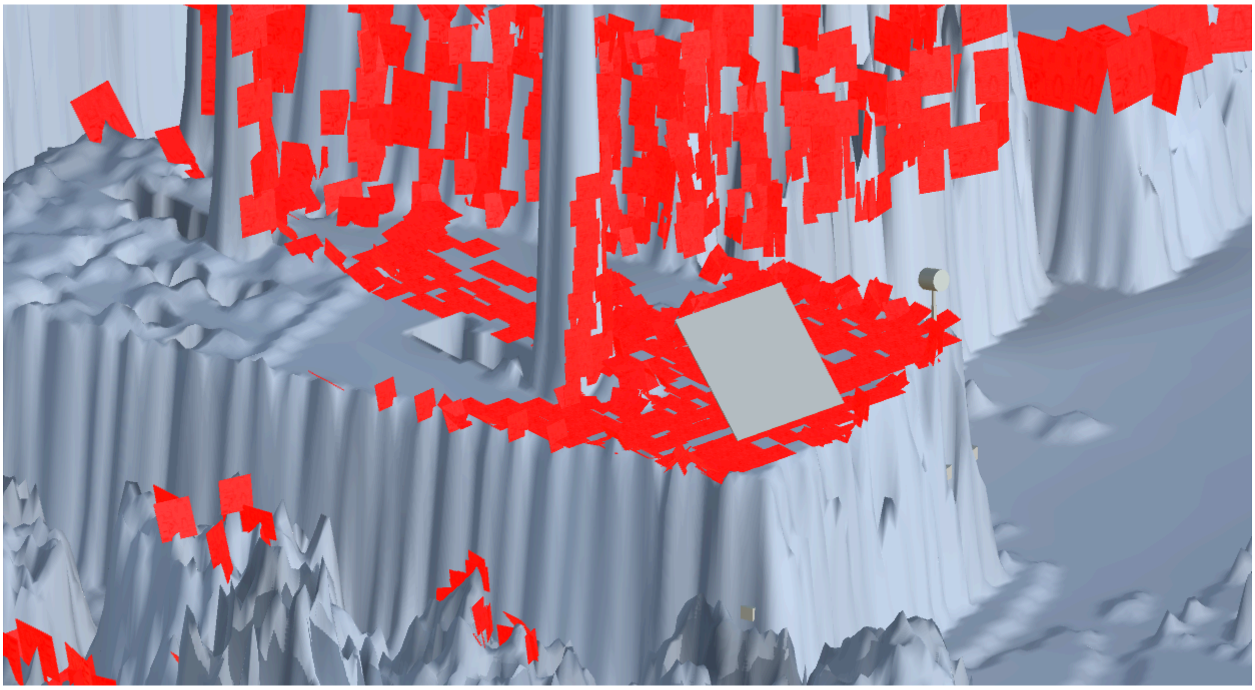

Figure 8.16: The visible surfaces to the backside of the bifacial PV module depicted in a red color.

total as the tilt angle increases. This can be seen in figure 8.18.

Clearly, at 0 degrees tilt angle, all of the total energy yield is made up of the reflected energy. At 90 degrees tilt angle, however, still a large portion of the energy yield is due to the reflected irradiance even for an albedo factor of 0.25. It is therefore important to keep the albedo factor as high as possible for bifacial modules.

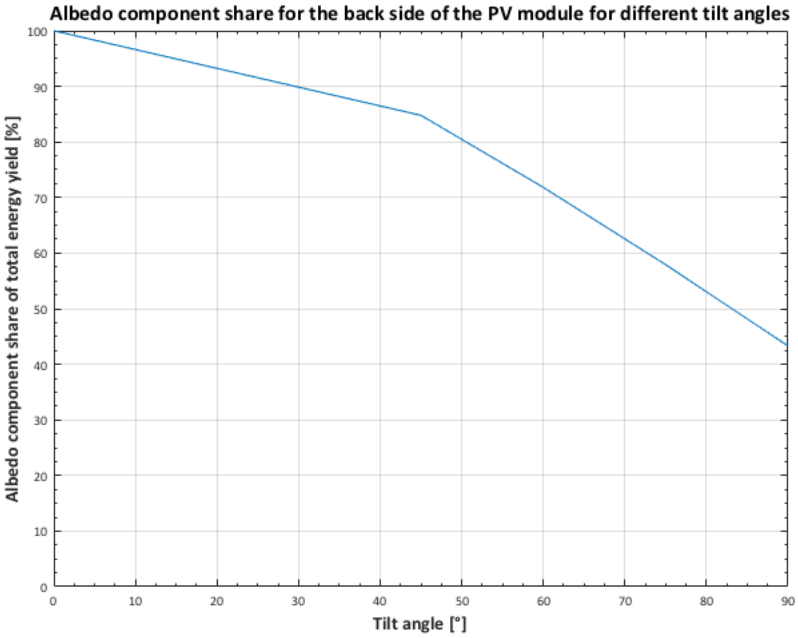

Figure 8.17: Albedo component share of total energy yield for the backside of a PV module for different tilt angles.

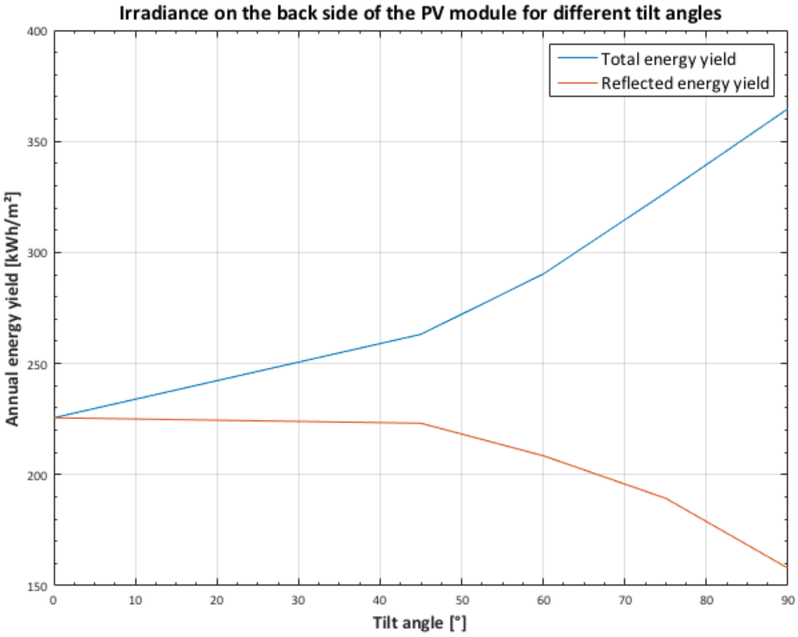

Figure 8.18: Reflected energy yield and the total energy yield on the backside of a PV module for different tilt angles.

8.4.2. Comparison between bifacial module and a monofacial PV module

According to Shoukry et al. [50], the gain in energy yield due to using a bifacial module instead of a monofacial module is up to 44%, while the gain in energy yield due to solar trackers is up to 18%. This increase is estimated using an albedo factor of 0.5 for a location in Uganda. For countries that are located more to the North, the bifacial gain may be even higher. This is due to the increase in albedo component share and the reliability of a bifacial module on the albedo component.
Simulations using the ray casting model show that the bifacial gain is up to 39% using an albedo factor

of just 0.25 and the gain in energy yield is even up to 56% for an albedo factor of 0.5. It should be noted that the bifacial gain does not double for the albedo factor which is 2 times greater, because the diffuse component and direct component do not change for a change in the albedo factor. Results of the gain in energy yield due to using a bifacial PV module instead of a monofacial PV module can be seen for different tilt angles in figure 8.19.

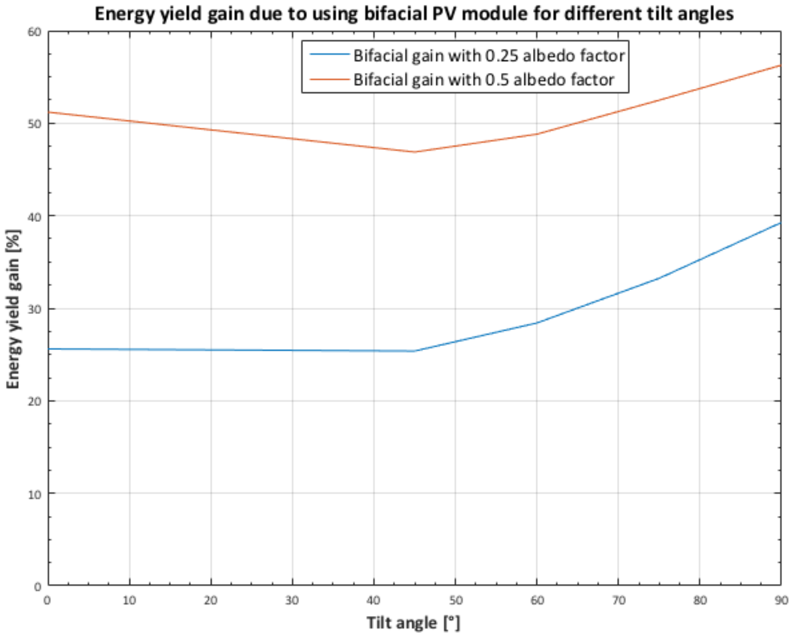

Figure 8.19: Bifacial gain for different albedo factors and different tilt angles.

It becomes clear that the largest bifacial gain is achieved for a PV module tilted with an angle of 90 degrees. However, this does not mean that a tilt angle of 90 degrees does also always result in the largest absolute energy yield. The energy yield of the front side, back side and both sides have been estimated for different tilt angles and can be seen in figure 8.21.

It seems that the maximum energy yield of a bifacial module for the factors used in the simulation are achieved for a tilt angle of approximately 60 degrees. When the albedo factor changes, so does the optimal tilt angle. According to figure 8.21, the optimal tilt angle for the maximum total annual energy of a bifacial PV module is now 45 degrees at the studied location.

8.5. Conclusions

The existing models will mostly be more optimistic in terms of energy yield since the sky view factor does not include the buildings or other obstacles in the surroundings. There are ways of including the environmental factors, but those often require field work. Also, the shading factor is not taken into account, causing the direct component to be only influenced by the angle of incidence. There are also models which do take the environmental factors into account using LiDAR or other means, but these models either do not take the albedo component into account at all or they do not take the environmental factors into account. This thesis eliminates that problem by using LiDAR data to map the surroundings using hitpoint surfaces. For each of those surfaces the irradiance is estimated separately. Along with the amount that is reflected and the view factor the albedo component of the irradiance is then determined. The results obtained by this model are very promising and are very much in line with what literature has claimed that the share of the albedo component of the irradiance can be. Also, this model is able to determine the optimal tilt angle of a PV module including the albedo component of the irradiance.

Even more importantly, this model is also useful for bifacial modules since it is able to estimate the irradiance on the back side of a PV module. The energy yield incident on the back side of a PV module is also in line with the claims of previously published literature. This model is able to easily determine the

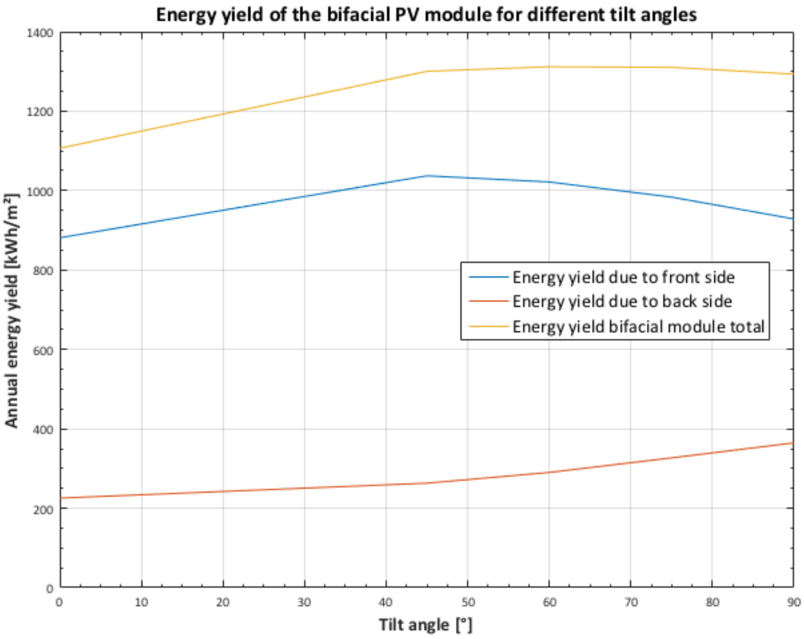

Figure 8.20: Energy yield of the front side, back side and both sides of a bifacial module for different tilt angles.

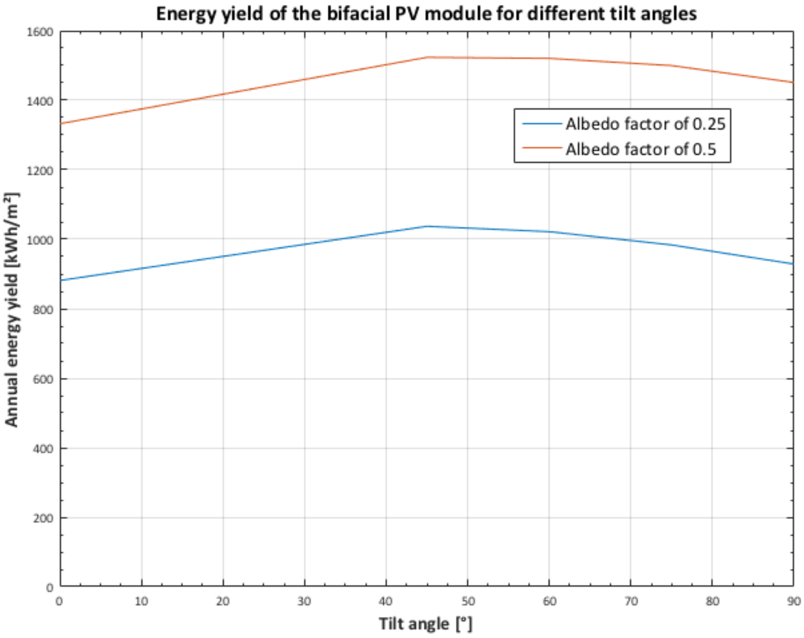

Figure 8.21: Energy yield of the bifacial PV module for different albedo factors and different tilt angles.

optimal tilt angle of a bifacial PV module which is different from a monofacial PV module. Furthermore, this model shows that the optimal tilt angle of a PV model changes with respect to the albedo of the environment.

9

Conclusions

In this thesis, the research done in order to create a model which is able to estimate the annual energy yield incident on of a monofacial and bifacial PV modules has been presented. Using LiDAR data allows for a location specific simulation, with custom sky view factors, view factors and shading factors, which are all determined using ray casting. Also along with the simulation framework, Unity 3D, it allows the user to rapidly change and see the environment along with the PV system to be placed in a three-dimensional view. Through this study, the three research questions proposed in chapter 1 have been addressed. The questions and the corresponding answers are concluded below:

What are the parameters which have an effect on the albedo factor?

After going through several existing models of irradiance prediction, the albedo has been thoroughly handled. Several measurements were done in order to determine the albedo of different materials, after which could be concluded that the albedo is constantly changing with respect to time, location and weather conditions. The measurements showed that a change in global horizontal irradiance, view factor, the type of irradiance and of course the reflecting surface material will result in a change in albedo. The spectral reflectivity along with the spectral irradiance has been introduced which has the potential of explaining the albedo. The spectral irradiance can be divided into the spectral direct irradiance as well as the spectral diffuse irradiance. The spectral direct irradiance changes with respect to the air mass, which can be found accurately. The diffuse component however is more unpredictable, since it is not always clear how it behaves. In this way the first research question has been answered. Currently a publication which has the aim to model the albedo in an accurate way is in progress. The albedo model also has the goal to eliminate the need of field work which will save much time and allows the determination of albedo for any location. The draft of this paper can be found in appendix D.
Another important conclusion on the albedo is that measuring the albedo on a certain location will only give the albedo of that specific location for that exact time and weather conditions. If one one the parameters differs, the albedo will become different. The albedo should therefore not be used as a parameter which describes the reflected irradiance of a location. The albedo should be used on specific surfaces, for which the entire surface has the same exact parameters. This means that the whole surface should have the same irradiances, shading factors, sky view factors etc. When using a large surface, this will of course not be true since one corner of a surface will likely have another sky view factor as an example. Therefore, the simulation should use as small surfaces as possible.

How can the albedo component of the irradiance be estimated using the environmental factors without the need of field work?

LiDAR data was used in order to determine the albedo component of the irradiance, because LiDAR allows for the simulation framework to create the three-dimensional environment of the location that is being studied. This 3 dimensional environment consists of all the surfaces that reflect light to the PV module. This reflected light is the albedo component. In order to determine this, first the sky view factor should be known, because each of those surfaces will have diffuse light irradiating on them. The albedo has been discussed in the chapter before and for this simulation, even though it has been concluded that the albedo changes with respect to many variables, a constant albedo was used. Since each of the surfaces consist of their own variables, the albedo can be a variable that changes with respect to the material of that surface and by means of time, irradiance and other potential variables which influence the albedo. Also, the shading factor and angle of incidence on each of those surfaces must be known, for which the sun path has been used. Now that the total irradiance on the surfaces is known along with the fraction of that irradiance that is reflected from each of those surfaces, all that is left is to know the amount of reflected irradiance that reaches the PV module. For this, the view factor is introduced, which is the fraction of radiation leaving each of the reflecting surfaces, that is intercepted by the PV module. The view factor is determined very accurately using ray casting and equation 9.1, which is explained in thoroughly in chapter 6.

$$F_{di-j} = \frac{y}{x} = \frac{\sum_{i=1}^{i=n} y_i \cos\theta_i}{\sum_{j=1}^{j=m} x_j \cos\theta_j} \tag{9.1}$$

All of these ingredients result in equation 9.2 for the albedo component of the irradiance, which is explained in detail in chapter 8.

$$G_M^{ground} = \sum_{n=1}^{n=i} F_{HS_n-PV}\, \alpha_n \; (DNI \; \cos(AOI_n)\,(1 - SF_n) \; + \; DHI\, SVF_n) \tag{9.2}$$

This results in the answer for the second research question.

How can the irradiance on the back side of a bifacial PV module be estimated?

The irradiance on the front side of a bifacial PV module is determined in the same way as the irradiance on the front side of a monofacial PV module. The back side, however, does not ”see” the same as the front side of the PV module. Therefore, all of the variables found for the front side of the PV module do not hold anymore. For this reason, the same exact steps are performed for the front side of the PV module. This means that the sky view factor of the back side of the bifacial PV module is determined, the view factors from the surfaces to the back side of the monofacial PV module (which is a new set of surfaces), the shading factor and the angle of incidence for the bifacial PV module as well as for all the new set of surfaces is determined. Then simply by using the same meteorological data as was used for the front side, the irradiance on the back side of a bifacial PV module is determined, resulting in the answer of the last research question. Now simply by adding the irradiance on the front and the back side of a bifacial PV module, the total irradiance is determined.

Bifacial gain and optimal tilt angle

From the results of the simulation and other literature it seems that the bifacial gain is up to 39% for an albedo of 0.25 and the optimal tilt angle of 60 degrees for that specific case. The optimal tilt angle proves to change with respect to the albedo of the surroundings, which is 45 degrees for an albedo of 0.5 and otherwise the same exact parameters. The maximum total gained energy yield is then found for a tilt angle of 60 degrees.

For another location, other optimal tilt angles might be found. It is therefore important to always simulate when changing a location, because it is hard to predict how the environment will change.

9.1. Recommendations

In this section, several recommendations will be given which may improve the model in different ways.

Spectral albedo

In this thesis, the spectral albedo was introduced, but it was not used as there is still research being done on this subject. The authors of the paper of appendix D are currently working on an albedo model which should describe the albedo of a material for any time and any weather conditions. This model can then be plugged into equation 9.2 to describe the albedo component in a more accurate way. Also research is being done by Readaar, which is one of the members of the PVISION project of which this thesis also is a part of, in order to determine materials of the surroundings using aerial imagery. Combining that technology with the model proposed in this thesis will allow for a fully automated estimation of the albedo component of the irradiance. This will then be usable to determine the irradiance on the back side of a bifacial PV module as well.

Spectral irradiance

Next to the spectral albedo, instead of the irradiance, the spectral irradiance should become the standard in which meteorologists record the solar power. Different PV technologies have different EQE spectra, thus different PV technologies have their own desired spectral irradiances. Since the spectral irradiance changes with respect to air mass, the weather conditions as well as the surrounding reflecting materials, a different PV technology could be optimal for location x as compared to location y. By selecting the PV technologies based on the spectrum that will be irradiating on them, higher efficiencies will be achieved. The air mass and the weather conditions are factors which cannot be easily changed, however, the reflecting materials surrounding the location of the potential PV module can be changed. As was concluded in chapter 3, choosing the right reflecting surface material can increase the output power by 7.5%.

Simulation time

One of the largest drawbacks of this model is the large simulation time that it takes in order to determine the annual energy yield on a surface. In order to increase the speed of the simulation, multi-core processing should be used. Multi-core processing is used to run a set of computer code by multiple processor cores simultaneously. This way, the simulation time steps could be divided between the different processor cores and added together in a later stage in the simulation. If there are 2 computer cores as an example, core 1 could be assigned to estimate the irradiance for the first half of the year, while the second core is assigned to estimate the irradiance for the second half of the year. The work could be divided even more if more processing cores would be used. This would reduce the simulation time potentially in the order of magnitudes depending on the amount of cores used. By doing so, the simulation could be improved by using even smaller hitpoint surfaces to divide the geometry into smaller areas, potentially approaching differential areas. This would make the simulation even more realistic.

Simulation time steps

In chapter 7, the importance of simulation time steps was expressed. Another way of improving the simulation is to use meteorological data with smaller time steps, since that is the factor that limits the time steps. As a consequence, this would of course increase the simulation time by the factor in which the simulation time steps have been reduced. However, if this would be combined with multi-core processing, this might potentially not become an issue in the future.

More accurate direct and diffuse irradiance models

For the prediction of the irradiance, the simplest direct and diffuse models have been used, because it was not in the scope of this thesis to determine which model performs the best. This model has been designed in such a way that it can be altered easily to be applicable for other direct and diffuse irradiance models. It is recommended, therefore, that more realistic direct and diffuse models are used in the future.

Validation with real life data

The simulation results have been checked with other literature and it complied with their results. However, it would be more effective if the model could be tested using real life data, since it would increase the reliability and reproduce-ability of the simulation. Measurements encompassing several hours, several days or even a year could be done, from which the latter is preferred. These measurements should measure the irradiance on a tilted surface, for which a simulation should be built in the same exact setting, for the same exact location. In order to have the same input, the same GHI, DHI, DNI and albedo as was measured during the measurements should be used for the simulation.

Bibliography

[1] ITRPV, *International technology roadmap for photovoltaic,* (2017).

[2] M. A. Green, *Solar cells : operating principles, technology, and system applications / Martin A. Green* (Prentice-Hall Englewood Cliffs, N.J, 1982) pp. xiv, 274 p.

[3] Meteonorm, *Irradiation data for every place on earth,* (2017), [Online; accessed 4-October-2017].

[4] A. Smets, K. Jager, O. Isabella, R. van Swaaij, and M. Zeman, *Solar energy - the physics and engineering of photovoltaic conversion, technologies and systems* (UIT Cambridge Ltd., 2016).

[5] J. S. Stein, *Poa sky diffuse,* (2012), [Online; accessed 4-Oktober-2017].

[6] S. Wang, *Pavement albedo assessment: methods, aspects, and implication,* (2015).

[7] Y. Kotak, M. Gul, T. Muneer, and S. Ivanova, *Investigating the impact of ground albedo on the performance of pv systems,* (2015).

[8] A. Baldridge, S. Hook, C. Grove, and G. G. Rivera, *The aster spectral library version 2.0, Remote Sensing of Environment,* **113**, 711 (2009).

[9] C. Honsberg and S. Bowden, *Air mass,* (2014), [Online; accessed 4-October-2017].

[10] S. Gate, *Simple model of the atmospheric radiative transfer of sunshine (smarts),* (2013), [Online; accessed 20-November-2017].

[11] C. A. Gueymard, *The sun's total and spectral irradiance for solar energy applications and solar radiation models,* Solar Energy **76**, 423 (2004).

[12] M. Brennan, A. Abramase, R. Andrews, and J. Pearce, *Effects of spectral albedo on solar photovoltaic devices,* Solar Energy Materials and Solar Cells **124**, 111 (2014).

[13] Google, *Google maps,* (2017), [Online; accessed 23-September-2017].

[14] Meteonorm, *Horicatcher,* (2017), [Online; accessed 22-September-2017].

[15] educcess, *How longitude, latitude and gps location services works,* (2015), [Online; accessed 24-October-2017].

[16] Wikipedia, *Daytime,* (2017), [Online; accessed 28-October-2017].

[17] EGENERGY, *Bifacial pv systems,* (2017), [Online; accessed 26-November-2017].

[18] Electrosun, *Panneau photovoltaïque premium double face 245w,* (2017), [Online; accessed 26-November-2017].

[19] G. Gilchrist, *A simple method to determine surface albedo using digital photography,* (2011).

[20] M. Geem Van, *Albedo of concrete and select other materials,* (2014).

[21] Motivaction, *Zonnepanelen goedkoper dan stroom,* (2012), [Online; accessed 26-November-2017].

[22] T. Energy, *Photovoltaic systems installation optimization,* (2016), [Online; accessed 27-November-2017].

[23] F. Kasten and A. T. Young, *Revised optical air mass tables and approximation formula,* Appl. Opt. **28**, 4735 (1989).

[24] E. Laue, *The measurement of solar spectral irradiance at different terrestrial elevations,* Solar Energy **13**, 43 (1970).

[25] C. Rigollier, O. Bauer, and L. Wald, *On the clear sky model of the esra — european solar radiation atlas — with respect to the heliosat method,* Solar Energy **68**, 33 (2000).

[26] KNMI, *Uurgegevens van het weer in nederland,* (2017), [Online; accessed 4-October-2017].

[27] F. Kasten, W. Palz, H. Golchert, J. Greif, C. Communities, R. Dogniaux, M. Lemoine, J. Page, and K. Scharmer, *European Solar Radiation Atlas: Solar Radiation on Horizontal and Inclined Surfaces* (Springer Berlin Heidelberg, 2012).

[28] D. Reindl, W. Beckman, and J. Duffie, *Evaluation of hourly tilted surface radiation models,* Solar Energy **45**, 9 (1990).

[29] A. M. Noorian, I. Moradi, and G. A. Kamali, *Evaluation of 12 models to estimate hourly diffuse irradiation on inclined surfaces,* Renewable Energy **33**, 1406 (2008).

[30] P. Loutzenhiser, H. Manz, C. Felsmann, P. Strachan, T. Frank, and G. Maxwell, *Empirical validation of models to compute solar irradiance on inclined surfaces for building energy simulation,* Solar Energy **81**, 254 (2007).

[31] J. A Coakley, *Reflectance and albedo, surface, Encyclopedia of Atmospheric Sciences,* (2003).

[32] C. Gueymard, *From global horizontal to global tilted irradiance: How accurate are solar energy engineering predictions in practice?* (2008).

[33] P. Ineichen, O. Guisan, and R. Perez, *Ground-reflected radiation and albedo, Solar Energy,* **44**, 207 (1990).

[34] K. en Zonen, *Kipp en zonen,* (2017), [Online; accessed 17-November-2017].

[35] T. C. R. Russell, R. Saive, A. Augusto, S. G. Bowden, and H. A. Atwater, *The influence of spectral albedo on bifacial solar cells: A theoretical and experimental study,* IEEE Journal of Photovoltaics **7**, 1611 (2017).

[36] ESRI, *What is lidar data?* (2017), [Online; accessed 23-September-2017].

[37] PDOK, *Ahn3 downloads,* (2017), [Online; accessed 23-September-2017].

[38] C. S. B. Grimmond, S. K. Potter, H. N. Zutter, and C. Souch, *Rapid methods to estimate sky-view factors applied to urban areas,* International jourlan of climatology **21**, 903 (2001).

[39] E. Weisstein, *CRC Concise Encyclopedia of Mathematics, Second Edition* (CRC Press, 2002).

[40] E. B. Saff and K. A.B.J., *Distributing many points on a sphere,* The mathematical intelligencer **19**, 5 (1997).

[41] Á. González, *Measurement of areas on a sphere using fibonacci and latitude–longitude lattices,* Mathematical Geosciences **42**, 49 (2009).

[42] P. Boucher, *Points on a sphere,* (2006), [Online; accessed 23-September-2017].

[43] A. Mills, *Basic Heat and Mass Transfer* (Prentice Hall, 1999).

[44] L. Augusto, B. Giacomet, and N. Mendes, *Numerical method for calculating view factor between two surfaces, IBPSA 2007 - International Building Performance Simulation Association 2007,* , 269 (2007).

[45] M. Mirhosseini and A. Saboonchi, *View factor calculation using the monte carlo method for a 3d strip element to circular cylinder,* International Communications in Heat and Mass Transfer **38**, 821 (2011).

[46] B. T. F. Chung and P. S. Sumitra, *Radiation shape factors from plane point sources,* Heat Transfer **94**, 328 (1972).

[47] S. Juds, *Photoelectric Sensors and Controls: Selection and Application, First Edition*, Mechanical Engineering (Taylor & Francis, 1988).

[48] S. J. Hoff and K. A. Janni, *Monte carlo technique for the determination of thermal radiation shape factors,* American Society of Agricultural Enineers **32**, 1023 (1989).

[49] D. Hamilton and W. Morgan, *Radiant Interchange Configuration Factors*, NACA Technical Note 2836 (National Advisory Committee for Aeronautics, Washington, D.C., 1952).

[50] I. Shoukry, J. Libal, R. Kopecek, E. Wefringhaus, and J. Werner, *Modelling of bifacial gain for stand-alone and in-field installed bifacial pv modules,* Energy Procedia **92**, 600 (2016), proceedings of the 6th International Conference on Crystalline Silicon Photovoltaics (SiliconPV 2016).

Appendices

A

Meteonorm data

Svalbard/Longyear

Location name

78.25
Latitude [°N]

15.467
Longitude [°E]

10080
WMO

29
Altitude [m a.s.l.]

I, 2
Climate region

Standard
Radiation model

Standard
Temperature model

Perez
Tilt radiation model

2000–2009
Temperature period

1991–2010
Radiation period

Additional information

Uncertainty of yearly values: Gh = 6%, Bn = 11%, Ta = 0,3 °C
Trend of Gh / decade: -
Variability of Gh / year: 4,0%
Radiation interpolation locations: Barentsburg (35 km), Isfjord Radio, Sval (47 km), Ny-Aalesund (107 km), Ny-Aalesund (107 km)
G_Gh:; Mean irradiance of global radiation horizontal
PAR:; Photosynthetically active radiation
G_Dh:; Mean irradiance of diffuse radiation horizontal

Month	**Ta**	**G_Gh**	**Td**	**RH**	**G_Dh**	**FF**	**G_Lin**	**PP**
	[°C]	[W/m2]	[°C]	[%]	[W/m2]	[m/s]	[W/m2]	[hPa]
January	-10.4	0.0	-13.9	75.3	0.0	6.0	226	1010
February	-10.9	0.0	-14.5	74.4	0.0	5.9	222	1010
March	-13.7	30.5	-17.4	73.3	15.9	4.9	197	1009
April	-8.9	119.4	-12.8	72.8	51.4	4.8	212	1009
May	-1.9	201.7	-6.1	72.8	85.8	4.3	243	1009
June	3.7	209.8	-0.9	71.9	107.1	4.2	273	1010
July	7.2	164.2	2.9	74.0	105.6	4.5	296	1010
August	6.3	98.7	2.6	77.0	62.0	3.7	295	1010
September	1.7	40.3	-2.3	74.5	26.8	4.2	274	1009
October	-3.7	5.1	-7.5	74.7	4.1	5.1	249	1009
November	-6.2	0.0	-9.6	76.7	0.0	5.7	239	1010
December	-8.4	0.0	-11.8	76.4	0.0	5.9	228	1010
Year	-3.8	72.5	-7.6	74.5	38.4	4.9	246	1009

Month	Sd	N	TL	Bn	Ghmax	G_Gex	G_PAR	Snd
	[h]	[octas]	[ ]	[W/m2]	[W/m2]	[W/m2]	[W/m2]	[cm]
January	0	0	1.1	0.0	0	0	0.0	-999.0
February	6	0	1.1	0.0	1	2	0.0	-999.0
March	57	5	3.0	95.2	39	71	9.0	-999.0
April	105	4	2.5	259.6	151	233	45.3	-999.0
May	116	4	3.1	328.8	282	420	84.9	-999.0
June	105	5	2.8	255.5	351	507	91.5	-999.0
July	79	6	3.3	156.5	314	468	73.6	-999.0
August	70	6	2.7	127.3	200	311	44.9	-999.0
September	42	7	3.2	60.2	75	129	18.4	-999.0
October	15	6	2.5	10.3	9	18	2.4	-999.0
November	0	0	1.1	0.0	0	0	0.0	-999.0
December	0	0	1.1	0.0	0	0	0.0	-999.0
Year	595	4	2.3	108.3	119	180	30.8	0.0

Ta:	Air temperature
RH:	Relative humidity
Ta min:	10 y minimum (approx.)
Ta max:	10 y maximum (approx.)
Ta dmin:	Mean daily minimum Ta
Ta dmax:	Mean daily maximum Ta
SD:	Sunshine duration
RR:	Precipitation
RD:	Days with precipitation
FF:	Wind speed
SD astr.:	Sunshine duration, astronomic
DD:	Wind direction
Snd:	Snow depth

Monthly radiation

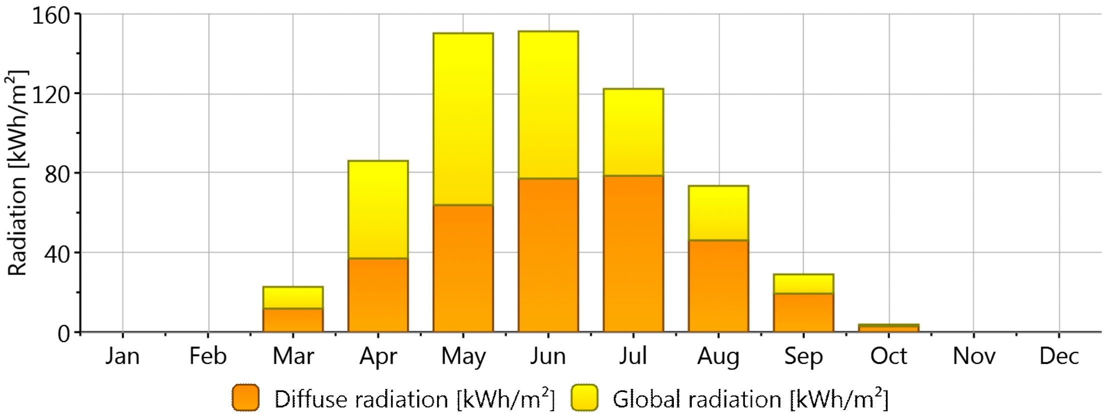

Daily global radiation

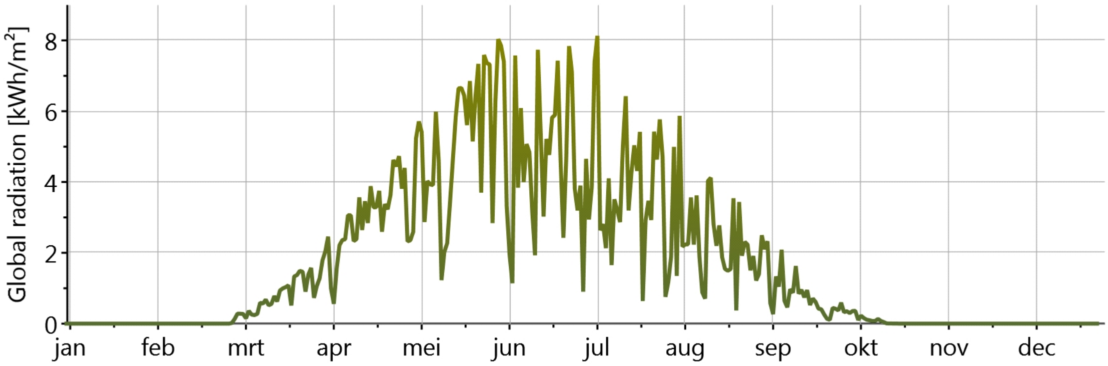

Monthly temperature

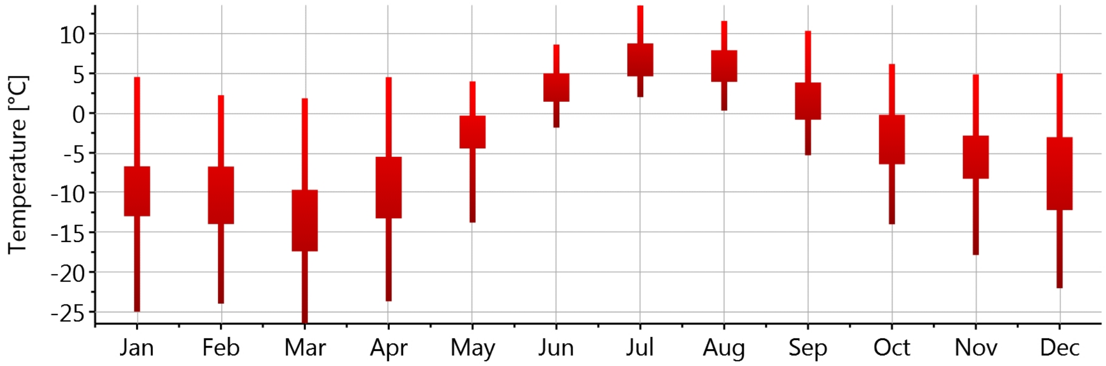

Daily temperature

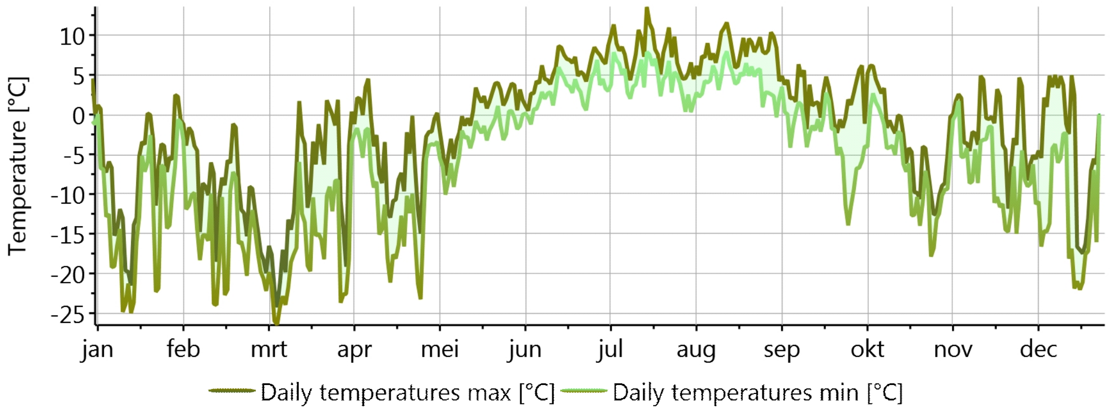

Precipitation

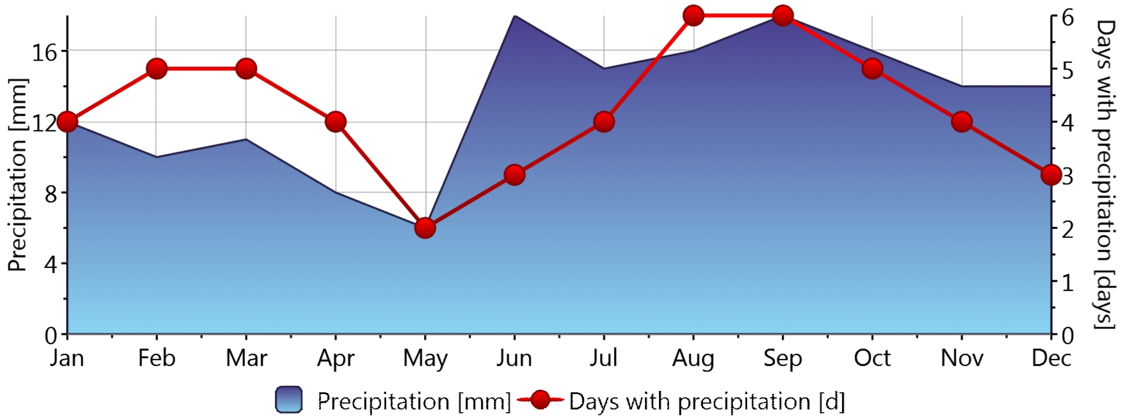

Sunshine duration

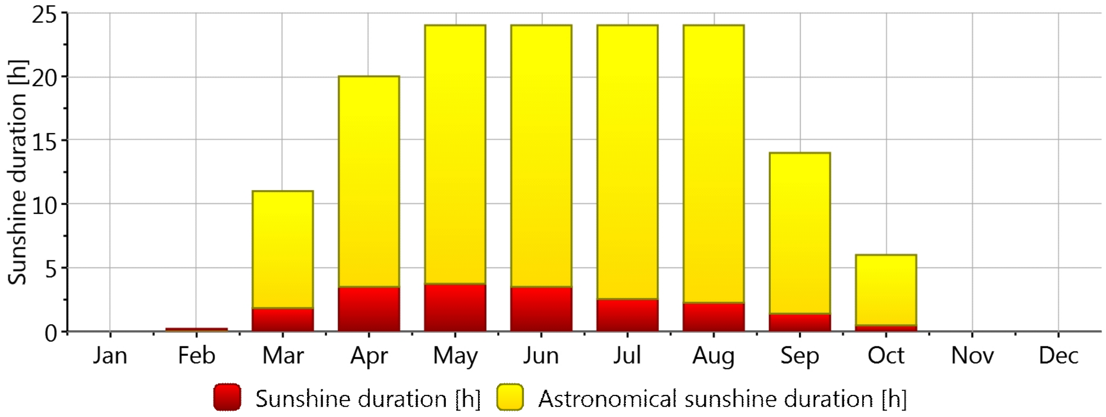

meteonorm

B

Albedometer

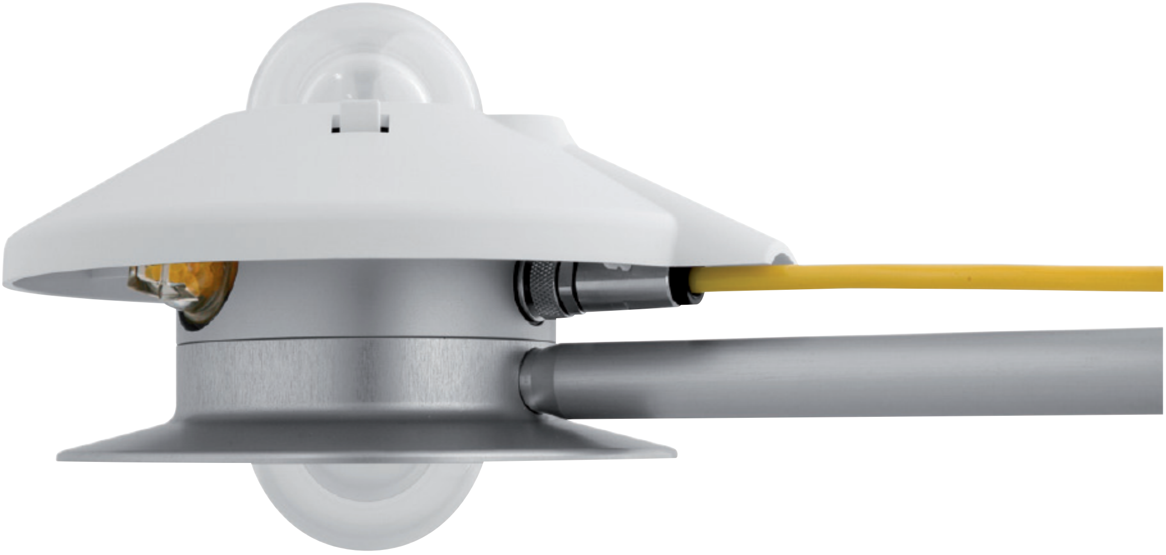

Albedometers

FOR THE PRECISE MEASUREMENT OF GLOBAL AND REFLECTED RADIATION

Specifications to ISO 9060:1990 and IEC 60904 standards
Measure incoming and reflected solar radiation with one convenient instrument
Used around the world in meteorology, hydrology and climate research
Easily portable for field research

INTRODUCTION

The albedo of a surface is the extent to which it diffusely reflects short-wave radiation from the sun in the wavelength range from 300 to 3000 nanometers (nm). It is the ratio of the reflected radiation to the incoming radiation and varies from 0 (dark) to 1 (bright). As an indication, albedo is about 0.15 for grass, 0.5 for dry sand and 0.8 for fresh snow.

An Albedometer consists of two pyranometers. The upper sensor measures incoming global solar radiation and the lower sensor measures solar radiation reflected from the surface below. When the two signal outputs have been converted to irradiance in W/m², the albedo can be simply calculated.

Kipp & Zonen has been manufacturing pyranometers for over 75 years and our CMA albedometers share this experience and technology. They comply with the requirements of ISO 9060:1990 and are fully traceable to the World Radiometric Reference (WRR) in Davos, Switzerland, where Kipp & Zonen instruments form part of the World Standard Group.

APPLICATIONS

Kipp & Zonen albedometers have been developed for use in all environments, from the Antarctic to deserts. They are installed around the world for meteorology, hydrology, climate research, and agriculture. A particular use is for measuring the changing albedo of glaciers, snow and ice fields in climate change research.

Kipp & Zonen CMA albedometers are convenient all-in-one instruments designed for a long operating life with simple maintenance and the light weight is ideal for portable applications.

CHOICE OF ALBEDOMETER

The most appropriate model for an application depends on the desired accuracy and performance. CMA albedometers have broadband thermopile detectors and double glass domes, an integrated bubble level and a white sun shield to prevent the body heating up. The waterproof connector has gold-plated contacts and is fitted with 10 m of high quality signal cable as standard. The instruments do not require power and are supplied with calibration certificates traceable to the WRR.

CMA 6 is an ISO First Class albedometer that uses two CMP 6 pyranometer detector assemblies built into a single housing. An integrated glare screen prevents direct illumination of the lower domes at sunrise and sunset, and a screw-in drying cartridge keeps the interior free from humidity. A mounting rod is fitted to provide easy attachment to a mast.

Its good quality and cost-effectiveness make CMA 6 ideal for meteorology, hydrology and agriculture.

CMA 11 is a double CMP 11 pyranometer that complies with the highest level of ISO classification, Secondary Standard. It has all the features of the CMA 6 but a faster response detector design with temperature compensation.

CMA 11 is recommended for scientific applications, for which accuracy needs to be according to the highest standards.

OTHER CONFIGURATIONS

An entry level albedometer can be configured by using two CMP 3 pyranometers and the accessory mounting rod. Highest performance albedometers can be assembled using two CMP 21 or CMP 22 pyranometers and a CMF 1 mounting fixture. Ventilated setups are also possible.

Specifications	CMA6	CMA11
ISO 9060:1990 CLASSIFICATION	First Class	Secondary Standard
Response time (95 %)	< 18 s	< 5 s
Non-linearity (0 to 1000 W/m²)	< 1 %	< 0.2 %
Tilt error (at 1000 W/m²)	< 1 %	< 0.2 %
Temperature dependence of sensitivity	< 4 % (-10 °C to +40 °C)	< 1% (-10 °C to +40 °C)
Sensitivity	5 to 20 μV/W/m²	7 to 14 μV/W/m²
Impedance	20 to 200 Ω	10 to 100 Ω
Operating temperature	-40 °C to +80 °C	-40 °C to +80 °C
Spectral range (50 % points)	285 to 2800 nm	285 to 2800 nm
Maximum irradiance	2000 W/m²	4000 W/m²
Directional error (up to 80 ° with 1000 W/m² beam)	< 20 W/m²	< 10 W/m²
Weight (including rod & cable)	1.2 kg	1.2 kg

The CMA series have a standard cable lenght of 10 m
Optional cable lenghts 25 m and 50 m

Note: The performance specifications quoted are worst-case and/or maximum values

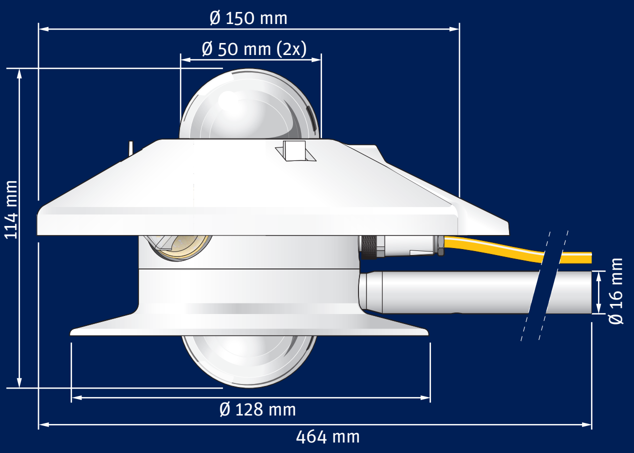

KIPP & ZONEN
SINCE 1830

Go to www.kippzonen.com for your local distributor

HEAD OFFICE

Kipp & Zonen B.V.
Delftechpark 36, 2628 XH Delft
P.O. Box 507, 2600 AM Delft
The Netherlands
T: +31 (0) 15 2755 210
F: +31 (0) 15 2620 351
info@kippzonen.com

Kipp & Zonen B.V. reserve the right to alter specifications of the equipment described in this documentation without prior notice

C

Measurement results

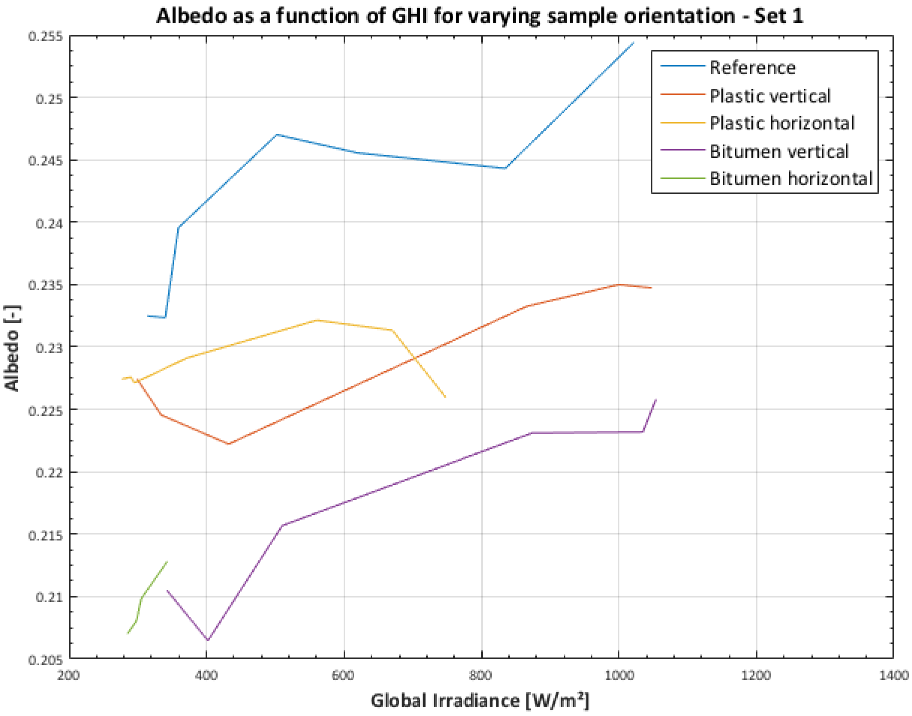

Figure C.1: The albedo as a function of GHI for different reflecting surface sample orientations for set 1.

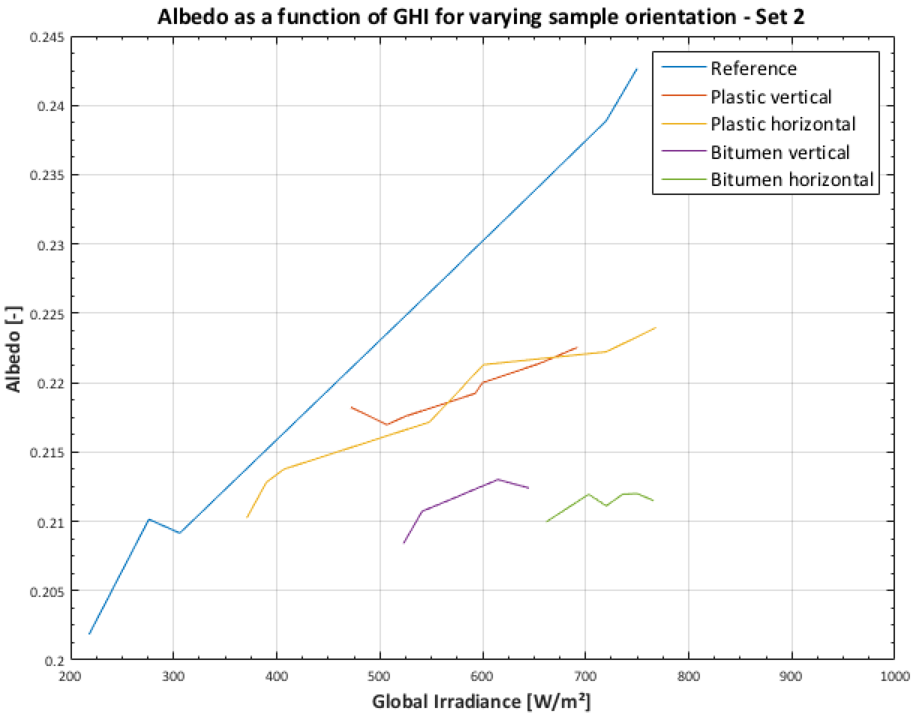

Figure C.2: The albedo as a function of GHI for different reflecting surface sample orientations for set 2.

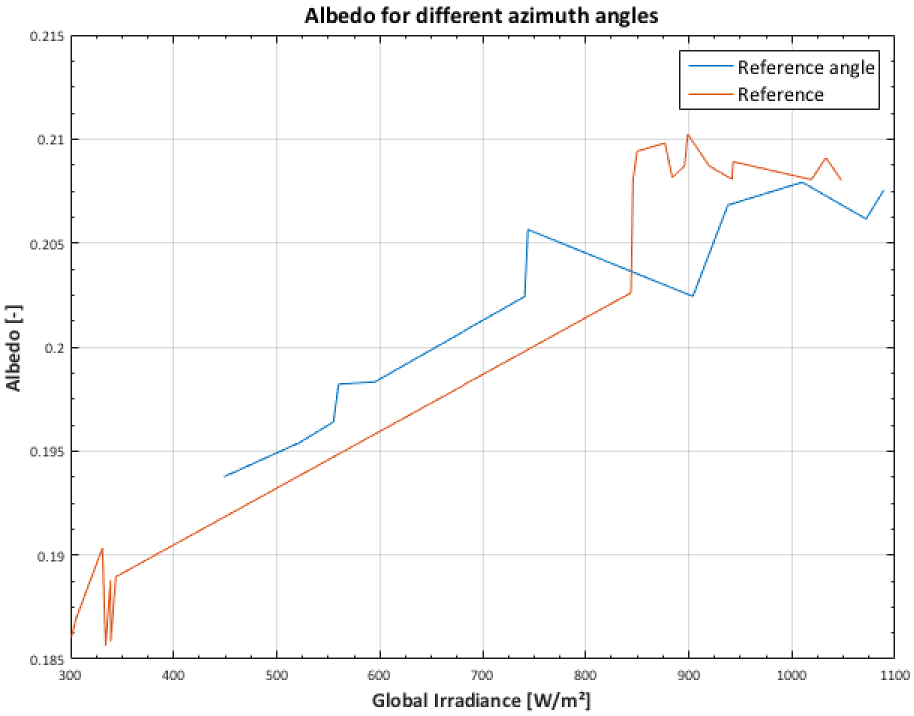

Figure C.3: The albedo as a function of GHI for different azimuth angles of albedometer.

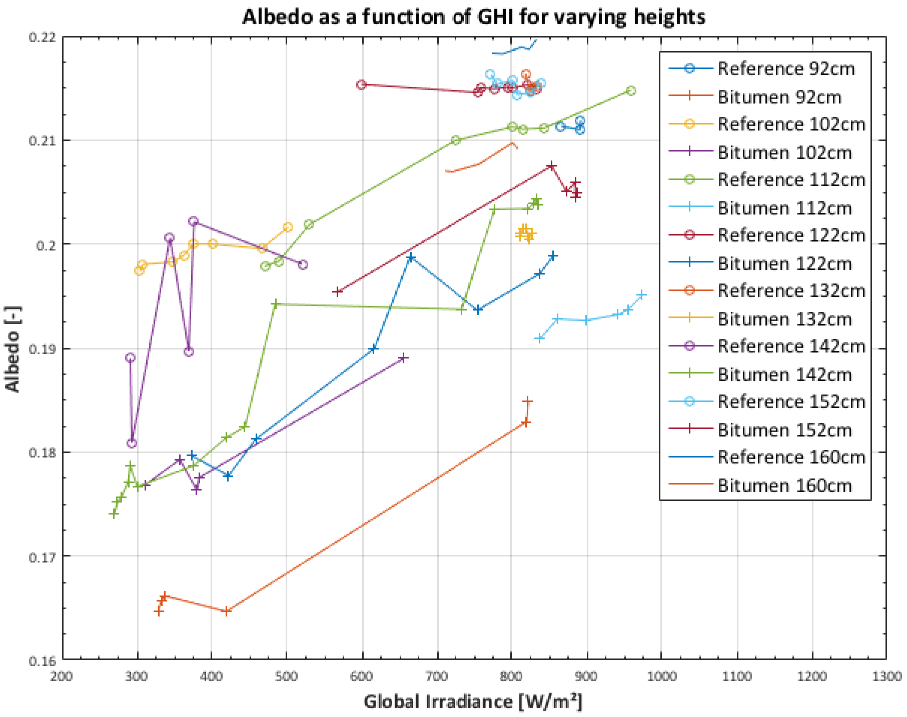

Figure C.4: The albedo as a function of GHI for different albedometer heights.

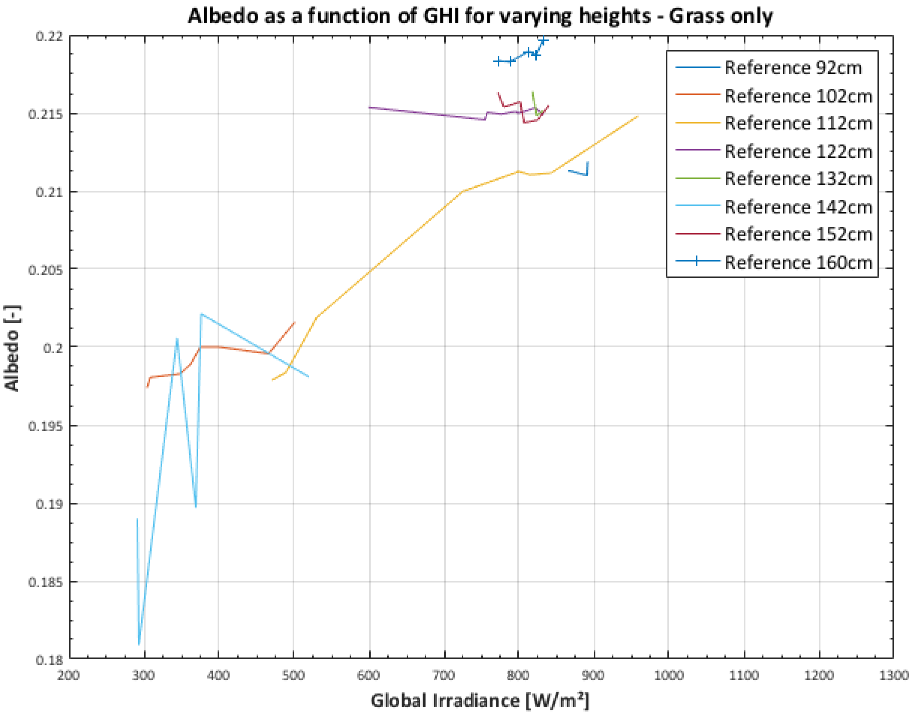

Figure C.5: The albedo as a function of GHI for different albedometer heights for grass only.

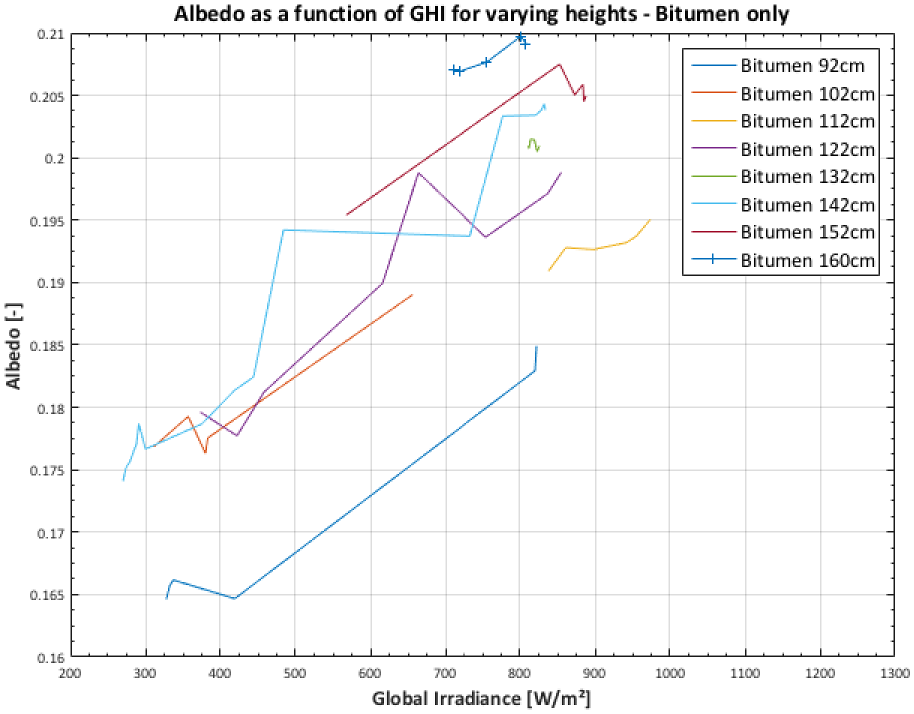

Figure C.6: The albedo as a function of GHI for different albedometer heights for bitumen only.

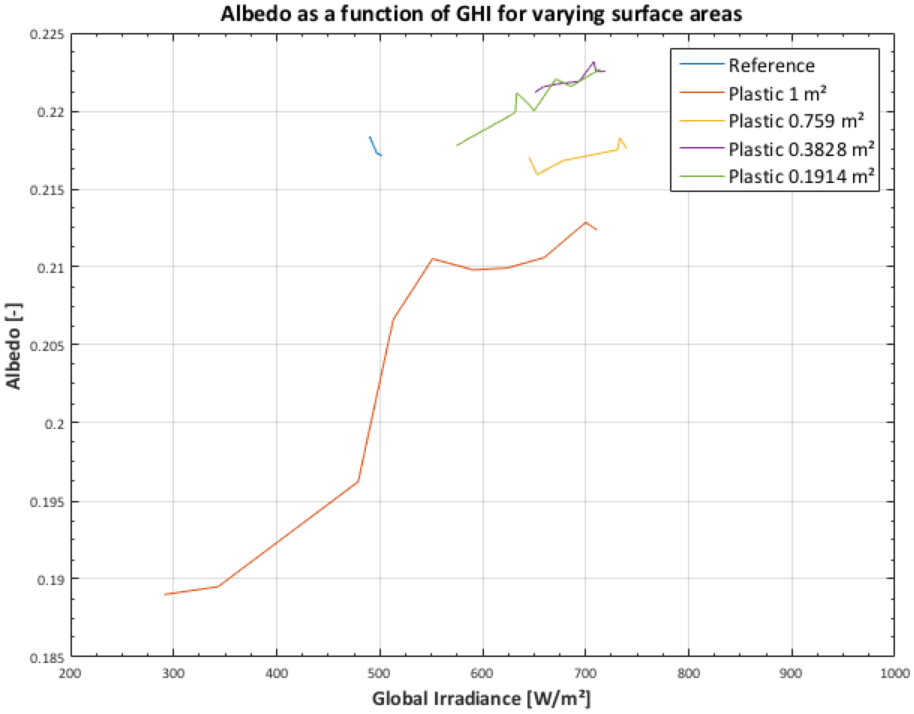

Figure C.7: The albedo as a function of GHI for different surface areas.

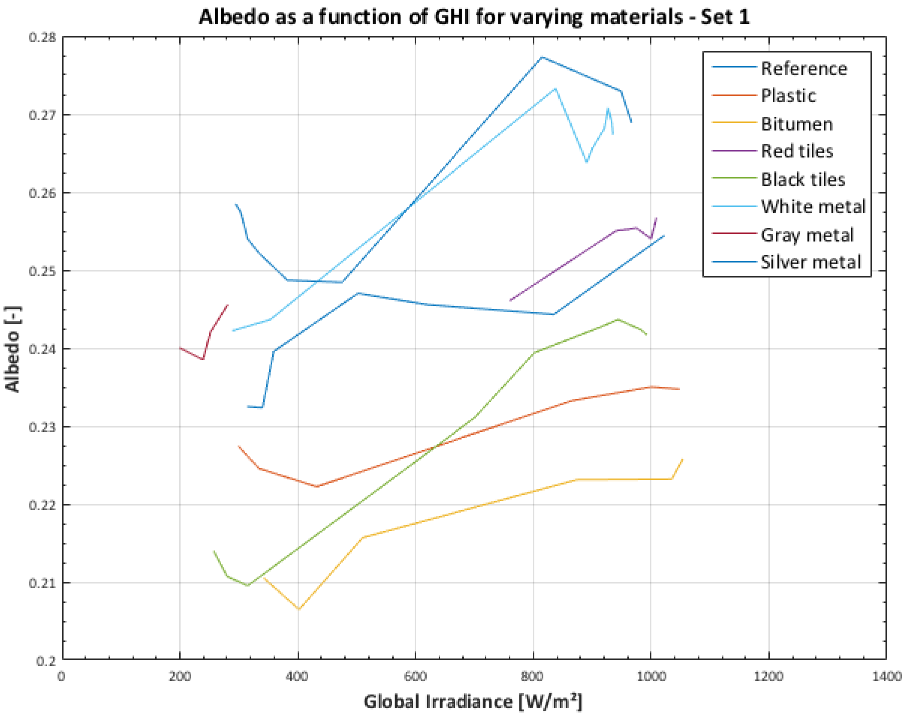

Figure C.8: The albedo as a function of GHI for different materials for set 1.

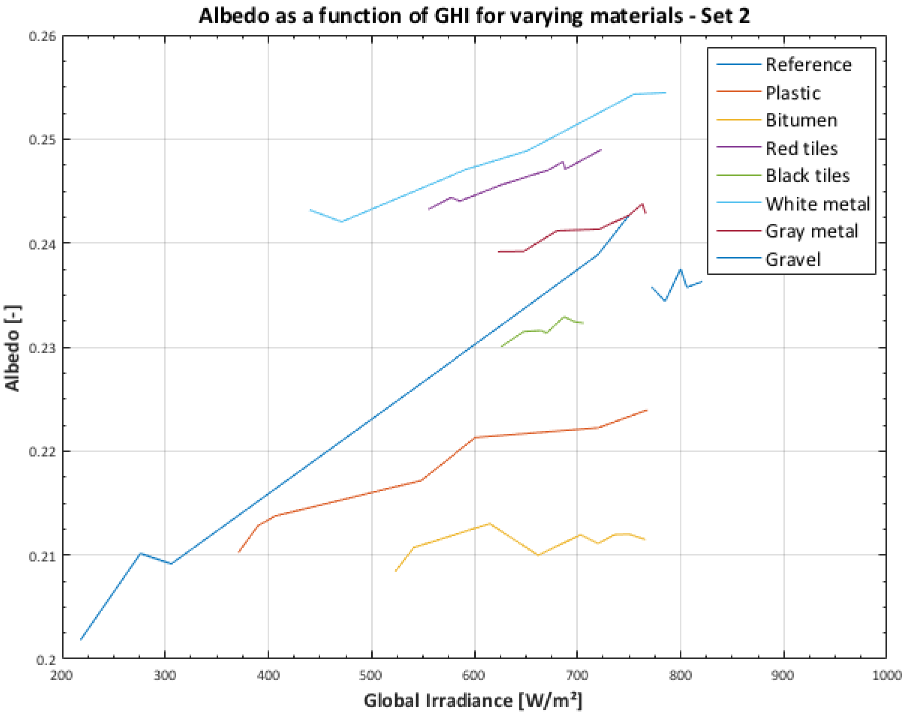

Figure C.9: The albedo as a function of GHI for different materials for set 2.

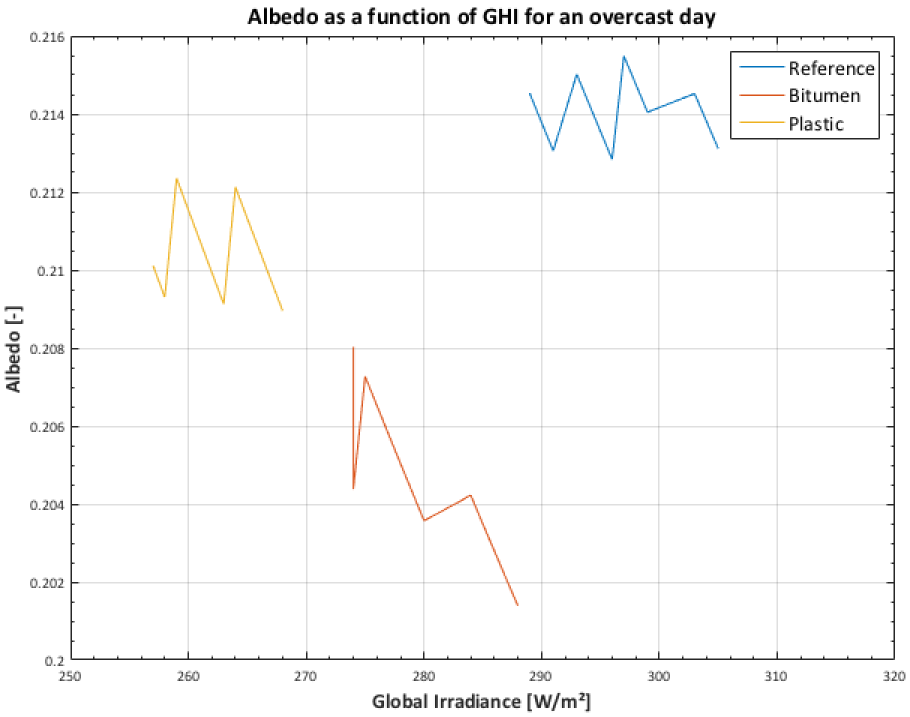

Figure C.10: The albedo as a function of GHI for diffuse irradiation only.

D

Paper draft

Albedo Recognition Model for Solar Engineering Applications

Hesan Ziar, Furkan Sonmez, Olindo Isabella, and Miro Zeman

Abstract.

With the rise of bifacial Photovoltaic (PV) technology it has become more important to accurately estimate the reflected irradiance. There is still very much discrepancy between different literature on the main ingredient of the reflected irradiance, which is the albedo. The albedo is subject to significant assumptions. The albedo is often considered as a constant, while a great amount of measurements have shown that it is changing constantly. This paper aims to introduce a mathematical model to describe the albedo as a function of the reflectivity of materials, the diffuse horizontal irradiance, the direct normal irradiance, the angle of incidence and the view factor of shaded and non-shaded areas, which can be used for solar engineering applications.

Index Terms— Albedo model, albedo recognition, solar engineering, photovoltaics, reflectance, spectral reflectivity, reflected irradiance.

I. INTRODUCTION

Forecasting the electric energy delivered by a Photovoltaic (PV) system is important for both plant owners and electric system operators [1]. Accurate PV system yield prediction minimizes technical risks and expenses. Uncertainty of PV system production can be minimized by accurate PV system modeling. PV system modeling is normally divided into three section: (1) optical, (2) thermal, and (3) electrical modeling. This paper mainly focuses on optical modeling of a PV system.

Irradiation received on the surface of a PV module consists of three main components : (1) direct normal irradiance or DNI, (2) diffuse horizontal irradiance or DHI, and (3) reflected irradiation. Influence rate of each component on the output of the PV system is strongly concerns with the PV system type and installation location. For the locations with frequent clear skies DNI is the dominant component while for the cloudy skies DHI play the most significant rule. For the building integrated and bifacial PV systems, reflected part of irradiation which is reflected by the ground and surrounding objects is of importance . Reflected part of the irradiance which is the main topic of this paper is also referred as “albedo component”. Albedo is defined as the ratio between reflected radiation and the global radiation incident on the measurement location .

Albedo is measured using albedometer which consists of two pyranometers. The upper sensor measures incoming global solar radiation and the lower sensor measures solar radiation reflected from the surface below. Simply, dividing the obtained values from lower sensor by upper sensor, the value of albedo is obtained .

DNI and DHI are measured at meteorological stations using pyrheliometer and pyranometer, respectively. However, for the albedo component, such data is not available because albedo might severely change from place to place. The reason is the geometry and material of the environment changes even in every few meters. Even for a specific location, the geometry of the environment changes by passing time so as albedo. Besides, even during a day, the measured albedo changes. This means that albedo also depends on the sky condition and position of the Sun. Therefore, it is fair to say, albedo almost depends on everything and that makes it difficult to model. Researchers developed several models to formulate the ground reflected albedo based on experimental data from different sites all over the world. The previously developed models for albedo will be addressed in Section II. Then, in section III the mathematical model of albedo developed in this paper will be introduced. Next, section IV describes the field test results for the proposed albedo model verification. Finally, some conclusions and remarks will be highlighted in section V.

II. ALBEDO MODELS

All the predeveloped albedo models are empirical models based on long term measured data. The first developed model for albedo is *constant albedo assumption* which suggests that constant albedo $\alpha = 0.2$ can be applied to the Global Horizontal Irradiance (GHI) to obtain the received irradiance on the reverse horizontal plane (downward facing surface of a horizontally mounted plane) [7]. Since the value of albedo is strongly case dependent, using constant albedo might lead to considerable error in many cases as authors in [c] reported 31% of albedo underestimation for a PV facade.

More accurate but site-dependent model of albedo is *mean measured albedo*. This model suggests a long-term albedo measurement for every location. The average measured values for each site can be assigned as the albedo of that site ($\alpha = \alpha_{site}$) [8]. The main disadvantage of this model is that it needs long-term monitoring of albedo for each site. Note that, albedo might severely change from place to place, then it makes it almost impossible to measure the albedo for a long time for every single location.

Another albedo model is *zonal albedo model* which shows the albedo dependency on latitude based on the measured data in North America [f]. The model suggests polynominal expressions for two ranges of latitude ($20° < \varphi \leq 30°$ and $30° < \varphi \leq 60$) in North America: $\alpha = \sum_{i=1}^{i=3} \alpha_i \varphi^i$ in which φ is in degree. The coefficients α_i, are determined monthly and can be found in [f]. This model cannot be applied for local albedo estimation. Also the provided empirical coefficient are only valid for North America and it might change for other places.

Next introduced albedo model in the literature is *Nkemdirim’s model* which models albedo as a function of the

Sun's elevation: $\alpha = \alpha_0 \exp(b\theta_z)$ where θ_z is the zenith angle in degree while α_0 and b are site-dependent coefficients based on the soil type and should be measured for each PV installation location [10]. The accuracy of this model strongly depends on the in-field measured coefficients.

Another study [e] proposed a different approach for albedo modeling by separating the albedo for direct and diffuse components. The *beam/diffuse albedo* model is a function of albedo for direct (or beam) radiation (α_b) and diffuse radiation (α_d) components on a horizontal plane, as: $\alpha = f(\alpha_b, \alpha_d)$.

Temps and Coulson model: is an empirical model

Complexity of albedo and its minor share in irradiation received on a surface of a module have been the most important reasons for less deep attention to this component so far. Normally in PV system modeling, albedo is either neglected or assumed to be constant value [b]. Albedo value of 0.2 is widely accepted and in used in PV modeling while authors in [c] showed that the value of albedo is strongly case dependent. Also it has been proven that this value can change seasonally [d][e]. One reason is the reflected component increases significantly when the ground is snow covered [a].

Authors in [11] proposed a constant value of 0.2 for the albedo during the year while results of the research and proved a strong seasonal dependence.

Assumption for mathematical modelling:
1. The foreground is horizontal, homogeneous and extends infinitely.
2. The reflecting surfaces contribute to the value of albedo are Lambertian surfaces which reflect light purely diffuse.

III. MATHEMATICAL MODELLING OF ALBEDO

This section, tries to understand how each influential factor affects the value of albedo measured at certain location and time. At the first step, let us assume that all the surrounding area of albedo measurement location (which reflects light) is homogenous and consists only one material. Some parts of the surrounding area is shaded and some parts are not. As a practical example, imagine that an albedometer has been set up horizontally in a wide grass-covered open plane and some parts of the ground is shaded by the albedometer itself[1]. Such a condition is depicted in Fig.1. In Fig. 1, surface S represents the surface that the albedo is measured on while surface A represents the area which contributes in reflecting light. Surface A is divided into two part. A_1 is not shaded and therefore receives both Direct Normal Irradiance (DNI) and Diffuse Horizontal Irradiance (DHI) while A_2 only receives diffuse component ($A_1 + A_2 = A$). Let us assign the reflectivity value of R to the surface A. For an albedometer, albedo is calculated by dividing the incoming global radiant fluxes (W) reach on the up-facing and down-facing parts of surface S, as:

$$\alpha = \frac{\Phi^{S}_{\mathrm{down}}}{\Phi^{S}_{\mathrm{up}}} \tag{1}$$

where Φ^{S}_{down} and Φ^{S}_{up} are the incoming global radiant fluxes (W) on the up-facing and down-facing parts of surface S. For the up-facing side of surface S, the radiant flux is:

$$\Phi^{S}_{\mathrm{up}} = S\left[\mathrm{DNI}^{S}_{\mathrm{up}} \cos(\theta) + \mathrm{DHI}^{S}_{\mathrm{up}}\right] \tag{2}$$

where S is the area of surface S (m^2) and θ is the angle of incident between the flux of irradiation and the normal of surface S $(0 \leq \theta \leq 90)$. DNI^{S}_{up} and DHI^{S}_{up} are the direct and diffuse components of the sunlight reach on the up-side of surface S, respectively (W/m^2). Having the reflected amount of sunlight from surface A, it is possible to calculate the received irradiation on the bottom part of the surface S using view factor concept. For two arbitrary surfaces of i and j in space, F_{ij} is defined as the fraction of the radiant flux leaving surface i that is intercepted by surface j . Therefore, the received radiant to the down-facing part of surface S is equal to:

$$\begin{aligned}\Phi^{S}_{\mathrm{down}} = {} & \mathrm{R}\ \mathrm{A}_1\left[\mathrm{DNI}^{\mathrm{A}_1}_{\mathrm{down}} \cos(\theta) + \mathrm{DHI}^{\mathrm{A}_1}_{\mathrm{down}}\right]\mathrm{F}_{\mathrm{A}_1 \to \mathrm{S}} \\ & + \mathrm{R}\ \mathrm{A}_2\left[\mathrm{DHI}^{\mathrm{A}_2}_{\mathrm{down}}\right]\mathrm{F}_{\mathrm{A}_2 \to \mathrm{S}}\end{aligned} \tag{3}$$

where $F_{S \to A1}$ and $F_{S \to A2}$ are the view factors from surfaces A_1 and A_2 to the down-part of the surface S. θ is the angle of incident between the flux of irradiation and the normal of surface A (since surfaces A and S are both horizontal, the angle of incident is equal for both them). DNI^{A1}_{down} and DHI^{A1}_{down} are the direct and diffuse components of the sunlight reach on surfaces A_1, respectively, while DHI^{A2}_{down} is the diffuse component on surface A_2 (W/m^2).
In Fig. 1, the following relations are hold true between DHI and DNI values for different surfaces:

$$\mathrm{DHI}^{S}_{\mathrm{up}} = \mathrm{SVF}^{S}\ \mathrm{DHI}_{\mathrm{m}} \tag{4}$$

$$\mathrm{DNI}^{S}_{\mathrm{up}} = \mathrm{DNI}_{\mathrm{m}} \tag{5}$$

$$\mathrm{DHI}^{\mathrm{A}_1}_{\mathrm{down}} = \mathrm{SVF}^{\mathrm{A}_1}\ \mathrm{DHI}_{\mathrm{m}} \tag{6}$$

$$\mathrm{DNI}^{\mathrm{A}_1}_{\mathrm{down}} = \mathrm{DNI}_{\mathrm{m}} \tag{7}$$

$$\mathrm{DHI}^{\mathrm{A}_2}_{\mathrm{down}} = \mathrm{SVF}^{\mathrm{A}_2}\ \mathrm{DHI}_{\mathrm{m}} \tag{8}$$

$$\mathrm{DNI}^{\mathrm{A}_2}_{\mathrm{down}} = 0 \tag{9}$$

where DNI_m and DHI_m are the direct and diffuse components of the sunlight measured at the meteorological station (W/m^2). SVF^{A1}, SVF^{A2} and SVF^{S} are the sky view factors for the surfaces A_1, A_2, and S, respectively. Using (4) to (9), one can substitute (2) and (3) in (1) and obtain:

---

[1] A bifacial PV module that causes shade on the ground beneath the module is also another example.

$$\alpha = R\left(\frac{H+SVF^{A_1}}{H+SVF^{S}}\left(\frac{A_1}{S}F_{A_1\to S}\right)+\frac{SVF^{A_2}}{H+SVF^{S}}\left(\frac{A_2}{S}F_{A_2\to S}\right)\right) \tag{10}$$

where H is defines as:

$$H = \frac{DNI_m}{DHI_m}\cos(\theta) \tag{11}$$

By Applying the reciprocity rule for view factors ($A\,F_{A\to B} = B\,F_{B\to A}$), it is possible to rewrite (10) as:

$$\alpha = R\left(\frac{H+SVF^{A_1}}{H+SVF^{S}}F_{S\to A_1}+\frac{SVF^{A_2}}{H+SVF^{S}}F_{S\to A2}\right) \tag{12}$$

When the reflecting surface A is tilted, (25) is transformed to:

$$\alpha = R\left(\frac{H\frac{\cos(\theta_S)}{\cos(\theta)}+SVF^{A_1}}{H+SVF^{S}}F_{S\to A_1}+\frac{SVF^{A_2}}{H+SVF^{S}}F_{S\to A_2}\right) \tag{13}$$

where θ_1 is the angle of incident for surface A. Equation (13) shows the value of the albedo when the albedometer is horizontally mounted in homogenous surrounding. For a wide open area with no objects around, $SVF^{A1} = SVF^{A2} = SVF^{S} = 1$ and $\theta_S = \theta$, then:

$$\alpha = R\left(F_{S\to A_1}+\frac{1}{H+1}F_{S\to A_2}\right) \tag{14}$$

where,

$$R = \frac{\int R(\lambda)\,G(\lambda)\,d\lambda}{\int G(\lambda)\,d\lambda} \tag{15}$$

In (15), $G(\lambda)$ is the broadband spectrum incident on the surface A. $R(\lambda)$ is the spectral reflectivity of surface A which varies with respect to spectrum. It should be noted that the spectrum received from the Sun, $G(\lambda)$, also changes depending on the position of the sun in the sky because the air mass (AM) ratio which sunlight sees in not always the same. This also affects the value of R because different materials reflect some wavelengths of the spectrum better than other wavelengths.

Equation (14), as a mathematical model for albedo, indicates that the albedo depends on: (1) *geometry* which shows itself as view factor terms, (2) *reflectivity* of the surrounding material, and (3) the factor H which models the effect of sun position and sky condition.

Equation (14) also shows that both sunny and shaded areas contribute to the value of albedo (depends on how much the albedometer sees shaded and sunny areas). Size of the shade also change by time which leads to variation of view factor values. H is also a function of time because DNI, DHI and position of the sun changes during a day or throughout a year.

In (14), coefficient $1/(H+1)$ models the brightness of the shaded area and $0 \leq 1/(H+1) \leq 1$. It is worth mentioning that $F_{S\to A1} + F_{S\to A2} = 1$ (summation rule of view factors) which results in:

$$\alpha \leq R \tag{16}$$

This means that albedo is always lower than or equal to reflectivity. However, sometime in the literatures albedo is referred as reflection coefficient of the ground which might cause ambiguity with surface reflectivity [pvmd ebook]. It should be noted that, albedo is a measure which is used in energy calculations while reflectance is a property of a material. It can be comprehended that albedo is maximum when $F_{S\to A2} / (H+1) = 0$.

However, R, H and view factors are not constant and depend on time. Albedo is a measure of energy while surface reflectance is a property of a material.

The fraction of sunlight that is reflected by a given surface is known as albedo. Albedo has spectral and directional dependencies and, consequently, it is not a straightforward intrinsic property of materials. It is a property of materials that depends on the directional and spectral conditions of the sunlight at any given time. The albedo from common ground surfaces introduces a spectral bias that can impact the optimal selection of PV materials.

Before extending (14) for the area with n number of different materials, Equation (14) shows that even in non-urban areas the value of albedo might change during measurements. But which value of the albedo should be used in PV system modelling?

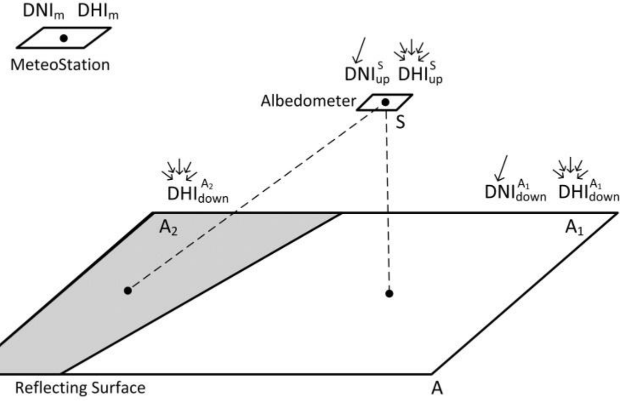

IV. CONCLUSIONS

The proposed model will allow for a more accurate automated PV system design, because the albedo can be determined more accurately. In order to use the model in PV system design, the materials of the surroundings must be known. By using the spectral reflectivity of the material, the reflectance can be determined. Then, using the irradiances obtained from meteorological data, the instantaneous albedo of a surface can be determined. This model is important, because the albedo is often considered as a constant or a lot of time is lost through field work in which the albedo is measured for long periods of time. Using this model, there will be no more need for measurements in the field.

References.

P. Ineichen, O. Guisan, and R. Perez, Ground-reflected radiation and albedo, Solar Energy,44,207 (1990).

A. Mills, Basic Heat and Mass Transfer(Prentice Hall, 1999).

M. Brennan, A. Abramase, R. Andrews, and J. Pearce, Effects of spectral albedo on solar photo-voltaic devices,Solar Energy Materials and Solar Cells124, 111 (2014)

C. A. Gueymard, The sun’s total and spectral irradiance for solar energy applications and solarradiation models,Solar Energy76, 423 (2004)